



Surface chemistry of oxygenates on rutile(110)

Von der

Fakultät für Mathematik und Naturwissenschaften der
Carl von Ossietzky Universität Oldenburg

zur Erlangung des Grades und Titels eines

Doktors der Naturwissenschaften (Dr. rer. nat.)

angenommene

Dissertation

von Herrn

Peter Clawin

geboren am 28. März 1984 in Münster

Gutachterin:

Prof. Dr. Katharina Al-Shamery

Zweitgutachter:

Prof. Dr. Thorsten Klüner

Tag der Disputation: 19.12.2014

Contents

Abstract	v
Kurzzusammenfassung	vii
Danksagungen	ix
Abbreviations	xi
List of figures	xv
List of tables	xvii
1 Introduction	1
2 Methods	5
2.1 Ultra high vacuum (UHV)	5
2.2 Temperature programmed desorption (TPD)	6
2.3 Infrared reflection absorption spectroscopy (IRRAS)	11
2.4 Low energy electron diffraction (LEED)	17
2.5 Density functional theory (DFT)	19
3 Experimental details	23
3.1 UHV system	23
3.2 Samplamount	23
3.3 Sample preparation	24
3.4 LEED	25
3.5 Doser	25
3.6 TPR spectra	30
3.7 IR spectra	32
4 Literature review titania	37
4.1 The rutile(110) surface	37
4.2 Defects	38
4.3 Surface chemistry of oxygen	40

5	Reductive coupling of benzaldehyde	45
5.1	Surface chemistry of carbonyl components	45
5.2	Previous work	46
5.3	Adsorption and reaction of benzaldehyde on reduced rutile(110)	49
5.4	Influence of bulk defect density	55
5.5	Oxygen	60
5.6	Conclusion	63
6	Oxidation reactions on rutile(110)	65
6.1	Literature overview reaction of oxygen with coadsorbats	66
6.1.1	Carbon monoxide	66
6.1.2	Water	67
6.1.3	Carbonyl compounds	68
6.2	Results	73
6.2.1	Oxidation of benzaldehyde	73
6.2.2	Oxidation of acetone	78
6.2.3	DFT results	82
6.3	Discussion	91
6.3.1	Oxidation to the carboxylates	91
6.3.2	Acetone-oxygen intermediate	94
6.4	Conclusion	97
7	Deprotonation, dehydrogenation and disproportionation of alcohols	101
7.1	Surface chemistry of alcohols	102
7.2	Results	106
7.2.1	Benzylalcohol results	107
7.2.2	DFT Results	112
7.3	Discussion	119
7.3.1	Benzylalcohol	120
7.3.2	Methanol	123
7.4	Conclusion	124
8	Summary and Outlook	127
	Appendix	131
1	Cluster Model	131
2	DFT functionals and basis sets	133
3	Preliminary NRA results	136
	Curriculum vitae	137

Publications	139
Selbstständigkeitserklärung	141
Bibliography	141

Abstract

Reducible transition metal oxides like titania are promising candidates for applications in heterogeneous catalysis or photo catalysis. These applications involve redox reactions which occur at the surface of the material. Therefore, within this work the surface chemistry of oxygenates on titania is studied, which are key intermediates in these redox reactions. In contrast to previous work, infrared reflection absorption spectroscopy (IRRAS) provides a significantly better means to identify surface bound species. The focus of this work lies on the interaction of adsorbates with bulk and surface defects and the various kinds of oxygen species that form on the surface:

The role of defects is demonstrated in the reductive coupling of benzaldehyde to stilbene. Using IRRAS, this work provides strong experimental evidence for the formation of a stilbene diolate intermediate on the surface. Furthermore, the concentration of this diolate and the stilbene yield observed in temperature programmed reaction spectra (TPRS) is found to scale with the bulk defect density, which strongly suggest that this reaction is driven by bulk defects.

Besides the reductive coupling, the reaction of benzaldehyde with coadsorbed oxygen is studied and compared to the analogue reactions with acetone. For benzaldehyde the oxidation to benzoate by coadsorbed molecular oxygen is observed, whereas for acetone an additional surface bound intermediate is indicated by an IR signal at 1196 cm^{-1} . Two candidates for this intermediate, an acetal, which has been proposed in the literature, and an aldol reaction intermediate are discussed. Additionally, the dissociative adsorption of benzylalcohol and methanol with coadsorbed oxygen is examined. The results presented herein suggest a dehydrogenation and disproportionation of benzylalcohol.

Kurzzusammenfassung

Reduzierbare Übergangsmetalloxide wie z.B. Titandioxid sind vielversprechende Materialien für Anwendungen in der heterogenen Katalyse oder der Photokatalyse. Für diese Anwendungen spielen Redoxreaktionen an der Oberfläche des Materials eine zentrale Bedeutung. Daher wird in dieser Arbeit die Oberflächenchemie von sauerstoffhaltigen Verbindungen auf Titandioxid untersucht, welche wichtige Intermediate in diesen Redoxreaktionen sind. Im Gegensatz zu früheren Arbeiten zu diesem Thema profitiert diese Arbeit von der Infrarot-Reflexions-Absorptions-Spektroskopie (IRRAS), welche wesentlich besser dazu geeignet ist auf der Oberfläche gebundene Spezies zu identifizieren. Schwerpunkt dieser Arbeit ist die Wechselwirkung von Adsorbaten zum einen mit Volumen und Oberflächendefekten und zum anderen die verschiedenen Sauerstoffspezies die sich auf der Oberfläche bilden:

Die Rolle von Defekten wird anhand der reduktiven Kopplung von Benzaldehyd zu Stilben untersucht. IRRA Spektren in dieser Arbeit geben Hinweise auf die Bildung eines Stilbendiolates auf der Oberfläche. Zudem wird gezeigt, dass die Konzentration dieses Diolates und die Stilbenausbeute in Thermo-Desorptions-Spektren (TDS) mit der Defektdichte des Kristalles skaliert, was darauf hinweist, dass diese Reaktion an Defektstellen abläuft.

Neben der reduktiven Kopplung wird die Reaktion von Benzaldehyd mit koadsorbiertem Sauerstoff untersucht und mit den analogen Reaktionen von Aceton verglichen. Die Ergebnisse zeigen, dass Benzaldehyd durch koadsorbierten Sauerstoff zu Benzoat oxidiert wird. Für Aceton wird ein zusätzliches Intermediat anhand eines Signals im IR Spektrum bei 1196 cm^{-1} beobachtet. Zwei unterschiedliche Kandidaten für dieses Intermediat werden diskutiert: zum einen ein Acetal, welches in der Literatur diskutiert wurde und zum anderen das Produkt einer Aldolreaktion. Zudem wird die Reaktion von Benzylalkohol und Methanol mit koadsorbiertem Sauerstoff untersucht. Die hier vorgestellten Ergebnisse deuten auf eine Dehydrogenierung und eine Disproportionierung von Benzylalkohol hin.

Danksagungen

An dieser Stelle möchte ich allen Person danken die mich beim Verfassen dieser Arbeit unterstützt haben:

Frau Prof. Katharina Al-Shamery und Frau Prof. Cynthia Friend danke ich für das interessante Thema meiner Arbeit und die Betreuung während meiner Doktorarbeit.

Herrn Prof. Thorsten Klüner danke ich für die Bereiterklärung zur Übernahme des Zweitgutachten und hilfreiche Diskussionen zu den DFT Rechnungen.

Rainer Koch danke ich für die Einführung in Gaussian, die Unterstützung beim Durchführen der DFT Rechnung und deren Diskussion.

Philipp Rahe, Jan Haubrich, Dirk Hoogestraat und Martin Baron danke ich für die Unterstützung bei experimentellen Fragen und die Diskussion meiner Ergebnisse.

Franziska Träger danke ich für die Zusammenarbeit bei den NRA Experimenten, Christopher Krause für ESR Messungen zur Bestimmung der Defektdichten in den verwendeten Kristallen.

Milena Osmić danke ich für die Weiterführung meines Themas.

Martina Nullmeier, Sebastian Eckert, Philipp Rahe und Gordon Schröder danke ich für das Korrekturlesen meiner Arbeit.

Den Mitarbeitern der Instandsetzung, insbesondere Herrn Holger Tuband, der Mechanischen Werkstätten und der Elektronikwerkstatt der Universität Oldenburg danke ich für Unterstützung bei technischen Problemen.

Ich danke dem Fonds der Chemischen Industrie (FCI) und dem Deutschen Akademischen Austauschdienst (DAAD) für die finanzielle Unterstützung.

Danksagungen

Und ganz besonders danke ich meinen Eltern, Großeltern, Tanten, Onkeln für die Unterstützung während meiner gesamten Ausbildungszeit.

Abbreviations

AFM	Atomic Force Microscopy
BOV	Bridging Oxygen Vacancy
DFT	Density Functional Theory
EELS	Electron Energy Loss Spectroscopy
EPR	Electron Paramagnetic Resonance
GGA	Generalized Gradient Approximation
HF	Hartree Fock
HFA	Hexafluoroacetone
HREELS	High Resolution Electron Energy Loss Spectroscopy
IRRAS	Infra Red Reflection Absorption Spectroscopy
KS-orbital	Kohn Sham orbital
LDA	Local Density Approximation
ML	Mono Layer
mL	milli Langmuir (10^{-9} Torr s)
NC-AFM	non contact atomic force microscopy
NIST	National Institute of Standards and Technology
O _{ad}	oxygen adatom
O _{br}	bridging oxygen
OH _{br}	hydroxyl groups adsorbed in place of O _{br}
OH _t	terminal hydroxyl groups adsorbed at Ti _{5c}
PES	Photoelectron Spectroscopy
PSD	Photo Stimulated Desorption
SDBS	Spectral Database for Organic Compounds
SSIMS	Static Secondary Ion Mass Spectroscopy
STM	Scanning Tunneling Microscopy
TDS	Thermal Desorption Spectroscopy
TFA	1,1,1-Trifluoroacetone
Ti _{5c}	five coordinated titanium atom
TPD	Temperature Programmed Desorption
TPRS	Temperature Programmed Reaction Spectroscopy
UHV	Ultra High Vacuum
XPS	X-ray Photoelectron Spectroscopy

Symbols

α	polarizability
γ	damping constant
λ	wavelength
ν	frequency
$\psi_i(r)$	one-electron orbital
$r_{(sp)}$	reflective coefficients
$\rho(r)$	electron density
θ	angle of incidence
$\tilde{\nu}$	wavenumber
c	speed of light
\vec{D}	displacement
$d_{(x y z)}$	diagonal elements of the d matrix
d	thickness of adsorbat layer
$E_{XC}[\rho(r)]$	exchange correlation functional
e	elementary charge
$n_{(v s ad)}$	refractive index of v: vacuum, s: substrat, ad: adsorbat layer
N	density of dipoles
q	effective electric charge

Vibration modes

ν	valence stretch mode
ν_{sym}	symmetric valence stretch mode
ν_{asym}	asymmetric valence stretch mode
δ	in plane deformation
ρ	out of plane deformation

List of Figures

2.1	TPD desorption maximum shifts to higher temperatures with increasing desorption energy.	7
2.2	Mass discrimination of quadrupole mass spectrometers	10
2.3	The metal surface selection rule	12
2.4	Illustration of the three layer model	13
2.5	Calculated absorption based on 3-layer model	15
2.6	Laue Diffraction	18
3.1	Photographic image of the used vacuum system.	24
3.2	LEED diffraction pattern of the rutile(110) surface	26
3.3	Rutil(110) LEED patterns	26
3.4	Explosion view of the used vapor doser	27
3.5	Schematics of the gas system used for dosing vapors	28
3.6	A glass flask used for dosing liquids.	29
3.7	Shielding of the mass spectrometer	30
3.8	Single channel IR spectra	33
3.9	Absorbance spectrum before and after baseline subtraction	34
3.10	Artifact signal observed due to drift	35
3.11	Artifact signal from adsorbate on sample holder	36
4.1	Rutile titania(110) surface	38
4.2	Schematic overview reactions of oxygen on rutile titania(110)	41
4.3	STM images of oxygen dissociation	42
5.1	Stilbene diolate intermediate	47
5.2	TPR spectra of benzaldehyde	48
5.3	STM image indicating pairing of benzaldehyde	50
5.4	Coverage dependent IR spectra of benzaldehyde	51
5.5	p-polarized IR spectra recorder after heating to increasing temperatures	53
5.6	Photos of the used rutile(110) crystal after reduction	55
5.7	Influence of bulk defect density on adsorption of benzaldehyde at 110 K	57

List of Figures

5.8	Influence of bulk defect density on intermediate formation	58
5.9	TPR spectra of stilbene yield based on bulk defect density	59
5.10	TPRS stilbene yield and integrated IR intensity of the alkoxy signal	59
5.11	TPR spectra of benzaldehyde with codosed oxygen	61
5.12	IR spectra of stilbene diolate with postdosed oxygen	62
6.1	The surface analogue of the aldol condensation	69
6.2	The surface analogue of the Cannizzaro reaction	70
6.3	Radical oxidation	71
6.4	IRRA spectra of benzaldehyde oxidation	74
6.5	TPRS fragments indicating benzoic acid	75
6.6	Influence of benzaldehyde coverage on the oxidation yield	76
6.7	Coverage dependent benzoate yield	77
6.8	Preparation of an oxidized surface	77
6.9	TPR spectra of acetone adsorbed on a reduced surface and with coadsorbed oxygen	80
6.10	p-polarized IRRA spectra of the reaction of acetone with coad- sorbed oxygen.	81
6.11	DFT results for acetate and benzoate adsorbed on the cluster. .	84
6.12	DFT results for acetone acetals	86
6.13	DFT results for benzaldehyde acetals	87
6.14	DFT results for isopropenolate	89
6.15	4-hydroxy-4-methylpentane-2-one	90
6.16	Summary acetone oxidation	99
7.1	Overview of reactions which were proposed for methanol on ru- tile(110)	103
7.2	β -hydrogen elimination reactions of aliphatic alcohols	105
7.3	TPR spectrum of benzylalcohol	108
7.4	Toluene signals observed in benzylalcohol TPRS	109
7.5	IR spectrum of benzylalcohol	110
7.6	DFT results for methanol and methoxy	112
7.7	DFT results for benzylalcohol and benzyloxy	113
7.8	DFT results for methanol and methoxy with coadsorbed termi- nal hydroxyl groups.	114
7.9	DFT results for benzylalcohol and benzyloxy with coadsorbed terminal hydroxyl groups.	115
7.10	Alternative reaction products and intermediates considered for methanol	118
7.11	Proposed mechanism for toluene formation	122

1	The used $\text{H}_8\text{Ti}_2\text{O}_8$ cluster model	132
2	Acetone adsorbed on the $\text{H}_8\text{Ti}_2\text{O}_8$ cluster	133
3	Preliminary NRA results	136

List of Tables

5.1	Overview of observed signals and references	55
6.1	Carboxylate vibrations for acetate and benzoate	85
6.2	Reference vibrations for acetals (see figures 6.12 and 6.13). p: mostly parallel to surface, +/-: observed as positive or negative absorbance signal, n.o.: not observed	88
6.3	Reference frequencies for aldol intermediates	91
6.4	Overview bond dissociation energies in kJmol^{-1} for the reaction $\text{O}\cdot + \text{R}-(\text{C}=\text{O})-\text{X} \longrightarrow \text{O}-\text{X} + \text{R}-(\text{C}=\text{O})$. ^[221]	93
7.1	Relative intensities of key fragments from the NIST fragmenta- tion pattern of benzylalcohol	107
7.2	Overview of the vibrations for alcohols	117
7.3	Overview of the bond lengths for alcohols	119
1	Cluster Coordinates used for Gaussian09	131
2	Vibration results for B3LYP and PBE0 (and M06) using 6- 31+G(d,p) and 6-311+G(d,p) basis sets.	135

1 Introduction

In many applications, reactions at surfaces play a central role in the function of materials, yet these reactions are often poorly understood.^[1] Such reactions are involved in processes like thin film deposition like atomic layer deposition,^[2] surface coatings e.g. anti fog coatings,^[3] the decomposition of natural organic materials in sediments to yield crude oil^[4,5] and heterogeneous catalysis.^[6,7] The latter is a key technology in chemical engineering: About 90% of all reaction processes involve a catalyst, most of which are heterogeneous catalysts.^[7] The catalyst lowers the reaction barrier of a chemical reaction by providing an alternative reaction pathway which usually involves elementary reactions steps on the surface of the catalyst. The importance of understanding such elementary reactions at surfaces has been pointed out by the Nobel prize committee by awarding the Nobel prize in chemistry to Gerhard Ertl "for his studies of chemical processes on solid surfaces" in 2007.^[1] The most prominent example for heterogeneous catalysis is probably the Haber-Bosch process, which is used to produce ammonia from nitrogen and hydrogen.^[1,8] This reaction occurs on the surface of an iron oxide catalyst, which activates the otherwise chemically inert nitrogen.^[8] The research goal in heterogeneous catalysis is the fundamental understanding of the interaction of molecules with the surface upon adsorption, in order to design catalysts for new chemical processes with lower energy demand and fewer waste side products.^[6,7] One approach to accomplish this is by using photo catalysis on semiconductor materials:^[9-11] on a photo catalyst, the chemical reaction is driven by a photo generated exciton, which is an electron hole pair. Therefore, photo catalysis enables reaction pathways, which are not accessible for thermally driven reactions in conventional catalysis.

Unfortunately, reactions in technical environments are often too complex to be studied systematically. For example, a commercial catalyst often consists of metal particles adsorbed on a support material.^[12] The total reaction at the catalyst involves various steps including the diffusion of the reactants to the catalyst, adsorption and possibly dissociation on the surface of the support or the metal particle, diffusion on the surface to an active site, reaction with a coadsorbate, desorption and diffusion of the product away from the surface.^[8]

1 Introduction

Furthermore, the structure of catalysts under reaction condition is usually not well defined. For example in some cases the encapsulation of the metal particles by a thin layer of the support material under reaction conditions was reported.^[13] This effect is known as the strong metal support interaction (SMSI).^[13] Additionally, under applied reaction conditions coadsorbates such as water and oxygen are omnipresent, which can greatly affect the reaction of interest. Due to this complexity, Irving Langmuir proposed in 1922 that simple model systems need to be studied to understand the underlying principles.^[14] This approach to manage the complexity is still used today in heterogeneous catalysis research.^[7] Within this work, reactions on a single crystal are studied in ultra high vacuum (UHV) as a model system: The surface structure of such single crystals is well defined, and the UHV environment offers control over the crystals exposure to adsorbates and the presence of coadsorbates.

A promising candidate for applications in (photo) catalysis is titania. It is particularly interesting as a redox catalyst, as it is a reducible oxide.^[15,16] Upon heating in vacuum or hydrogen, titania is partly reduced which introduces defects in the crystal. These defects were proposed to act as a buffer for charge which is transferred in a redox reaction. For example, Haruta et al. have shown that gold nano particles catalyze the CO oxidation at low temperatures when they are supported on titania even though both metal particles and support are inert for this reaction by themselves.^[12,17,18] Furthermore, titania is a promising candidate as a photo catalyst: Fujishima and Honda have demonstrated that titania produces hydrogen by photo electro chemical water splitting.^[9,19] The gained hydrogen could be used as a renewable fuel which could be converted into electricity in fuel cells. Besides generation of solar fuels, titania is used as a photo catalyst to photo oxidize organic pollutants in air or waste water^[9,20] and as a semiconductor in the Grätzel cell, which is a dye-sensitized solar cell.^[21]

The common aspect of the applications mentioned above, is that they all involve redox reactions of oxygenates on the titania surface. Therefore, the goal of this work is to gain a fundamental understanding of oxidation and reduction processes on titania: To this end carbonyl compounds, such as benzaldehyde and acetone, and alcohols, such as benzylalcohol, have been chosen as probe molecules to study their interaction with defects and coadsorbed oxygen.

For a better understanding of the surface reactions, infra red reflection absorption spectroscopy (IRRAS) is introduced. IRRAS allows an identification of reaction intermediates on the surface, a piece of information which is not accessible through commonly used thermal desorption techniques or scanning probe microscopy. IRRAS is frequently used on metal surfaces, but it has been intro-

duced on dielectric surfaces such as titania only recently due to experimental challenges which are discussed in section 2.3. This work demonstrates the value of IRRAS on titania as a complementary technique for thermal desorption and density functional theory (DFT) to identify surface bound intermediates and, therefore, to study chemical reactions on the surface.

The IRRAS results presented in this thesis give for the first time strong experimental evidence for key intermediates in surface reactions and, thus, provides a new and unique perspective on the surface chemistry on titania. Furthermore, the importance of other factors such as the often neglected defect density and the role of coadsorbed oxygen is investigated. The insights on the impact of these factors help to understand differences between model systems, like the UHV study presented herein, and experiments under ambient conditions.

2 Methods

In this chapter, the methods used in this work to study the reaction mechanism on titania are presented. After a brief motivation for the need of doing experiments in ultra high vacuum a special focus is pointed to temperature programmed desorption and reaction and infrared reflection absorption spectroscopy due to their importance for this work.

Unfortunately, this chapter cannot cover all methods currently used in the surface science of titania, such as scanning probe microscopy or electron spectroscopy. A good overview for these methods is given in *Surface Science - Foundations of Catalysis and Nanoscience* by Kurt W. Kolasinski^[22] and *Surface Analysis - The Principal Techniques* by John C. Vickerman and Ian S. Gilmore.^[23]

2.1 Ultra high vacuum (UHV)

As discussed in the introduction, a simple model system is needed to understand the individual reaction steps involved in a catalytic process: the herein used model system is a rutile titania single crystal examined under ultra high vacuum (UHV) conditions:

To prepare a clean, adsorbate free surface the sample needs to be held at pressures in the order of $p < 1 \cdot 10^{-10} \text{ mbar}$.^[22] The impact rate Z of gas molecules is given by equation 2.1, where m is the particle mass, k_B is the Boltzmann constant and T is the temperature. For nitrogen, assuming a surface density of $10^{19} \text{ atoms m}^{-2}$, at a pressure of 10^{-6} mbar each surface atom is roughly hit once every second.^[22,24]

$$Z = \frac{p}{\sqrt{2\pi m k_B T}} = 2.88 \cdot 10^5 \frac{p}{\text{mbar}} \text{ ML/s} \quad (2.1)$$

The surface needs to be kept clean for the duration of an experiment in the order of 2 h (7200 s). Therefore, the pressure has to be in the 10^{-10} mbar range. The vacuum system used in this work is described in section 3.3 on page 24.

A prominent example for the challenge of preparing clean surfaces is work

published by Schaub et al.^[25] The authors reported an oxygen mediated diffusion mechanism for oxygen vacancies based on scanning tunneling microscopy (STM) results. However, further experiments showed that they actually observed the diffusion of water molecules, which adsorbed from the background water pressure in the used UHV system.^[26] Thus preparing a clean surface is challenging, even in UHV.

2.2 Temperature programmed desorption (TPD)

Temperature programmed desorption (TPD) also known as thermal desorption spectroscopy (TDS) is a versatile method for probing adsorption sites of a sample such as a single crystal surface in UHV. A probe molecule such as CO is dosed on the sample which is then heated in front of a mass spectrometer which in turn detects desorbing molecules. The integrated area, the peak temperature and shape of the desorption peak yields information about the relative abundance of different adsorption sites, desorption energies and desorption kinetics. This information is critical for understanding the surface chemistry on various materials.^[27] Temperature programmed reactions spectroscopy (TPRS) studies chemical reactions of adsorbed molecules on surfaces as in the case of benzaldehyde on rutile(110), which reacts to form stilbene and is discussed in detail in this work.^[28]

Kinetic model for thermal desorption

The desorption rate is detected by monitoring the adsorbate's partial pressure. If the pumping speed is sufficiently high, the partial pressure is proportional to the desorption rate. Otherwise the desorbing molecules accumulate in the vacuum system, and the desorption rate is proportional to the change in pressure. In most cases the pumping speed is high enough and only some accumulation of molecules is observed. This accumulation leads to a slightly increased partial pressure following the desorption peak which is known as the pump tail. The temperature dependent desorption rate $r(T)$ of an adsorbed molecule is given by the Polanyi-Wigner equation (equation 2.2)^[22,29,30]. This equation is derived from the Arrhenius equation for chemical reactions in solution.^[24] Desorption kinetics are typically of first order. Zero order reactions are often observed for condensed multi layer desorption and second order for desorption

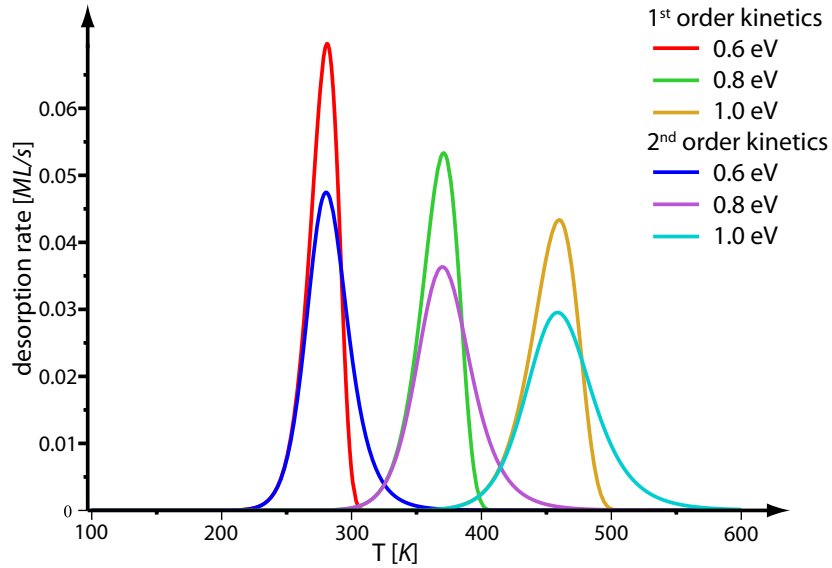


Figure 2.1: TPD desorption maximum shifts to higher temperatures with increasing desorption energy. The desorption rate reaches a maximum with increasing temperature according to the exponential term in equation 2.2 and falls to zero due to depletion of the adsorbate. For second order desorption kinetics this leads to a more symmetric peak shape.

TPD spectra for different desorption energies were calculated using an initial coverage of $\theta(0) = 1 \text{ ML}$ (mono layer), a frequency factor $\nu = 10^{10} \text{ s}^{-1}$ and a heating rate $\beta = 2 \text{ K s}^{-1}$.

processes which involve recombination of adsorbed species.

$$r(T) = -\frac{d\theta}{dT} = \frac{\nu}{\beta} \theta^n \exp\left(-\frac{E_{des}}{RT}\right) \quad (2.2)$$

E_{des} – activation energy for desorption

θ – surface coverage

ν – frequency factor

β – heating rate

n – order of desorption kinetics

R – ideal gas constant: $8.31447 \text{ J mol}^{-1} \text{ K}^{-1}$

TPD spectra are plots of the desorption rate versus the sample temperature and show peaks for each desorbing species (figure 2.1). The peak shape is a result of adsorbate depletion from the surface. For low temperatures ($RT \ll E_{des}$) the exponential term dominates equation 2.2. With increasing temperature the desorption rate reaches its maximum. Since with desorption, the surface coverage θ is consumed, the desorption rate falls to zero. The trail-

2 Methods

ing edge is steeper for zero and first order desorption kinetics than for second order kinetics, as in the latter case the desorption rate decreases faster and, therefore, the surface coverage is depleted more slowly.

The peak temperature depends on the desorption energy and the frequency factor. Increasing the desorption energy and the heating rate or decreasing the frequency factor decreases the desorption rate in equation 2.2. Thus the surface coverage depletes more slowly: The peak maximum shifts to a higher temperature and the peak gets broader (figure 2.1). If the peak temperature T_p shifts with the initial coverage of the adsorbate θ_0 , either the desorption energy depends on the coverage or the desorption is due to second order reaction kinetics. In the latter case $\log(\theta_0 T_p^2)$ correlates linearly with $\frac{1}{T_p}$.^[29]

Thermal desorption analysis

A key aspect of interpreting TPD spectra is determining the desorption energy and frequency factor from the observed peaks. This section introduces three different methods:

Redheads method estimates the desorption energy of an adsorbate based on the peak temperature T_p .^[29] Redhead observed that for first order reaction kinetics, the peak temperature depends in good approximation linearly on the desorption energy. With an estimate for the frequency factor, it is determined using equation (2.3).

$$\frac{E_{des}}{RT_p} = \ln \frac{\nu T_p}{\beta} - 3.64 \quad (2.3)$$

This method is frequently used since it is very simple, even though it depends on an estimate for the frequency factor. The desorption energy is determined independent of coverage from a single TPD spectrum. An appropriate estimate for the frequency factor is needed for this method, most commonly $\nu = 10^{13} \text{ s}^{-1}$ is assumed.^[31,32] However, since the desorption energy scales only logarithmically with the frequency factor in equation 2.3, the deviations are small and tolerable.

Falconer and Madix^[32] proposed a method for determining the desorption energy and the frequency factor from a series of TPD spectra with variable heating rate. For accurate results, the heating rate needs to be varied by typically two orders of magnitude. The variable heating rate is experimentally challenging: For low heating rates the peaks get broader, and the signal to noise ratio becomes an issue. On the other hand, when using a high heating rate, the pumping speed is a limiting factor.

Comparing various different analysis methods on numerically simulated TPD

spectra, Jong and Niematsverdriet^[31] showed, that only a full analysis of TPD spectra gives accurate results for the desorption parameters.^[30] Especially coverage dependent desorption energies and frequency factors falsify the results of simpler methods.

However, considering further accuracy issues such as the temperature calibration or a constant heating rate, the simple methods are sufficiently accurate. In the simulated spectra which were examined by Jong and Niemantsverdriet, the desorption energy determined by Redheads method was to within 6% of the correct value though a frequency factor was used that is off by a factor of 10.^[31] Falconer and Madix method is even more accurate and additionally determines the frequency factor.^[31]

Quantification of TPD spectra

The integrated peak area in TPD spectra is proportional to the amount of desorbing molecules. Quantification in TPD is typically done by using an external standard.^[33] The coverage is determined by comparing the integrated signal to a saturated mono layer of the adsorbate. Alternatively the absolute amount of desorbing molecules is obtained by calibration with a well known reference system such as Pt(111).

If a mixture of adsorbates coexist on the surface, for example as a result of a reaction, the different sensitivities of the mass spectrometer for each adsorbate need to be taken into account. The sensitivity depends on the fragmentation probability, the ionization cross section, the mass depending pass-function of the mass filter and the sensitivity of the detector.^[35,36] Especially for quadropole mass spectrometers, the latter two functions discriminate high mass fragments. The sensitivity depends on the used device, e.g. some mass spectrometers, such as the Hiden HAL/3F RC 301 PIC, use pre-focusing filters to reduce the discrimination effect (figure 2.2).

The relative sensitivity is obtained by recording the fragmentation pattern of the substance. This pattern is obtained either by leaking the adsorbate into the UHV system or by analyzing TPD spectra of each fragment from multilayer desorption. The first method is easier and does not rely on observation of multilayer signals. However, the second method benefits from being able to distinguish between adsorbate and impurities, which would desorb at a different temperature. A different desorption temperature of the expected fragments would further indicate decomposition of the adsorbate prior to adsorption. Finally, using the second method, the maximum pressure of the substance is lower in the UHV system compared to background exposure, which prevents

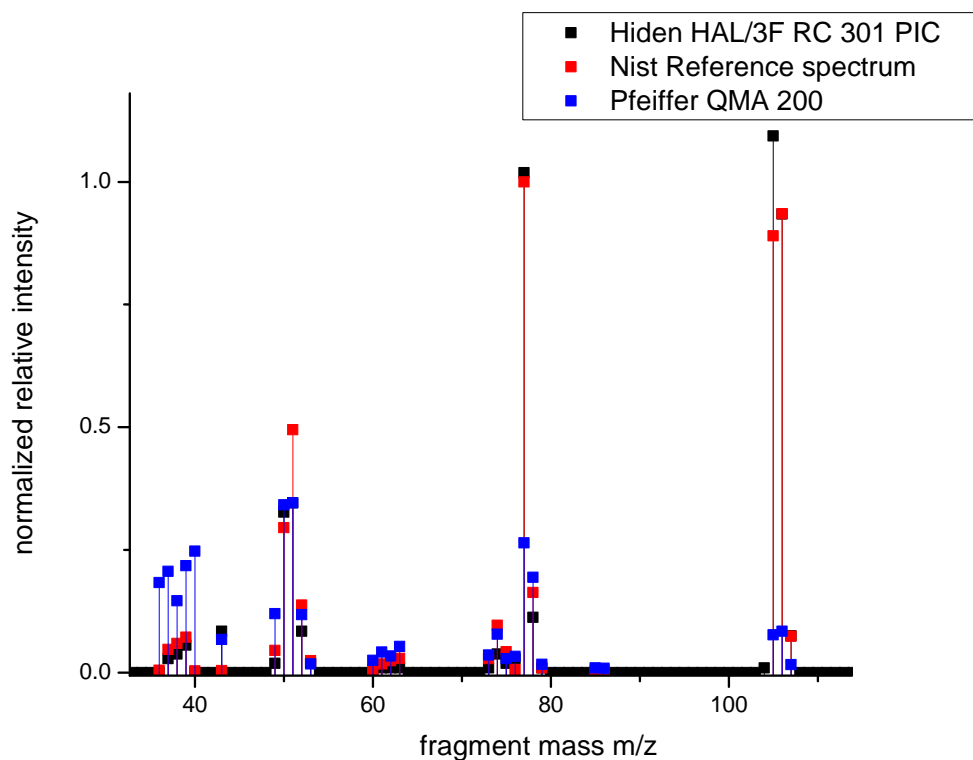


Figure 2.2: A simple quadrupole mass filter such as Pfeiffer QMA 200 used in this work discriminates high mass fragments (e.g. $m/z=77$, 105, 106), the Hiden HAL/3F PIC, a quadrupole mass spectrometer with a triple filter and pulsed ion counting set-up reproduces the NIST reference spectrum more closely.^[34] The graph shows a normalized benzaldehyde fragmentation pattern obtained as mentioned in the text. The Pfeiffer and Hiden intensities are normalized on m/z 51 to better illustrate this effect.

contamination issues.

Temperature programmed reaction spectroscopy (TPRS)

An extension of TPD, which takes reactions on the surface into account, is the temperature programmed reaction spectroscopy (TPRS).^[37] In contrast to TPD, desorption occurs due to a reaction of a surface bound species and not exclusively by thermally activated desorption.

In TPRS, the reaction activation energy is deduced from the peak temperature in a similar way as for the desorption energy in TPD. Similar to the Polanyi-Wigner equation, the surface reaction kinetics is described by an Arrhenius equation similar to eq. 2.2. Within this approach the desorption energy in the exponential term is replaced by the activation energy of the reaction. A high initial surface coverage accelerates a second order reaction, which shifts the

desorption maximum to lower temperatures. The determination of the exact reaction stoichiometry is challenging: As discussed in the previous section the detection sensitivities for the different reaction products need to be taken into account. Furthermore, the reaction products and desorbing unreacted educts often have common fragments which are superimposed in the recorded mass spectra.

A similar peak temperature and shape of two products indicates a common precursor species. The rate limiting step in desorption in this case is the activation of the intermediate. For example in the case of the reductive coupling of benzaldehyde discussed in chapter 5, a stilbene diolate intermediate forms on the surface. Upon heating to 485 K this intermediate reacts either releasing stilbene or dissociates and desorbes as benzaldehyde. Fragments of both molecules are observed in TPRS with a slightly different peak temperature (see figure 5.2).

A sharp desorption signal at high temperatures suggests an auto catalytic process. Usually desorption signals get broader with increasing peak temperature (figure 2.1). In some cases a reaction product, which is still bound to the surface, catalyzes the reaction. This additional catalyst lowers the activation energy which exponentially increases the reaction rate as more of the catalyst is formed. The result is a sharp desorption signal observed in the spectra.

2.3 Infrared reflection absorption spectroscopy (IRRAS)

In heterogeneous catalysis, vibrational spectroscopy is often used to study the binding of an adsorbate to a surface. Compared to other techniques, such as high resolution energy electron loss spectroscopy (HREELS) and Raman spectroscopy, the advantage of infrared (IR) spectroscopy is being applicable from UHV conditions to ambient pressures while having good absorption cross sections.^[38–41] IR spectra are recorded in transmission, in specular reflection e.g. from single crystal surfaces (infrared reflection absorption spectroscopy, IRRAS), diffuse reflection from powder samples or by attenuated total reflection (ATR). IR spectroscopy further benefits from a long experience in studying chemical structures in liquids and gases.^[42,43] Fourier transform infrared spectrometers (FTIR), where the entire spectral range is recorded simultaneously, allow a faster measurement with higher intensities and better signal to noise ratio.^[44]

A challenge when using IRRAS on single crystals is the low density of dipoles

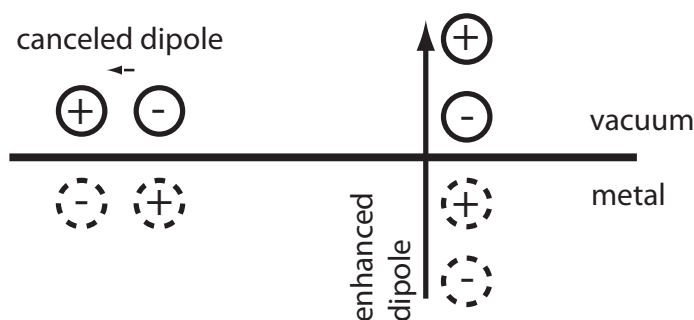


Figure 2.3: The metal surface selection rule - On metal surfaces a dipole on the surface induces an image dipole in the metal which leads to cancellation for dipoles parallel to the surface and enhancement for dipoles perpendicular to the surface.

on the surface. Therefore, IRRAS was limited to metal substrates, possibly covered with thin oxide films, which benefit from resonant enhancement.^[39] This enhancement is due to an image dipole, which is induced by the adsorbate in the free electron gas of the metal. This image dipole increases the absorption cross sections for perpendicular alignment to the surface but cancels dipoles aligned parallel to the surface (figure 2.3). Another explanation is based on the electric fields at the interface: For p-polarized light at grazing incidence the electric field vectors sum up and give almost twice the field strength perpendicular to the surface while the components parallel to the surface (s-polarized) cancel each other. The "metal surface selection rule" is commonly stated as only molecules with a component of the dynamic dipole moment aligned perpendicular to the surface are observed in IRRAS. Since dielectric surfaces such as titania lack resonant enhancement and reflect poorly, IRRAS on these substrates is challenging and only recently is possible due to optimized experimental setups.^[45–55] The dielectric surface selection rules are more complex than for metals and are discussed based on the three layer model in the next section.

Three layer model

The most commonly used model for describing reflection from a thin adsorbate film is the three layer model.^[48,56–61] The system is defined by three media (figure 2.4): vacuum, adsorbate and substrate, which are separated by sharp boundaries. The z -direction is perpendicular to the interfaces and the media are invariant in the x - and y - directions. The plane of light incidence is the x,z -plane. For simplification, the vacuum and substrate layers are characterized by isotropic dielectric constants ϵ_v and ϵ_s and are assumed to be semi-infinite.

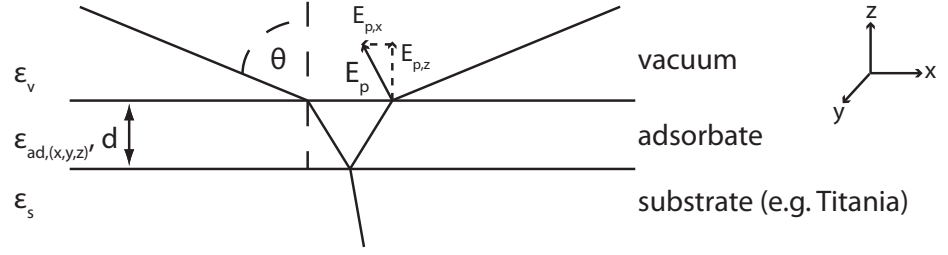


Figure 2.4: Illustration of the three layer model - The three layer model is used to describe reflection from a thin film on a substrate. The system consists of three layers: vacuum, adsorbate and the substrate, with the z direction perpendicular to the stacking, and the xz -plane as the plane of incidence. The vacuum and substrate layers are characterized by an isotropic dielectric constant ϵ_v and ϵ_s , the adsorbate film by a dielectric constant in x,y and z -direction $\epsilon_{ad,(x|y|z)}$ and a film thickness d . The electric field for s -polarized light is perpendicular to the plane of incidence (y -direction, not shown), for p -polarized light the electric field is aligned parallel to the plane of incidence and has x and z components ($E_{p,x}$ and $E_{p,z}$) depending on the angle of incidence θ .

The adsorbate layer of thickness d is anisotropic, with dielectric components for each direction $\epsilon_{ad,(x|y|z)}$. All media are assumed to be non-magnetic, thus their magnetic susceptibility is $\mu = 1$.

The electric fields of the incident, reflected and transmitted light are modeled as plane waves (eq. 2.4),

$$\vec{E}(\vec{r}, t) = \vec{E}_0 \cdot \exp(i\vec{k} \cdot \vec{r} - i\omega t) \quad (2.4)$$

where \vec{r} is the position vector, t is the time, \vec{k} is the wave vector (a vector in direction of propagation of magnitude $\frac{\omega}{c}$) and ω is the angular frequency. Two polarization states of the electric field are distinguished: The electric field of s -polarized light is aligned perpendicular to the plane of incidence, the electric field vector \vec{E} has therefore only a y component. P -polarized light is parallel to the plane of incidence, the electric field vector has a x and a z component (figure 2.4). To account for absorption, the dielectric constant of the adsorbate is complex, which results in a complex wave vector. Therefore the exponent in equation 2.4 has an additional real and negative term.

The wave equation of a plane wave is derived from Maxwell's equations:

$$\vec{k} \times (\vec{k} \times \vec{E}) + \omega^2 \mu \epsilon \vec{E} = 0 \quad (2.5)$$

2 Methods

Furthermore, the electric field must be continuous in a charge free system as follows from Gauss law. This leads to the usual boundary conditions at a dielectric surface, where the sum of the tangential electric and magnetic fields must be zero and the displacement $\vec{D} = \epsilon\vec{E}$ perpendicular to the surface must be continuous. Solving equation 2.5 under these conditions for the three layer system gives reflective coefficients for s- and p-polarized light (r_s and r_p , eq. 2.6 and 2.8).^[56] The dielectric constant of the substrate was assumed to be real, therefore, these equations do not apply to metal surfaces, for details see reference.^[56] A more general approach using (4 x 4) matrices, which accounts for anisotropy in the other media and is expandable to multilayer systems, was developed by Pochi Yeh.^[62-64]

$$r_s = r_{s,0} \cdot \left(1 + 2i \frac{\omega}{c} d \cdot \sqrt{\epsilon_v} \cos \theta \cdot \frac{\epsilon_s - \epsilon_{ad,y}}{\epsilon_s - \epsilon_v}\right) \quad (2.6)$$

$$r_{s,0} = \frac{\sqrt{\epsilon_v} \cos \theta - \sqrt{\epsilon_s - \epsilon_v \cdot \sin^2 \theta}}{\sqrt{\epsilon_v} \cos \theta + \sqrt{\epsilon_s - \epsilon_v \cdot \sin^2 \theta}} \quad (2.7)$$

$$r_p = r_{p,0} \cdot \left(1 + 2i \frac{\omega}{c} d \sqrt{\epsilon_v} \cos \theta \frac{(\epsilon_s - \epsilon_{ad,x}) - \left(\frac{\epsilon_s}{\epsilon_{ad,z}} - \frac{\epsilon_{ad,x}}{\epsilon_s}\right) \epsilon_v \sin^2 \theta}{(\epsilon_s - \epsilon_v) - \left(\frac{\epsilon_s}{\epsilon_v} - \frac{\epsilon_v}{\epsilon_s}\right) \epsilon_v \sin^2 \theta}\right) \quad (2.8)$$

$$r_{p,0} = \frac{\epsilon_s \sqrt{\epsilon_v} \cos \theta - \epsilon_v \sqrt{\epsilon_s \left(1 - \frac{\epsilon_v}{\epsilon_s} \sin^2 \theta\right)}}{\epsilon_s \sqrt{\epsilon_v} \cos \theta + \epsilon_v \sqrt{\epsilon_s \left(1 - \frac{\epsilon_v}{\epsilon_s} \sin^2 \theta\right)}} \quad (2.9)$$

Calculated absorption curves for titania (figure 2.5) show complex selection rules: Absorption for s-polarized light is always negative, but for p-polarized light depending on the angle of incidence and orientation of the adsorbate gives negative and positive peaks. For grazing incidence, p-polarized absorption is negative for isotropic and z-oriented adsorbates, but positive for x-oriented adsorbates. All graphs have a pole at the Brewster angle at 68°. Brunner et al.^[65] got similar results for silicon using the matrix approach by Yeh, as well did Buchholz et al.^[55] for ZnO.

The calculations were done assuming a model adsorbate of thickness $d = 0.2$ nm and refractive index $n_{ad} = 1.5 + 0.1i$ ^[65] at wave number $\tilde{\nu} = 3000$ cm^{-1} . The substrate's refractive index is $n_s = 2.451$ for titania (value for the ordinary ray, $n^2 = \epsilon$ and $\omega = 2\pi c\tilde{\nu}$).^[66] Isotropic and oriented absorption were modeled by using the complex dielectric constant for the according component, and the real part for all other components.

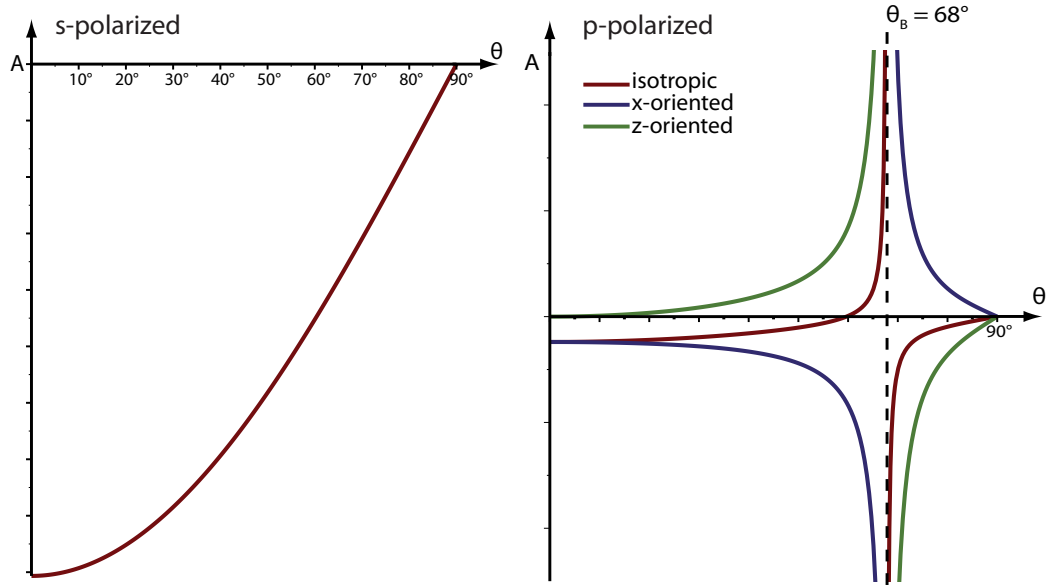


Figure 2.5: Calculated absorption based on 3 layer model for s- and p-polarized light for reflection on rutile TiO_2 - For s-polarized light absorption is negative independent of angle of incidence (θ). P-polarized light shows a more complex behavior: Absorption curves have a pole at the Brewster angle ($\theta_B = 68^\circ$). For larger angles the x-oriented adsorbates show positive, isotropic and z-oriented show negative absorption.

Microscopic interpretation of dielectric constants

The three layer system is a macroscopic model in which all information about the adsorbate is contained in its dielectric constant ε (and the film thickness d). Microscopical vibrations are described by the harmonic oscillator model.^[24] These oscillators are driven by the external electric field of the incident light, which is described by the Lorentz oscillator model.^[57,61,67] Therefore, this model is used to link the microscopic properties of the harmonic oscillator with the macroscopic dielectric constant of the adsorbate film. The wave equation for the Lorentz oscillator is

$$E(x) \cdot q = m \left(\frac{d^2x}{dt^2} + \gamma \frac{dx}{dt} + \omega_0 \cdot x \right) \quad (2.10)$$

q and m are the effective charge and mass of the oscillator and x is the oscillators displacement from the equilibrium position. The second term on the right side accounts for attenuation of the oscillation. The attenuation constant γ and the eigenfrequency ω_0 are obtained from quantum mechanical solutions of the harmonic oscillator. Assuming the electric field is described by a plane wave (eq. 2.4), the solution to eq. 2.10 will have the same form

2 Methods

e.g. $x(t) = x_0 \cdot \exp(-i\omega t)$. The polarizability α , which is the displacement of charge induced by an electric field is then:

$$\alpha(\omega) = \frac{q \cdot x_0}{E} = \frac{\frac{q^2}{m}}{\omega_0^2 + i\gamma\omega - \omega^2} \quad (2.11)$$

The imaginary term in equation 2.11 is due to the attenuation term in eq. 2.10 ($\frac{dx}{dt}$ is imaginary). This will result in a complex dielectric constant, a complex wavevector \vec{k} and ultimately the real and negative exponential term in equation 2.4 which was discussed above. Therefore, the microscopic quantity describing absorption is the oscillators attenuation constant. For a macroscopic system, the total polarizability is composed of the sum of individual polarizabilities and an electronic contribution α_0 , which is generally assumed to be constant for IR-frequencies:^[61]

$$\alpha(\omega) = \alpha_0 + \sum_j \frac{\frac{q_j^2}{m_j}}{\omega_0^2 + i\gamma\omega - \omega^2} \quad (2.12)$$

Finally, the dielectric constant is obtained using the Clausius-Mossotti equation (eq. 2.13) where N is the density of dipoles per volume.^[61]

$$\varepsilon(\omega) = 1 + \frac{4\pi N\alpha(\omega)}{1 - \frac{4\pi N\alpha(\omega)}{3}} \quad (2.13)$$

D-parameter theory

The three layer model is based on the assumption of sharp boundaries at the interfaces. This assumption is problematic due to the boundary interpretation at the atomic scale and when considering sub-monolayer coverages of the adsorbate.^[68] Furthermore, a sharp boundary implies a discontinuity in the electric field perpendicular to the surface, a surface charge, which plays an import role in plasmon excitation and applications based on it, such as surface enhanced Raman spectroscopy (SERS).

Another approach for describing reflection from a covered surface circumventing these issues is the d-parameter theory developed by Feibelman.^[68-70] It is based on a perturbation based approach and does not rely on the assumption of sharp boundaries. The electric field in a volume at the interface is evaluated as a linear combination of the electric fields of the surrounding media, the so called reference field. This field has a discontinuity of the tangential field components at the interface, which is compensated by correction terms. These terms are obtained by multiplying the reference field with the so called d-parameter matrix.^[70] Absorption in x-, y- and z-direction depends on the

diagonal elements of this matrix d_x , d_y and d_z , which depend on the wavelength. Based in this theory, the complex reflection amplitude for s-polarized light is: ^[53,69]

$$\frac{r_s}{r_s^0} = 1 + i \frac{4\pi \cos \theta}{\lambda} d_y \quad (2.14)$$

and for p-polarized light:

$$\frac{r_p}{r_p^0} = 1 + i \frac{4\pi \cos \theta}{\lambda} \cdot \left(\frac{d_z(\epsilon_1 \cdot \sin^2 \theta_{in}) - d_x \cdot (\epsilon_1 - \sin^2 \theta_{in})}{\sin^2 \theta_{in} - \epsilon_1 \cos^2 \theta_{in}} \right) \quad (2.15)$$

The d-parameters are obtained in a similar way as for the 3-layer model: for discrete dipoles on the surface they are proportional to the induced dipole moments p which are calculated from the polarizability and the effective electric field at the interface. For details and numerical examples see reference. ^[69] Absorption depends on the imaginary part of the d-parameters. ^[53]

Considering the imaginary parts of the d-parameters, the terms for the y and z component in equations (2.14 and 2.15) are negative, whereas the x component for p-polarized light is positive. ^[53] Therefore, d-parameter theory reproduces the surface selection rule for dielectric surfaces derived in the previous section.

2.4 Low energy electron diffraction (LEED)

Low energy electron diffraction (LEED) is a method to characterize the structure of a surface, which is based on the diffraction of electrons. ^[22,23,71–73] Electrons behave like waves and, therefore, are diffracted at the surface lattice of a crystalline sample, similar to light at a grating. The wavelength λ of any particle wave is tuneable based on the kinetic energy E_{kin} as given by the de Broglie relation (equation 2.16, h : Planck's constant, m_e : mass of an electron).

$$\lambda = \frac{h}{\sqrt{2m_e E_{kin}}} \quad (2.16)$$

In contrast to e.g. x-ray diffraction, this method is surface sensitive due to the low inelastic mean free path length of electrons in solids. For example in rutile titania, the path length is in the order of 0.5 to 1 nm at energies, which are typically used in LEED (50 to 350 eV). ^[74]

In this work, LEED is used to assess the cleanness of the used rutile(110) crystal, to check for a [2x1] reconstruction, which will form if the crystal is heavily reduced, and to identify the orientation of the crystal axis. An example for a diffraction pattern obtained during this work is given in figure 3.2 on page 26. It shows the [1x1] reconstruction with a rectangular unit cell.

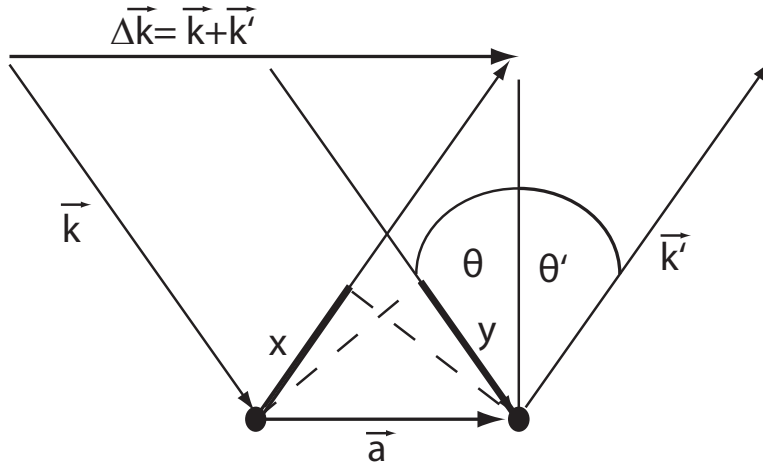


Figure 2.6: Laue Diffraction: A diffraction spot is observed when the reflected electron waves are in phase. This condition is satisfied when the path difference $x-y$ equals an integral multiple of the wave length.

A diffraction spot is observed in the LEED pattern when constructive interference occurs between scattered electron waves. The geometry is illustrated in figure 2.6: The two dimensional surface lattice is spanned by the two basis vectors \vec{a}_1 and \vec{a}_2 . The sum of the incident electron wave vector \vec{k} and the scattered wave vector \vec{k}' is the scattering vector $\vec{\Delta k}$. Constructive interference for a scattering vector $\vec{\Delta k}$ occurs when the path difference $y-x$ equals an integral multiple of the wavelength.

The scattering vectors that fulfil the condition for constructive interference, form a two dimensional vector space. This space is spanned by the basis vectors \vec{g}_1 and \vec{g}_2 , which are obtained from the lattice basis vectors according to equation 2.17. (\bullet marks the scalar product of two vectors: $\vec{x} \bullet \vec{y} = |\vec{x}| |\vec{y}| \cos \angle(\vec{x}, \vec{y})$)

$$\begin{aligned} \vec{a}_i \bullet \vec{g}_j &= 2\pi \delta_{i,j} \\ \delta_{i,j} &= \begin{cases} 1, & i = j \\ 0, & i \neq j \end{cases} \end{aligned} \quad (2.17)$$

Equation 2.17 indicates that the obtained basis vectors \vec{g}_i are proportional to the reciprocal length of the corresponding lattice basis vectors \vec{a}_i . Therefore, this vector space is called the *reciprocal space*. Furthermore, as $\cos(\pi) = 0$, the reciprocal basis vectors are orthogonal to the non corresponding lattice basis vector ($i \neq j$). The experimental setup for LEED is designed to show a diffraction pattern, which is a projection of this reciprocal vector space.

The rutile(110)[1x1] reconstruction has a rectangular unit cell with an orthogonal basis. Therefore, the reciprocal vectors are parallel to the corresponding

lattice vectors but their length is inverted. Thus, the observed diffraction pattern appears to be rotated by 90° with respect to the surface lattice.

2.5 Density functional theory (DFT)

Density functional theory (DFT) is a method for calculating the electronic structure of molecules.^[75–78] These calculations are used within this work to complement the experimental data: for example the calculation results are used to identify reaction intermediates observed in chapter 6.

As the name implies, DFT is based on evaluating a functional of the electron density. A functional is like a function except that it assigns a value to an argument function whereas a function assigns a value to a (list of) argument values. Functionals are often distinguished from functions by using square brackets instead of round brackets for the argument list (e.g. $E[\rho(r)]$).

DFT is based on the proof by Hohenberg and Kohn,^[79] who showed that all ground state properties of a molecule can be calculated from the electron density distribution. However, the exact form of the functional to do this is not known. Therefore, DFT uses a fundamentally different approach than Hartree Fock (HF) and other computational methods based thereon, which use molecular orbitals to determine the electronic properties. The advantage of DFT is that it provides sufficiently accurate results for most applications at a computational cost which is similar to HF. This advantage is based on the implicit treatment of the electron correlation. However, as the exact form of the functional is not known, DFT relies on empirical approximation.

In the approach by Kohn and Sham (KS),^[80] the electron density is obtained from one-electron orbitals ψ_i , the KS orbitals. Though these KS orbitals are treated like molecular orbitals, and are obtained in a similar way like molecular orbitals in a HF calculation, they do not represent molecular orbitals and are merely a means to obtain the electron density. The electron density $\rho(r)$ is the sum of the square of the absolute value of all occupied ground state orbitals as indicated in equation 2.18. The ground state electronic energy $E[\rho]$ is given by equation 2.19.

$$\rho(r) = \sum_{i=1}^N |\psi_i(r)|^2 \quad (2.18)$$

$$E[\rho] = E_{kin}(\psi_i) - V_{en}[\rho] + V_{ee}[\rho] + E_{XC}[\rho] \quad (2.19)$$

The kinetic energy $E_{kin}(\psi_i)$ is calculated from the KS orbitals in a similar way as it is obtained from the molecular orbitals in a HF calculation. The

2 Methods

electron-nuclei interaction $V_{en}[\rho]$ and the electron-electron interaction $V_{ee}[\rho]$ are calculated from the electron density and are described by coulomb interaction. However, the last term in equation 2.19, the exchange correlation energy ($E_{XC}[\rho(r)]$), which describes all purely quantum mechanical electron-electron interactions, is not known and this is where approximations are introduced. Typically, this term is separated in an exchange term ($E_X[\rho(r)]$) and a correlation term ($E_C[\rho(r)]$).

A simple approach for the exchange correlation functional is the local density approximation (LDA). It is based on the model of a homogeneous electron gas of constant density. This method fails when gradients in the electronic density occur. Therefore, within the generalized gradient approximation (GGA), correctional terms are introduced to account for density gradients.

Better results are obtained by using hybrid functionals. In this work the B3LYP functional is used. It is composed of a hybrid exchange function proposed by Becke^[81] (Becke three parameter, B3) and a gradient corrected correlation functional proposed by Lee, Yang and Parr (LYP).^[82] The B3 exchange functional is a linear combination of the exchange functional in the LDA approximation, a gradient correction term (GGA extension) and the exchange energy obtained by applying the exchange operator used in HF calculations on the KS orbitals.

For the calculation, the KS orbitals are modelled as a linear combination of basis functions. Typically, Gauss type orbital functions, which are shaped like atomic orbitals (s,p,d,f), are used. They are more easily computable than for example Slater type orbital functions. Gauss and Slater type basis function are the established functions used for various ab initio calculations including HF. Increasing the number of basis functions increases the flexibility of the calculation and, therefore, the accuracy of the result, but also the computational cost. Besides functions for each electron, extra functions are added to the basis to account for additional effects: As the electron basis functions can only shrink or expand, but not change their spacial distribution, they poorly reproduce a polarization of the molecule. The remedy for this issue are polarization functions with a lower symmetry. For example the polarization of a s-type orbital is accomplished by adding a p-type orbital. Furthermore, diffuse Gauss functions improve the modelling of long range electron distribution for example as in the case of electron lone pairs.

Within this work the basis sets 6-31+G(d,p) and 6-311+G(d,p) are used.^[83-85] These basis sets treat inner shell and valence electrons with different accuracy: inner shell electrons are in both cases represented by a single contracted Gauss function, which is a linear combination with fixed coefficients of 6 primitive

Gauss function. The valence electrons are described by two in the 6-31 and 3 Gauss functions in the 6-311 case. In each case one of the valence Gauss functions is a contraction of 3 primitive functions, whereas the other ones are not contracted. The + indicates extra diffuse Gauss function for each non-hydrogen atom in the system (s- and p-type functions). Additionally, the (d,p) indicates polarization functions: d-type Gauss functions for each non hydrogen atom, and p-type for each hydrogen atom.

The KS orbitals are determined using an iterative method. The calculation starts with an initial guess for the electron density, or more specifically a set of coefficients for the basis functions. Then a new set of KS orbitals is calculated based on the Kohn-Sham equations from this initial guess (see ref.^[75] for details). This cycle is repeated until the coefficients are constant within a certain tolerance with further iterations and the density function is consistent. This method is called a self consistent field calculation, which is also used for HF calculation.

3 Experimental details

This chapter describes the experimental setup and the processing of the recorded data.

3.1 UHV system

The experiments reported in the following chapters were performed in a home build vacuum system with a base pressure of less than 10^{-10} *mbar* (figure 3.1). Except for the sample holder, the system is mostly identical to the one described by Wille in detail.^[86] The vacuum recipient is pumped by turbo molecular pumps and a titanium sublimation pump (TSP) and rotary vane pumps as roughing pumps. To minimize oil diffusion, foreline traps filled with copper mesh or alumina beads were installed between the turbo molecular pumps and the roughing pumps.

The system is equipped with a low energy electron diffraction (LEED) optics equipped for Auger electron spectroscopy (Omicron SpectraLEED), a quadrupole mass spectrometer (Pfeiffer QMA200) for residual gas analysis and TPD/TPRS (section 2.2), a sputter gun (Omnivac PS-IQ12) for sample preparation and an IR-cell with CaF_2 -windows for IRRAS experiments (section 2.3). A load lock with a sample transfer system is attached to the system. The IR-cell is fitted into the sample compartment of a FT-IR spectrometer (Bruker IFS 66v/S) aligned for reflectance measurements. The IR setup will be described in detail below.

3.2 Samplmount

The single crystal sample was mounted on a 0.25 mm thick sheet of tantalum held by two screwed on clamps made from the same material. A piece of gold foil improved the thermal contact between the crystal and the sheet. The crystal's temperature was measured using a bar wire ultra thin type-K thermocouple (CHAL-005, Omega Engineering) glued in a hole on the side of the crystal with a ceramic adhesive (Ceramabond 569, Aremco).

For this work a mobile sample holder based on a previous design by Leist et

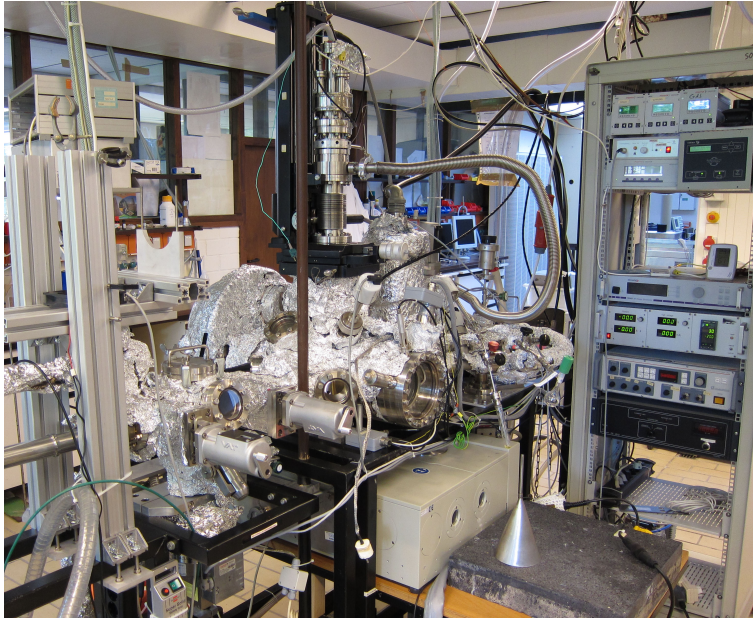


Figure 3.1: Photographic image of the used vacuum system.

al.^[87] was used. It allowed fast heating and cooling and changing samples without the need to break vacuum. The tantalum sheet with the crystal was mounted on two sapphire blocks, which in turn were supported on a copper sheet. This sheet was in thermal contact with a liquid nitrogen reservoir for cooling. A filament made from 0.2 mm tungsten wire was used for heating the sample by thermal radiation or electron bombardment. The filament was mounted between the sapphire blocks approximately 1-2 mm below the tantalum sheet. It was powered by a sample heating system (Bestec), which includes a PID-controller (Eurotherm) for TPD-experiments.

3.3 Sample preparation

The rutile(110) crystals were obtained from SurfaceNet GmbH. The crystals were 10 by 10 mm large, 1 mm thick, and delivered with a 0.3 mm hole on one side to attach the thermocouple. The crystals were cleaned by sonication in iso-propanol and mounted on the sample holder as described above.

In UHV, the crystals were cleaned by cycles of ion bombardment and tempering. The crystal was first bombarded by 1000 eV Ar^+ -ions at an ion current of $1 \mu\text{A}/\text{cm}^2$ at room temperature to remove adsorbates. This procedure has been known to preferentially remove oxygen from the top layer of the crystal and thus damage the surface.^[88] This damage was healed by tempering the crystal: The crystal was tempered using a PID-programm, which heated the crystal in 3 min to 600°C, held that temperature for 7 min and slowly cooled it

to 100°C in 10 min. During tempering, the surface was reoxidized by diffusion of excess Ti atoms into the bulk, which introduced defects.^[88] The defects are color centers, which turned the crystal from white to dark blue with increasing bulk reduction (see figure 5.6 on page 55). Starting with a fresh crystal, after approximately ten cycles a sharp LEED pattern was observed (see figure 3.2).

3.4 LEED

LEED was used in this work to check the quality of the crystals surface especially whether a [2x1] reconstruction has been formed, which would have indicated an over reduced crystal, and to identify the orientation of the crystal axis. LEED patterns were obtained using an Omicron Spectra LEED optics with electron energies in the range from 100 to 250 eV. The crystal was shifted in front of the optics to ensure that the obtained LEED pattern is representative for the surface over the entire crystal.

A typical LEED pattern of the crystal (figure 3.2) shows the [1x1] reconstruction of the (110) surface, which is known from literature (see figure 3.3 b).^[89] The sharp spots with little background indicate a well ordered clean crystal. The light dark areas between the spots in the middle of the crystal is due to reflection of external light. No indications of the [2x1] reconstruction were observed (figure 3.3 a).^[89]

The LEED pattern also indicates that the crystal is mounted with the $\langle 001 \rangle$ direction aligned vertically and the $\langle 1\bar{1}0 \rangle$ direction horizontally. As discussed in section 2.4, the observed LEED pattern is a representation of the reciprocal vector space, which appears to be rotated by 90° with respect to the surface lattice. The surface unit cell of rutile(110) is 2.96 Å in the $\langle 001 \rangle$ direction and 6.49 Å in the $\langle 1\bar{1}0 \rangle$ direction.^[90] Therefore, the short $\langle 001 \rangle$ direction appears as the long direction in the LEED pattern (figure 3.2), which is oriented vertically.

3.5 Doser

For studying their reactions on a surface, adsorbates need to adsorb onto the surface. Gases, like oxygen or CO, can simply be introduced by backfilling the UHV system using a variable leak valve. The standard exposure unit is the langmuir (L), which corresponds to an exposure at 10^{-6} torr ($1.33 \cdot 10^{-6}$ mbar) for one second.^[22] As the exact exposure of gases within this work is not critical, the approximation $1 \text{ L} \approx 10^{-6} \text{ mbar s}$ is used.

Backfilling the vacuum system is not recommended for vapors, e.g. of water

3 Experimental details

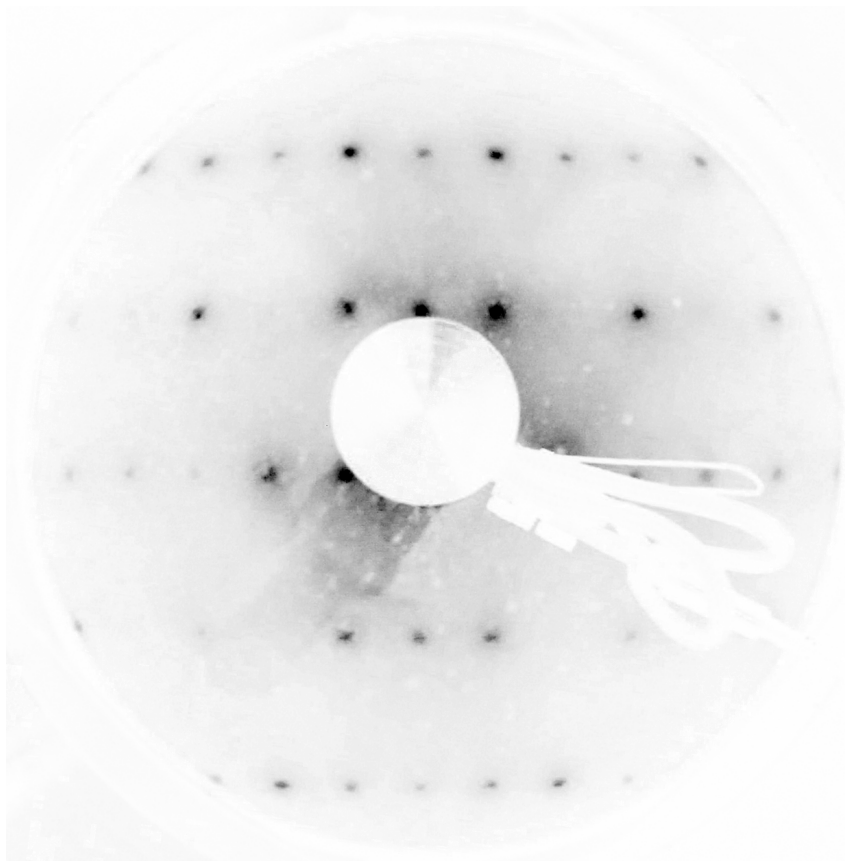


Figure 3.2: LEED diffraction pattern of the rutile(110)[1x1] reconstruction recorded at 227 eV. The pattern shows a rectangular unit cell, the $\langle 001 \rangle$ direction is vertical, the $\langle 1\bar{1}0 \rangle$ horizontal. The image was inverted, converted to black and white and optimized for brightness and contrast. The cylindrical object in the middle of the picture is the electron gun.

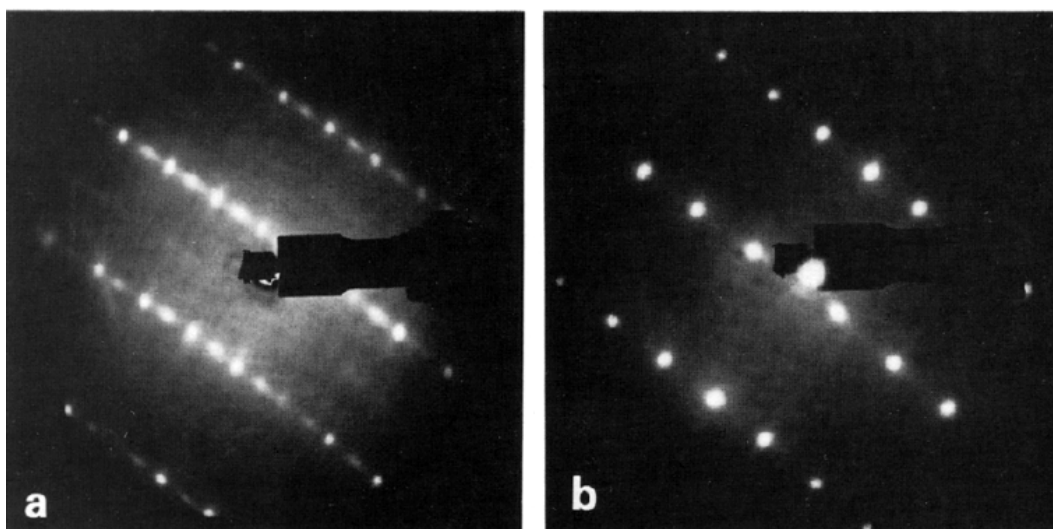


Figure 3.3: Rutile(110) LEED patterns of the a) [2x1] and b) [1x1] reconstruction recorded at 123.4 eV.^[89,91]

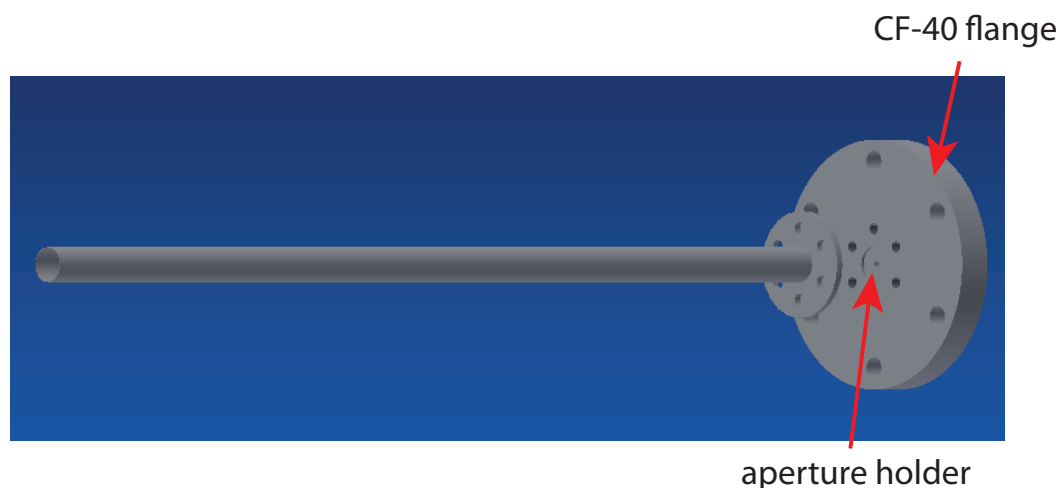


Figure 3.4: Explosion view of the used vapor doser - The adsorbate is confined onto the crystal by using a 300 mm tube. A SEM aperture is used as pin hole and clamped by the tube into the indentation in the aperture holder. The entire holder is mounted onto a linear shift for aligning the tube directly in front of the crystal.

or organic substances, such as benzaldehyde, acetone or methanol. These substances are not as easily removed by pumping as gases, because they stick to various surfaces within the UHV recipient at room temperature. This problem is often circumvented by using a tube in front of the leak valve, which confines the adsorbate onto the crystal surface. The amount of exposure is controlled by monitoring the pressure within the UHV system. If the sample is mounted on a bulky cooled sample holder, as it was the case in this work, the adsorbate would condensate on the sample holder and almost no pressure rise is observed in the main recipient. Thus, in this case, a method for dosing which relies on the pressure in the main recipient for quantification of the adsorbate flux is unreliable.

The above mentioned problems were circumvented by using a pin-hole doser as illustrated in figure 3.4. Due to the fixed pin-hole size, the leak rate is proportional to the pressure of the vapor on the high pressure side of the doser (typically 0.1 mbar in the experiments in this work). Thus, this method does not rely on a rise in pressure in the UHV system to determine the exposure. The pressure rise, which was observed in the main recipient in this work, was typically less than 10^{-10} mbar. An aperture with a diameter of $20 \mu\text{m}$, which was previously used in an electron microscope, was used as pinhole. It was clamped between a 300 mm pipe, which was pointed at the sample, and the aperture holder illustrated in figure 3.4. The aperture holder was mounted on a linear translator for alignment of the doser facing the sample.

The high pressure side of the doser was attached to the gas system illustrated

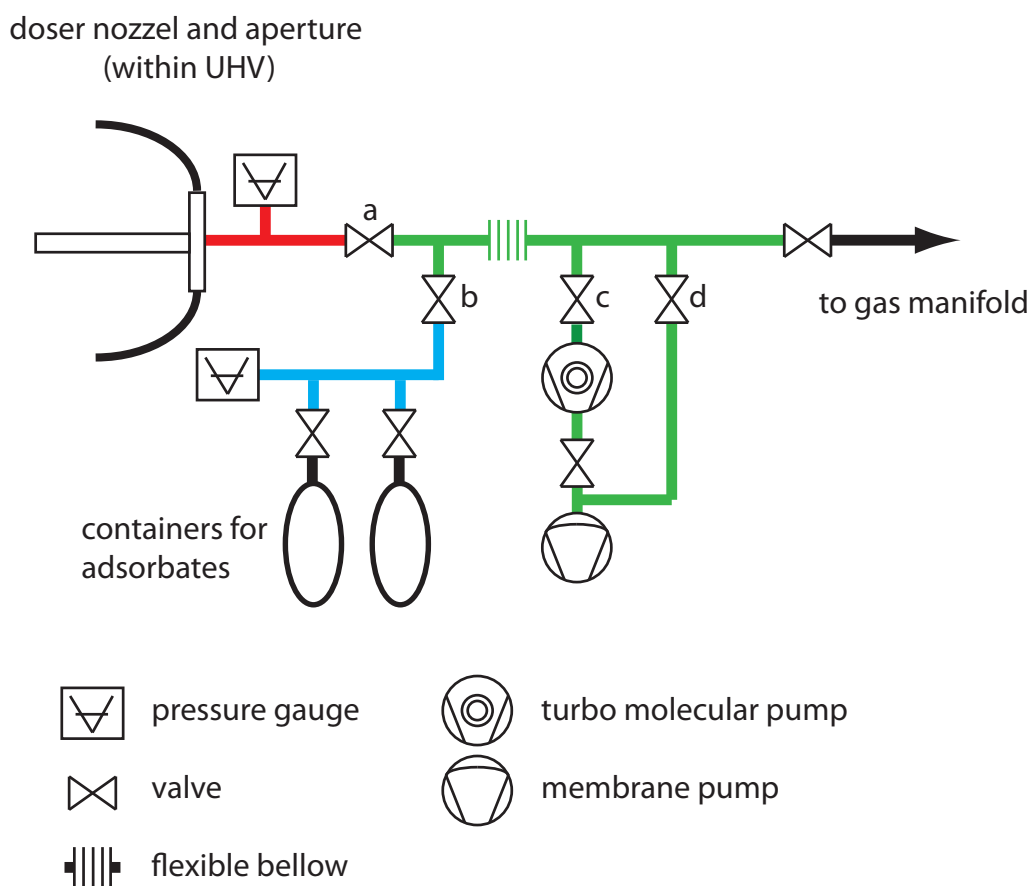


Figure 3.5: Schematics of the gas system used for dosing vapors - Dosing is started by filling the compartment in front of the pinhole (marked red), and stopped by evacuating this compartment. The containers with the substances (see figure 3.6) are attached to the organics manifold (light blue). The gassystem is pumped by a turbo molecular pump using a membrane pump as roughing pump. (marked green)



Figure 3.6: A glass flask used for dosing liquids. After freeze-pump-thaw-cycles the flask only contains the liquid and its vapor.

in figure 3.5. The compartment in front of the pin-hole (marked red) was filled or evacuated via valve a. A fixed pressure was set in the organics manifold (light blue) prior to dosing. To start dosing, the vapor was expanded into the compartment in front of the pinhole (valves a,b open, valves c,d closed), to stop dosing, the compartment was evacuated by opening valve c. This procedure improved the reproducibility of dosing, as the pressure in the compartment was not set during the initial time span of dosing as it would have been the case if a leak valve had been used to fill the compartment.

The vapor of the substances were introduced into the gas system in glass flasks as shown in figure 3.6. The substances were purified by repeated freeze-pump-thaw cycles: The contents of the flask was first frozen by submerging it in liquid nitrogen, then the flask was evacuated. After thawing the flask this procedure was repeated. After several cycles, the flask only contained the pure substance and its vapor. Air and more volatile contaminations were removed. Significantly less volatile contaminations, such as benzoic acid in the case of benzaldehyde, were of no concern, as they remained in the flask during dosing. The cleanness of the dosed vapor was judged based on the fragmentation patterns from mass spectrometry obtained as described in section 2.2.



Figure 3.7: Shielding of the mass spectrometer to reduce background contribution to the recorded spectra. The mass spectrometer is mounted on the CF-flange on the left with the ionization source and massfilter within the shielding. The openings on the left are for differential pumping of the spectrometer.

The herein presented method is limited to substances, which have a minimum vapor pressure of approximately 1 mbar. Some substances, such as stilbene or benzoic acid, could not be dosed using this method, because their vapor pressure is too low. To circumvent this problem, a molecular spray doser has been installed, which will be described in future work by Milena Osmić.^[92]

3.6 TPR spectra

TPR spectra were recorded with a Pfeiffer QMA200 at a heating rate of 2 K/s. The mass spectrometer was encapsulated in a shield with a 5 mm nozzle to reduce the influence of background desorption (figure 3.7). The shield had openings at the rear end for differential pumping of the mass spectrometer. The sample was heated using a linear heating ramp with a rate of 2 K/s. For this purpose, the power supply feeding the heating filament was regulated by a PID controller. The controller was programmed to start with an initial temperature step to 130 K to desorb any adsorbates from the heating filament and, therefore, to further reduce contribution to the background of the recorded TPR spectrum. The sample temperature was recorded using an auxiliary analog input of the mass spectrometer, which was fed by an output signal of the PID controller.

Typically, up to 20 fragments were recorded simultaneously during a TPRS experiment using the Quadstar software package.^[93] The software was set to cycle through the different masses, the signal of each mass being recorded for 20 ms during one cycle. Prior to the experiments, the mass scale of the mass spectrometer had been calibrated over the entire range based on fragments of benzaldehyde, ethyliodid and tungsten isotopes, which were emitted from the ionization source. The ionization source had been optimized to maximize the

CO₂ signal (m/z 44) from residual gas.

The quantification of reaction products from TPR spectra was done by interpreting the integrated desorption signal. Most of the desorption signals in TPR spectra were shifted by a constant offset due to a background signal or a pump tail of a desorption signal at a lower temperature. To account for this shift, a straight baseline was subtracted prior to integration of the desorption signal.

To compare various fragment signals the different fragmentation probability for each fragment, the mass dependent sensitivity and the ionization cross section of the molecules need to be taken into account as discussed in section 2.2. For some adsorbates the characteristic fragmentation pattern for the mass spectrometer used in this work could not be recorded, e.g. stilbene is not volatile enough to be dosed by the method mentioned above. Therefore, NIST reference spectra were used instead.^[34] To minimize the effect of the mass dependent transmission of the quadropole filter (see section 2.2), fragments with a similar mass were chosen to be compared. For example, the fragment m/z 102 for stilbene was used to be compared to the m/z 106 parent ion for benzaldehyde instead of the parent ion of stilbene (m/z 180). The integrated signals were corrected for the fragmentation probability $p(m)$, which is the probability that the fragment of mass m forms upon ionization.

$$p(m) = \frac{I(m)}{\sum I(m)} \quad (3.1)$$

$I(m)$ is the intensity of the fragment of mass m in the NIST reference spectrum. Equation 3.1 is based on the assumption, that exactly one charged fragment is observed for each ionized molecule. Therefore, it neglects e.g. multiple fragmentation and ionization events. Furthermore, the relative ionization cross section σ_{rel} of the molecules was taken into account. The relative amount of desorbant i , X_i characterized by fragment m is given by

$$X_i = \frac{A(m)}{p(m) \cdot \sigma_{rel}} \quad (3.2)$$

where $A(m)$ is the integrated area. The reaction yield Y_i is then obtained by relating the relative amount of the product i to the educts according to

$$Y_i = \frac{n_i \cdot X_i}{\sum n_i \cdot X_i} \quad (3.3)$$

where n_i are the stoichiometric factors. The denominator in equation 3.3 represents the total amount of the educt on the surface, based on the sum of the

unreacted educt and products.

This method for quantification is only used to estimate the yield. Especially, using the NIST fragmentation pattern and neglecting multiple ionization events limits the accuracy. However, these deviations are systematic. Therefore, even though the absolute yield is dubious, this method reproduces general trends.

3.7 IR spectra

IR spectra were recorded using a Bruker IFS 66v/S Fourier Transform IR spectrometer. The spectrometer was equipped with a global mid IR source and a mercury cadmium telluride (MCT) detector. The interferometer used a KBr beam splitter. The IR beam was adjusted for grazing incidence (85°) external reflection on the crystal. A 6 mm aperture near the source was used to reduce the beam diameter to ≈ 7.2 mm on the 10 mm crystal. A grid wire polarizer was used for polarization dependent experiments. The interferometer was evacuated by a roughing pump to ≈ 1 mbar, the sample compartment of the spectrometer was purged by air, which was dried in a pressure swing absorber (Zander KM-25).

Background and sample IR spectra were recorded without changing the alignment of the crystal. For organic substances, the crystal was first exposed to the adsorbate and then aligned in the spectrometer for the sample spectrum. The background spectrum was obtained after heating the crystal (>600 K) to remove adsorbates from the surface. For IR spectra of gaseous adsorbates, such as CO, the crystal was first aligned and a background spectrum was taken prior to exposing the sample to the adsorbate. The spectra were recorded using the OPUS software with a resolution of 4 cm^{-1} and averaged over ≈ 8000 scans (fixed measurement time 1 h).^[94]

An example for a background and a sample spectrum of benzaldehyde on rutile(110) is shown in figure 3.8. Within the OPUS software these spectra are referred to as "single channel spectra". The overall shape of the spectra is given by the sensitivity of the detector and the transmission of the used optical components, especially the KBr beam splitter and the CaF_2 -windows. Furthermore, the spectra show a broad OH signal between 3000 and 3500 cm^{-1} , C-H stretch modes around 2900 cm^{-1} and a weak signal due to CO_2 at 2400 cm^{-1} . The O-H signal is due to an ice layer, which has formed on the cooled MCT detector during the experiments. The C-H signals indicate hydrocarbon contamination, possibly due to oil diffusion from the roughing pump into the spectrometer. No rotation-vibration spectrum of water vapor around 1600 cm^{-1}

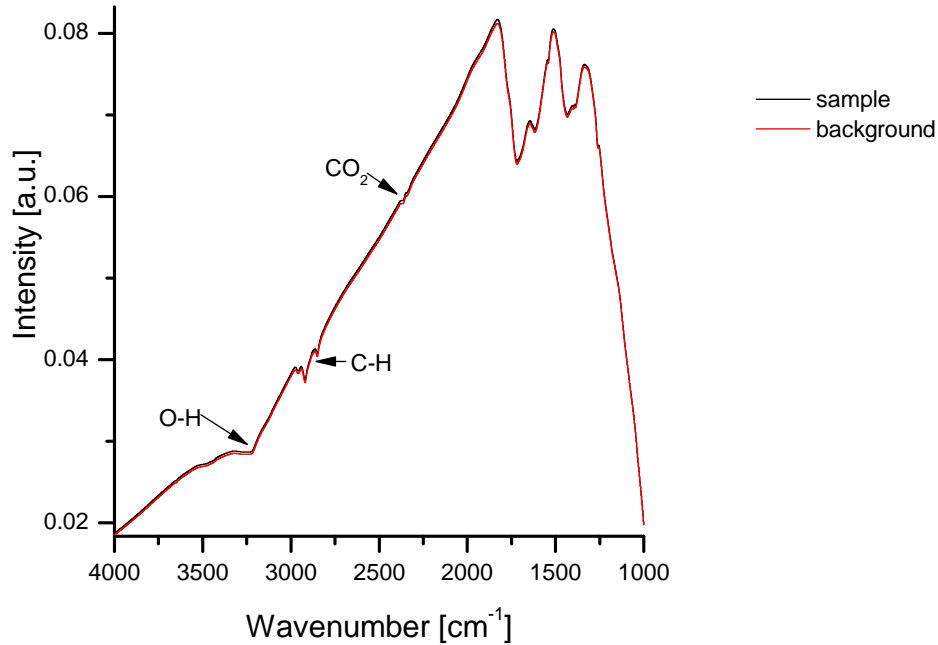


Figure 3.8: Single channel IR spectra: The spectra general shape is given by the sensitivity of the detector and transmission of the optical components. Furthermore, the spectra show O-H modes (3000-3500 cm^{-1}), C-H modes (2900 cm^{-1}) and CO_2 (2400 cm^{-1}).

is observed. The absence of these signals indicates that the spectrometer was evacuated and the pressure swing adsorber worked properly.

As the changes in absorption are typically too small to be recognizable from the single channel spectra, the absorbance spectrum $A(\tilde{\nu})$ is used in the discussion in the following chapters. It was obtained according to equation 3.4, where $I(\tilde{\nu})$ refers to the intensity of the sample or background single channel spectrum.

$$A(\tilde{\nu}) = -\log \frac{I_{\text{sample}}(\tilde{\nu})}{I_{\text{background}}(\tilde{\nu})} \quad (3.4)$$

One issue with the long measuring time used in the experiments herein was a drift in the single channel spectra over time. This drift was due to long term instabilities in the temperature, humidity and sample alignment. For example, the liquid nitrogen reservoir expanded as the liquid nitrogen slowly evaporated. Thus, the crystals alignment slightly shifted over time. Due to this drift, the absorbance spectra show a curly baseline, which was compensated by manually adapting a polynomial baseline to the spectrum, as indicated in figure 3.9.

The drift of the single channel spectra can lead to artifact signals in the absorbance spectra. Figure 3.10 shows a magnification of the single channel spectra from figure 3.8 and the corrected absorbance spectrum. The signal in the absorbance spectrum at 1540 cm^{-1} coincides with a bump, which is

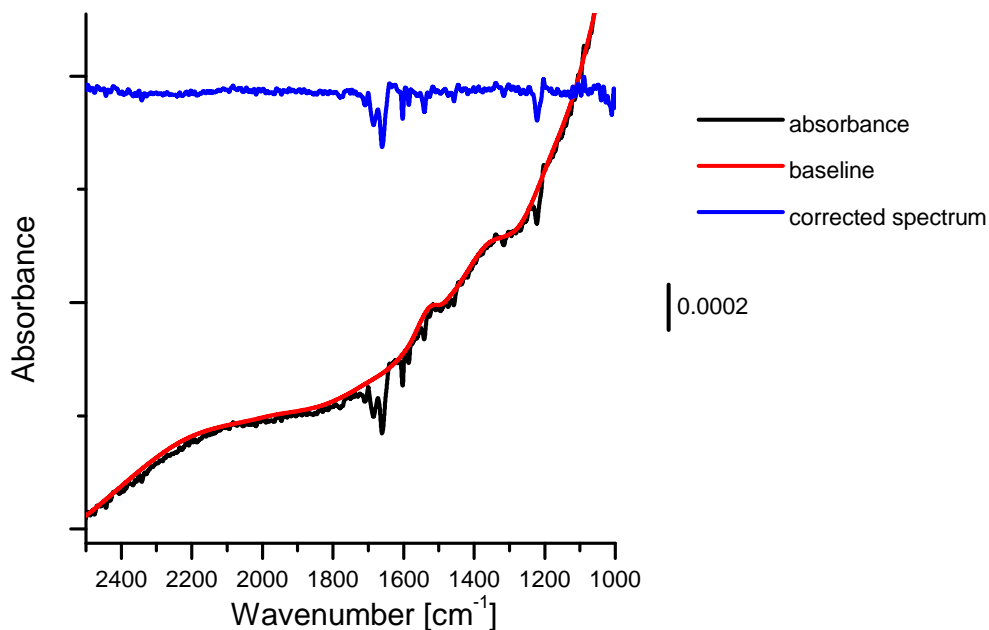


Figure 3.9: Absorbance spectrum before and after baseline subtraction. Due to a drift in single channel spectra, the absorbance spectrum shows a curly baseline. A manually fitted baseline is subtracted to obtain the "straightened corrected" spectrum.

observed in both sample and background single channel spectra. Therefore, this signal is presumably due to a slight drift in the single channel spectrum and not due to an adsorbate vibrational mode. Similar artifact signals were observed for the C-H modes, which are observed in the single channel spectra at 2900 cm^{-1} (figure 3.8).

Another problem leading to artifact signals is the alignment of the IR beam. As the IR beam is invisible, it is difficult to determine whether it is correctly aligned on the crystal surface, or whether it also covers parts of the sample holder. The alignment was done, based on the reflection of the helium neon laser. This laser is coupled into the interferometer to determine the position of the movable mirror and propagates co-linearly to the IR beam.^[44] However, as the IR beam is divergent and thus has a much larger spot diameter compared to the laser, this method of alignment is just a rough estimate.

An example for a signal, which is most likely due to poor alignment of the IR beam is given in figure 3.11. Two absorbance spectra of benzaldehyde are presented, which were recorded with different aperture sizes. Closing the aperture confines the IR beam on the crystal, and thus covers less parts of the sample holder than the unconfined beam. The 1705 cm^{-1} signal is only observed using the 6 mm aperture, but not the 3 mm aperture. Therefore, it is presumably due to adsorption of benzaldehyde on the sample holder and not

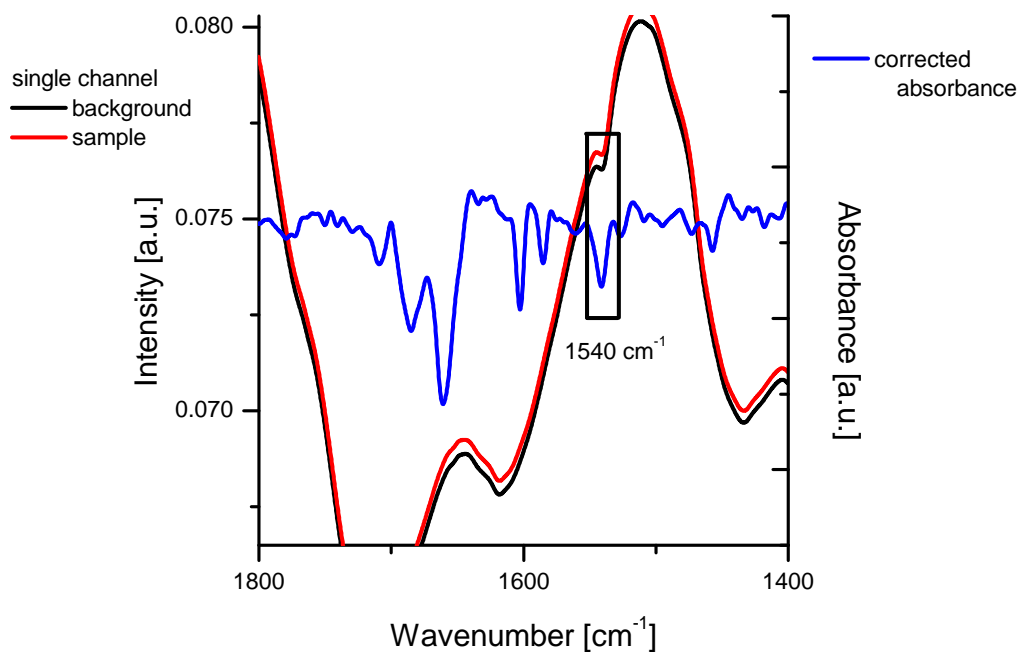


Figure 3.10: Artifact signal observed due to drift: The signal observed in the absorbance spectrum at 1540 cm^{-1} coincides with a signal observed in both background and sample spectra. Therefore, it is most likely an artifact due to a drift in these single channel spectra.

the crystal. Unfortunately, closing the aperture decreases the signal intensity and ultimately the signal to noise ratio. Therefore, spectra were recorded with a 6 mm aperture, but the likelihood of such artifacts were reduced by aligning the sample position with a confined IR beam using the 3 mm aperture. Using this method for alignment, the 1705 cm^{-1} signal was not observed anymore.

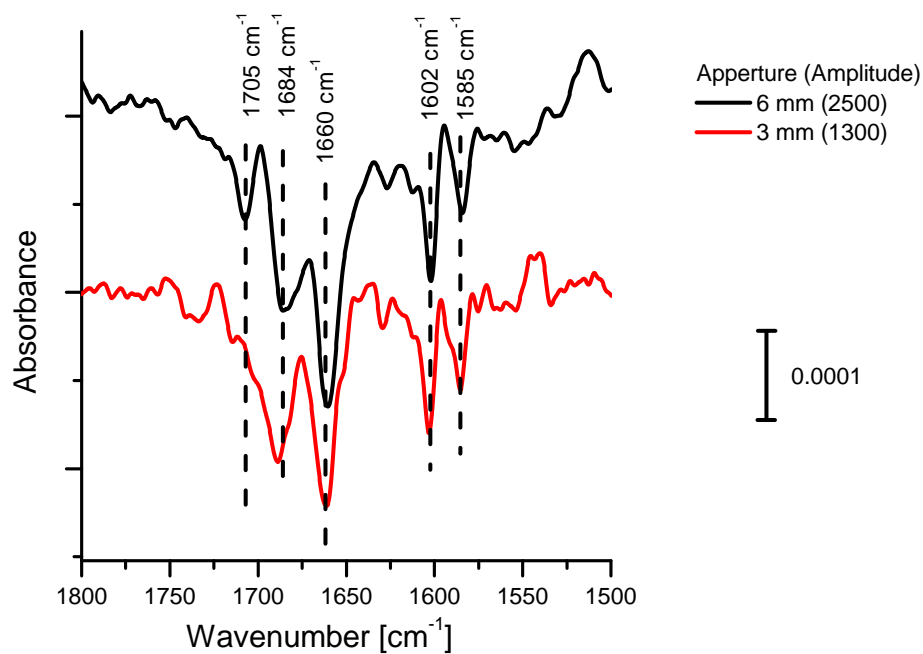


Figure 3.11: Artifact signal from adsorbate on sample holder: The IR spectrum of benzaldehyde recorded with a larger aperture size shows an extra signal at 1705 cm^{-1} , which is not observed in the spectrum recorded with the smaller aperture. This signal is possibly due to adsorbate adsorbed on a part of the sample holder.

4 Literature review titania

As mentioned in the introduction, titania is the prototypical transition metal oxide in surface chemistry. It is a promising candidate for many applications which has stimulated numerous studies of reactions of various adsorbates on this surface. This chapter gives an introduction to the surface structure and chemistry of rutile titania with a focus on defects and the surface chemistry of oxygen. For a complete introduction to the surface chemistry of titania see the review articles by Diebold,^[15,95] Pang et al.^[16], Henderson,^[96,97] Linsebigler et al.^[98] and Thompson et al.^[99]

4.1 The rutile(110) surface

Among the three modifications of titania: brookite, anatase and rutile, rutile is the thermodynamically most stable one. In bulk rutile, each titanium atom is coordinated by six oxygen atoms in a distorted octahedral geometry and each oxygen atom by three titanium atoms.^[101] The rutile unit cell is tetragonal with $a = b = 4.59 \text{ \AA}$ and $c = 2.96 \text{ \AA}$.^[90] Anatase has a lower surface energy than rutile.^[15] Therefore, thin films and (nano) particles (at lower temperatures) often consist of anatase. Most commercial catalysts, such as TiO₂ P25, are mixtures of rutile and anatase particles. High quality anatase single crystals for UHV studies are rare and tend to accidentally transform to rutile during annealing^[102].

This work focuses on the rutile(110) surface, which forms a [1x1] surface reconstruction, or a [2x1] reconstruction for more reduced crystals. The [1x1] reconstruction of the rutile(110) (figure 4.1) surface was studied using low energy electron diffraction (LEED) and scanning tunneling microscopy (STM).^[15,89,103] It consists of alternating rows of five coordinated titanium atoms (Ti_{5c}) and two fold coordinated bridging oxygen atoms (O_{br}).^[15] These rows are parallel to the <001> direction. Additionally, there are three fold coordinated in plane oxygen atoms, which surround the Ti_{5c} atoms, and six fold coordinated Ti atoms below the O_{br} atoms.

On an overannealed sample, Møller et al.^[89] have observed a [2x1] reconstruction using LEED. They proposed a missing row model which is derived from

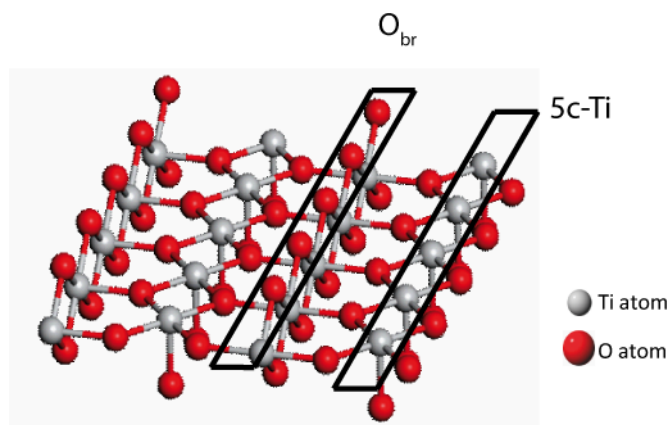


Figure 4.1: The rutile titania (110) 1x1 reconstructed surface consists of alternating rows of five coordinated titanium atoms (Ti_{5c}) and bridging oxygen atoms (O_{br}).^[100]

the [1x1] reconstruction by removing every second O_{br} row. However, this model was found to be incompatible with later STM results. Onishi and Iwasawa^[104] proposed a model of added Ti_2O_3 rows on the surface, which was later confirmed by quantitative LEED experiments.^[105]

Usually, STM images found in the literature are dominated by the electronic structure of the surface (figure 4.3). The images are recorded at tip bias that induces the tunneling of electrons from the tip to the unoccupied 3d orbitals of the titanium atoms. As the density of states is higher at the Ti_{5c} rows than at the O_{br} rows, the Ti_{5c} atoms are imaged as bright rows and the O_{br} atoms as dark rows.^[103] Non contact atomic force microscopy images the geometric structure of the surface.^[106]

4.2 Defects

As pointed out in the introduction, titania is especially interesting because it is a reducible oxide. For example, cleaning titania crystals in UHV by argon ion bombardment and annealing reduces the crystal and introduces defects. The ion bombardment removes the lighter oxygen more easily from the surface than the heavier titanium atoms.^[90,107] Therefore, the surface is amorphous and strongly reduced after ion bombardment.^[88] The reduction by ion bombardment was confirmed by Idriss and Barteau^[108] who observed signals of Ti^{I} to Ti^{IV} in x-ray photo electron spectroscopy (XPS) for such a surface. Annealing above 700 K was found to reoxidize the surface.^[88] Henderson showed through static secondary ion mass spectrometry (SIMS) experiments with surfaces enriched by titanium and oxygen isotopes, that this reoxidation occurs by diffusion of excess titanium atoms as point defects into the bulk.^[88] The

reduction of the crystal introduces electronic defect states, which have been observed in XPS,^[109] electron loss spectroscopy (ELS),^[90] IR spectroscopy^[110,111] and two photon photo emission studies.^[112] Furthermore, the defects are color centers, which is indicated by a change of crystal color: With increasing defect density, the crystal turns from white over light to dark blue to dark black (see figure 5.6 on page 55).^[15,113]

Various kinds of defects, especially point defects such as bridging oxygen vacancies (BOV) and interstitial titanium atoms, play a prominent role in the surface chemistry of titania.^[114,115] They are recombination sites for charge carriers in photo chemistry^[99,116] and affect the conductivity of the crystal.^[117] Furthermore, BOV and interstitials play a central role as charge donors in the adsorption of oxygen which will be discussed in the following section 4.3. Other point defects such as in plane oxygen vacancies are energetically less favorable.^[118]

BOVs have been observed in STM images as bright protrusions on the O_{br} rows,^[103,119] or in non contact atomic force images as dark spots on the bright oxygen rows.^[106,120] Water^[121–124] and methanol^[125–127] have been reported to dissociate in BOVs which results in hydroxyl and methoxyl groups at an O_{br} site. However, for water this dissociation in the BOVs was found to be reversible and does not quench a defect state which is observed in EELS spectra.^[128] In contrast, molecular oxygen has been observed to heal the vacancy and leaves an oxygen adatom on a Ti_{5c} atom upon dissociation.^[129]

Interstitial titanium atoms (from here on called interstitials) are formed during reoxidation of a reduced surface by diffusion of excess titanium atoms into the bulk.^[88] They have been found to be involved in the growth of new titania layers upon oxidation of the crystal and growth of the $[2 \times 1]$ reconstruction.^[113,130–135] Excess titanium atoms were reported to encapsulate adsorbed metal particles forming thin TiO_x layers. The growth of these layers, which is known as the strong metal support interaction (SMSI) effect, was reported to change the reactivity of the particles.^[13,136] Interstitials have also been proposed to be involved in redox reactions such as the reductive coupling of aldehydes,^[28,137–139] which will be discussed in the following chapter, and the reduction of formate on a cross linked $[2 \times 1]$ surface.^[140] The influence of interstitials has been found to be difficult to study systematically as preparation of different defect concentrations is laborious. Li et al.^[131] showed that the reduction affects the reoxidation mechanism of the crystals upon exposure to oxygen. They used ex situ quantification of the defects by electron paramagnetic resonance spectroscopy (EPR). Bennett et al.^[141] and Nolan et al.^[109] have proposed to use self doped titania thin films and crystals as model sys-

tems to study this effect. They prepared these systems by depositing titanium on top of the surface and annealed it subsequently.

Besides point defects, shear plane and terrace step sites were observed: Aono and Hasiguti^[142] have found by using EPR, that for defect concentrations TiO_{2-x} for $x > 4 \cdot 10^{-4}$ interstitials form pairs and $\{121\}$ plane defects. Furthermore, shear planes have been observed on highly reduced samples in STM.^[141] Martinez et al.^[143] found that step edges react similar to BOVs and are active sites for water dissociation or methanol adsorption. However, the adsorbates were found to bind more weakly to these sites compared to adsorption at BOVs.^[143]

The electronic structure of defects has been studied using density functional theory (DFT). The calculations on the influence of BOVs and interstitials have indicated a charge transfer from the defect sites to neighboring titanium atoms^[115,144–147] and a displacement of lattice atoms^[130,148]. Deskins et al.^[144] found that the charge from BOVs is donated to neighboring six coordinated Ti atoms. They proposed that near surface atoms better compensate the extra charge, as the crystal structure relaxes more easily than for bulk atoms. Thus, the charge would presumably accumulate near the surface. Finazzi et al.^[145] found that interstitials donate their charge to nearest neighbors as well. Haubrich et al.^[148] and Wendt et al.^[130] suggested that a sub surface interstitial pushes a surface Ti_{5c} atom outwards. This exposed atom interacts more strongly with adsorbates.

4.3 Surface chemistry of oxygen

The adsorption and reaction of oxygen on rutile(110) is complex and involves various reaction pathways, which have been found to depend on the defect density and the adsorption temperature. On reduced titania oxygen was found to adsorb molecularly at temperatures below 200 K, or dissociatively on Ti_{5c} atoms or in BOVs (figure 4.2). Adsorption in BOV was observed to heal the defect and leave a single oxygen adatom (O_{ad}), whereas dissociation at Ti_{5c} leaves pairs of O_{ad} at the surface.^[129,149] These dissociation mechanisms were observed in STM experiments, which are illustrated in figure 4.3.^[129] Furthermore, oxygen was observed to react with interstitials to form new TiO_x islands on (110) terraces. These oxygen species show a different chemical behavior which is discussed in chapter 6.

Molecular oxygen was reported to adsorb on the reduced surface and to be stabilized by charge transfer from defects. Henderson has found a molecular oxygen species which desorbs at 410 K in TPD.^[149] No isotope mixing has

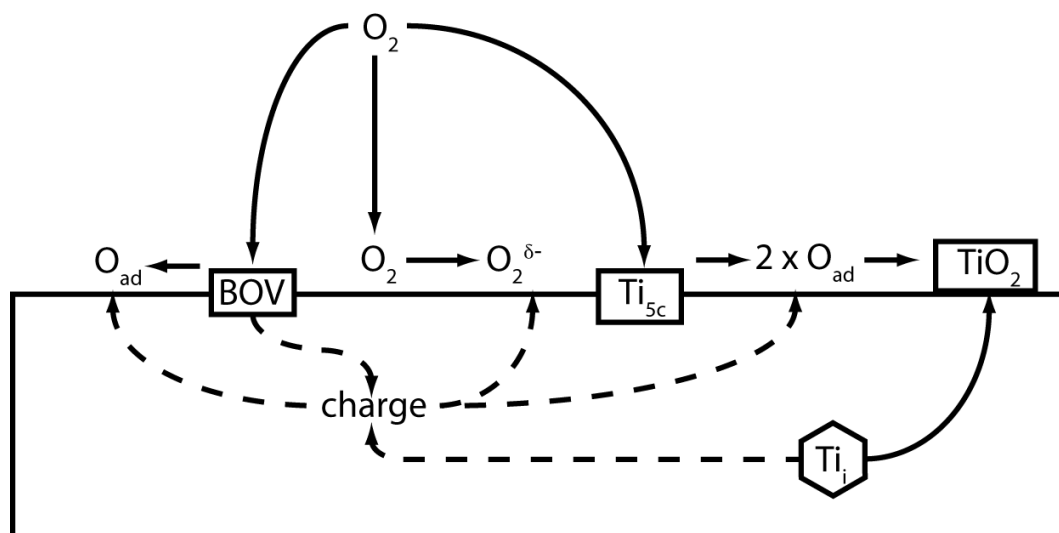


Figure 4.2: Schematic overview reactions of oxygen on rutile titania(110) - oxygen adsorbs both molecularly and dissociatively on reduced titania. Dissociative adsorption occurs at BOVs healing the vacancy and leaving an oxygen adatom, or at Ti_{5c} sites leaving two adatoms. Furthermore oxygen reacts with interstitials to form new islands.

been observed which indicated that this species adsorbs as molecular oxygen and does not evolve upon recombination of O_{ad} . This species has been proposed to form on the surface from a precursor species below 200 K: No TPD signal was observed when oxygen had been adsorbed at a higher temperature. The formation of the molecular species was found to require charge from defects, which is consumed in a parallel reaction: In a second TPD experiment after oxygen desorption without heating the crystal to restore the defects, the 410 K species has not been observed. The role of defects has been confirmed in EELS spectra: a Ti^{3+} signal which had been associated with a defect state was observed to disappear upon adsorption of oxygen and a new signal which indicated a O_2^- species appeared. Henderson proposed that the defects involved are BOVs: three oxygen molecules adsorbed per BOV, two desorbed at 410 K and one healed the vacancy.^[149] The charge transfer to molecular oxygen has been confirmed by EPR spectroscopy: EPR spectra of oxygen adsorbed on polycrystalline titania propose the existence of a superoxide species O_2^- , which is stable up to 400 K.^[150,151] Recently, Henderson proposed based on EELS spectra that a peroxo (O_2^{2-}) species forms upon adsorption of oxygen on the surface.^[152]

The low temperature molecular oxygen species has also been observed in photo and electron stimulated desorption experiments (PSD and ESD).^[153-156] Lu et al.^[153,154] have observed a slowly desorbing α oxygen species in PSD experiments which transforms upon heating to 250 K to a faster desorbing β species.

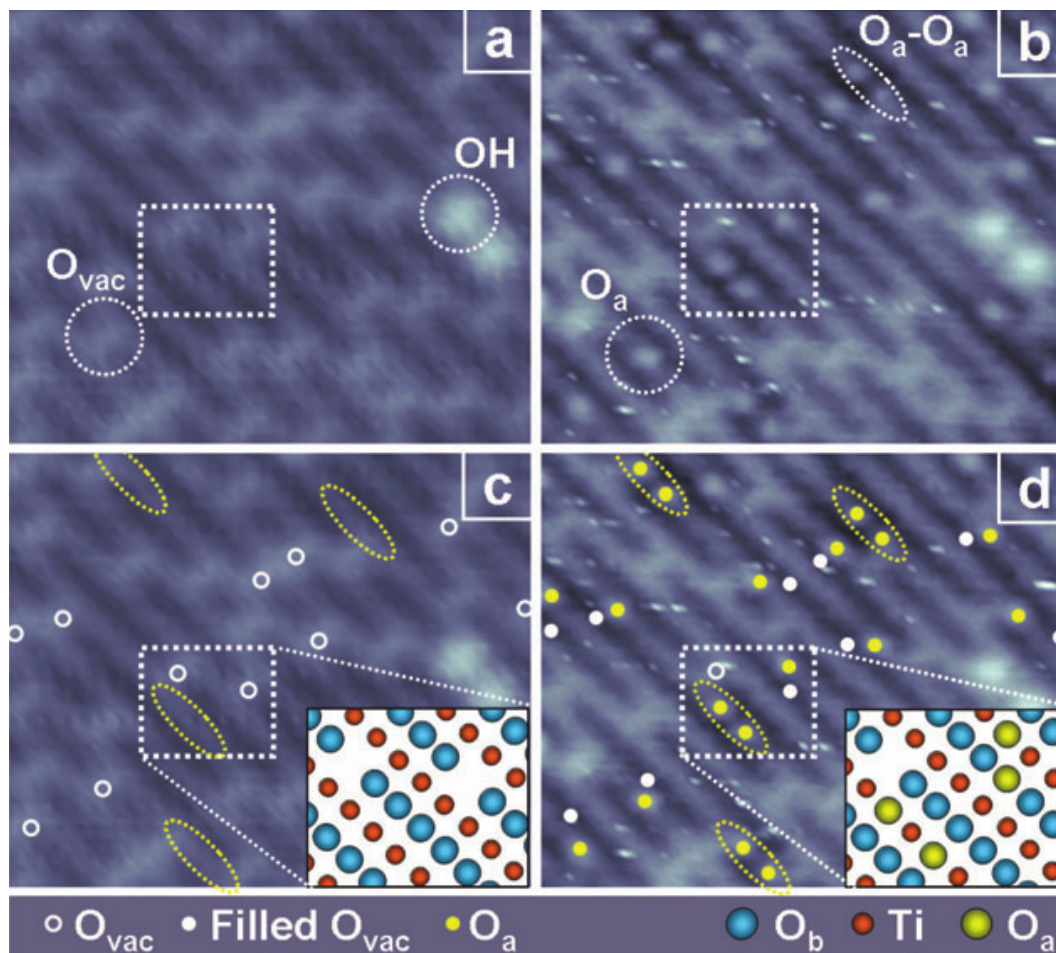


Figure 4.3: STM images of oxygen dissociation.^[129] Figures a and b show a vacuum annealed rutile(110) surface. The bright rows indicate the Ti_{5c} rows, whereas the dark rows are due to the O_{br} rows. The bright protrusion on the dark rows were identified as BOVs, (labeled O_{vac}) part of which are filled by dissociative adsorption of water. Figures b and d show the same area of the surface after exposure to oxygen at 300 K. Oxygen was dissociated in some BOVs, which is indicated by the disappearance of a BOV with a bright protrusion on a Ti_{5c} row nearby. Furthermore, oxygen dissociation to pairs of O_{ad} adsorbed at Ti_{5c} is observed. Figures c and d have additional markings to illustrate the effects. Reproduced from Ref.^[129] with permission from the PCCP Owner Societies.

The α species was found to be active for CO photo oxidation whereas the β species is inert. Later results by Rusu et al.^[155] have indicated two low temperature species α_1 and α_2 which coexist on the surface but show different photo desorption cross sections. The two species were attributed to adsorption at different defect sites. ESD experiments have confirmed the thermal conversion of the adsorbed oxygen: an oxygen species which is formed upon heating desorbs more slowly in ESD spectra than oxygen adsorbed at low temperatures.^[156]

The adsorption of molecular oxygen was further studied by Hartree Fock (HF) and DFT calculations.^[157,158] HF calculations on a cluster model have suggested a charge transfer from defects to the oxygen molecule. Based on the oxygen coverage, the calculations have indicated that oxygen adsorbs as a peroxo O_2^{2-} , a superoxo O_2^- or a neutral O_2 species at BOV and Ti_{5c} sites.^[157] DFT calculations further suggested an oxygen tetramere which binds to a BOV and a neighboring Ti_{5c} .^[158] In a combined STM and DFT paper, Tan et al.^[159] have suggested that oxygen adsorbs in a side on η_2 geometry at BOVs, which leans to a neighboring Ti_{5c} before dissociation.

Though it is generally accepted that oxygen is stabilized by charge transfer, it is under dispute whether interstitials or BOVs donate this charge.^[151,160] Oxygen was found to dissociate in BOVs which heals the vacancies and leaves oxygen adatoms. However, only half of the BOVs were filled upon dissociation.^[119,129,130,161,162] Du et al.^[129] concluded that dissociation of oxygen requires charge from more than one BOV per molecule, instead Wendt et al.^[130] proposed, that actually interstitials donate the necessary charge:

The influence of BOVs and interstitials was studied by comparing surfaces with different BOV densities.^[163–165] Petrik et al.^[163] prepared a "stoichiometric" surface: they first adsorbed water, which dissociated at the BOV sites, and removed the resulting surface hydroxyl groups in a reaction with oxygen. They compared the oxygen uptake of this surface with a defective annealed surface and strongly defective surfaces, which they had created by bombardment with electrons. The oxygen capacity of the sample has been observed to increase with defect densities: the stoichiometric surface showed almost no oxygen uptake whereas the bombarded surface showed a much higher capacitance than the annealed surface. Yim et al.^[164] studied the effect of electron bombardment and oxygen exposure on the surface band gap state corresponding to O(2p) and Ti(3d) in UPS. Oxygen exposure was found to quench the state whereas electron bombardment produced more defects. Therefore, Yim et al. concluded that BOV are responsible for the band gap state.

Wendt et al.^[130] first suggested, that interstitials are involved in the adsorption

of oxygen based on STM and PES. They observed that the defect state is neither quenched by healing vacancies through dissociation of water nor on an almost stoichiometric surface prepared by a method which is similar to the one used by Petrik et al. Based on the oxygen dissociation channel on Ti_{5c} atoms and the formation of TiO_x islands they proposed that near surface interstitials are the involved charge donors. Lira et al.^[165] showed that molecular oxygen desorption at 410 K only scales with BOV density for low densities but declines at higher densities. This observation is inconsistent with the model of oxygen adsorbing only at BOV sites. They concluded that the amount of molecular oxygen increases, as the amount of stabilizing charge available from interstitials increases with defect density, but at higher defect densities the dissociative adsorption becomes more pronounced and consumes the oxygen. Recently, the role of step edges on the adsorption of oxygen has been studied.^[166] Though step edges are reduced and show a similar reactivity to alcohols like BOV, less molecular oxygen desorption in TPD spectra was observed from misscut crystals with high step edges density.^[166,167] Furthermore, fewer TiO_x islands were observed in STM after an oxygen TPD, during which the crystal was heated to 500 K. In agreement with observations by Stone et al.^[133], this suggests, that step sites are highly active for dissociative adsorption of oxygen. In contrast to the effect on adsorption of oxygen, the role of interstitials in re-oxidising the crystal is well established.^[113,131,133,168-170] The mechanism has been reported to involve diffusion of interstitials to the surface and reaction with oxygen from the gas phase. Depending on the bulk defect density and temperature, different types of intermediate sub oxide structures have been observed such as the above mentioned $[2 \times 1]$ reconstruction, a similar cross linked added row structure^[133,168] and a rosetta structure.^[113] Regular $[1 \times 1]$ terraces were reported to grow at step edges^[133]. The variety of the different observed structures indicate that preparation of stoichiometric defect free surfaces is challenging. Simply annealing a crystal in oxygen, which is often used in the literature, has been found to result in an undefined surface.^[113]

5 Reductive coupling of benzaldehyde

In this chapter the reaction mechanism for the reductive coupling of benzaldehyde to stilbene is studied. Previous temperature programmed reaction spectroscopy (TPRS), scanning tunneling microscopy (STM) and density functional theory (DFT) results have suggested a reaction mechanism which is mediated by interstitials.^[28,138,139] A stilbene diolate intermediate was proposed (figure 5.1), but not experimentally confirmed. In this chapter, experimental evidence will be given for an intermediate stilbene diolate using infrared (IR) spectroscopy including studies on the influence of interstitial defects on its formation and reaction. The concentration of the intermediate scales with the bulk defect density which demonstrates the importance of bulk defects in surface science. The results in this chapter were published in *Chemistry - A European Journal*.^[171]

5.1 Surface chemistry of carbonyl components

Several reactions such as low temperature oxidation, solar fuel generation or photo oxidation of organic components involve oxygenates such as aldehydes, ketones or alcohols as intermediates. Therefore, the surface chemistry of oxygenates, especially of aldehydes and ketones, is of general interest for applications in heterogeneous catalysis and photo catalysis. To name one example, gold nano particles supported on titania show a high reactivity for low temperature oxidation^[18] and acetone and acetaldehyde oxidation are used as benchmark reactions to evaluate the efficiency of new photo catalysts.^[97,172,173] This chapter focuses on the reductive coupling of benzaldehyde, which is an excellent simple model reaction for carbonyl chemistry as it shows no side reactions on rutile(110).^[138]

Reductive coupling of aldehydes and ketones in solution is known as McMurry reaction^[174-177] and uses TiCl_3 and Zn powder as reductive agents. A two step mechanism was proposed: the first step is a pinacol coupling reaction to the 1,2-diolate. Electron transfer from low-valent Ti yields radicals, which

dimerize forming the diolate. This intermediate was found in the reaction solution.^[174] The second step is the deoxygenation of the diolate which yields the olefine. This step was proposed to occur on Ti^0 particles.^[174] Of all transition metals, titania shows the highest reaction yield in deoxygenation.^[175]

Idriss et al.^[108,178-181] studied the reductive coupling of benzaldehyde and acetaldehyde on titania powders and sputtered, not annealed rutile(001) crystals. They found that the reaction occurs on the freshly sputtered and therefore presumably amorphous surface.^[88] Annealing the crystal reoxidizes the surface, which in turn reduces the reaction yield. X-ray photo electron (XPS) spectra of the sputtered surface show Ti^{I} to Ti^{IV} signals but no Ti^0 .^[108] Thus, in contrast to the proposed mechanism for the McMurry reaction in solution, no Ti^0 is needed for the coupling on titania(001). Near edge X-ray absorption fine structure (NEXAFS) spectra support stilbene diolate as an intermediate for the coupling of benzaldehyde on the sputtered rutile(001) surface.^[182] Besides the coupling products, Idress et al.^[179] observed (1) mono-molecular reduction e.g. to toluene for benzaldehyde and ethanol in the case of acetaldehyde, (2) benzene and styrene which they attributed to a stilbene decomposition and (3) aldol condensation to crotonaldehyde for acetaldehyde. The coupling to stilbene is less favorable on powders than on single crystals compared to the side products. Ceria and ironoxide powders show similar reactions as the titania powder samples. The cross coupling product 1-phenyl-propene from coupling of benzaldehyde with acetaldehyde is observed as well.

On rutile(110) Qiu et al.^[183] suggested that formaldehyde polymerized on surfaces which had been annealed in oxygen. Furthermore, they observed a high temperature formaldehyde species and ethylene desorption on an ion bombarded surface. The polymerization product paraformaldehyde was identified from the $\nu(\text{C} - \text{O})$ signals in high resolution electron energy loss spectroscopy (HREELS). However based on DFT calculations, Haubrich et al.^[148] later suggested an η_2 - formaldehyde species which binds to Ti_{5c} and O_{Br} . This species is consistent with the CO signals, which were observed in HREELS as well.

5.2 Previous work

Previous work on the McMurry-like reductive coupling of benzaldehyde^[28,138,139] and acrolein^[137] on the vacuum annealed rutile(110) surface suggested an interstitial mediated reaction mechanism which involves a reaction intermediate. In the first step, benzaldehyde was proposed to adsorb on the surface and to be stabilized by an interstitial. Upon heating, two adsorbed benzaldehyde molecules couple to form a surface bound dimer, which is presumably a stil-

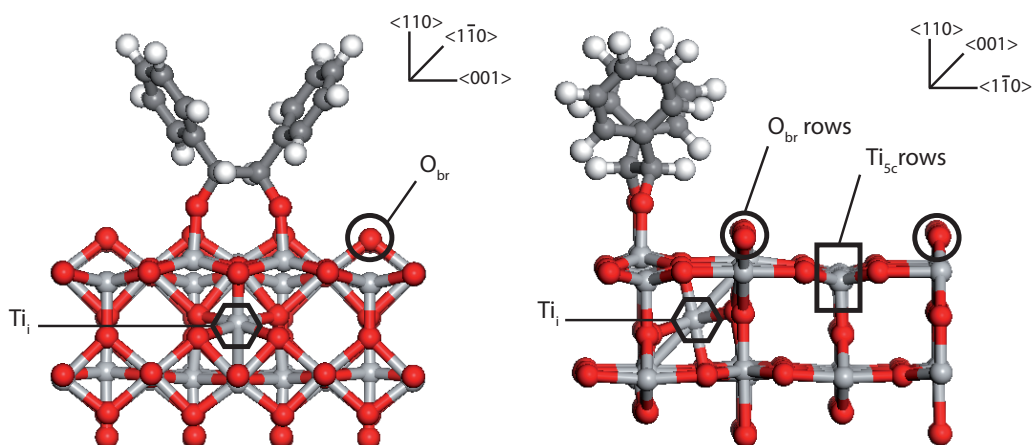


Figure 5.1: Stilbene diolate intermediate proposed by DFT calculations.^[100,171] The stilbene diolate binds to Ti_{5c} atoms and is stabilized by an interstitial. Upon heating the diolate is either reduced to stilbene leaving a new titania islands on the surface or dissociates and desorbs as benzaldehyde. Adapted with permission from L. Benz, J. Haubrich, S.C. Jensen, C.M. Friend, *ACS Nano*, **2011**, *5*, 834-843. Copyright 2011 American Chemical Society.

bene diolate. After further heating, the intermediate either falls apart and releases benzaldehyde, or reacts with the interstitial to the coupling product stilbene. The oxygen atoms of the carbonyl group remain on the surface forming new titania islands on the (110) terraces.

TPR spectra (figure 5.2)¹ show three desorption signals for benzaldehyde (m/z 106): a multilayer signal at 190 K, a molecular species, which shifts in desorption temperature from 380 K to 350 K and a high temperature species at 485 K.^[28] The molecular species has been assigned to adsorption on Ti_{5c} rows, the coverage depending temperature shift was suggested to indicate repulsive interaction between the adsorbed molecules. The high temperature signal coincides with desorption of stilbene (m/z 180) at 500 K. The common desorption temperature was proposed to indicate a common precursor state on the surface.^[28]

Bridging oxygen vacancies (BOV) were suggested not to be involved in the reductive coupling of benzaldehyde.^[28] If BOVs were the active site, water coadsorption would have quenched the reaction. Water is known to adsorb dissociatively in BOV and would compete with benzaldehyde for those sites, which was not observed in TPRS experiments with predosed water.^[28] In con-

¹The peak temperatures reported here are from reproducing the TPRS results in the vacuum chamber in Oldenburg. No calibration to the previously reported temperatures was done for a better comparison with the temperatures used in the later IR experiments. The errorbar of the temperatures given herein is ± 20 K.

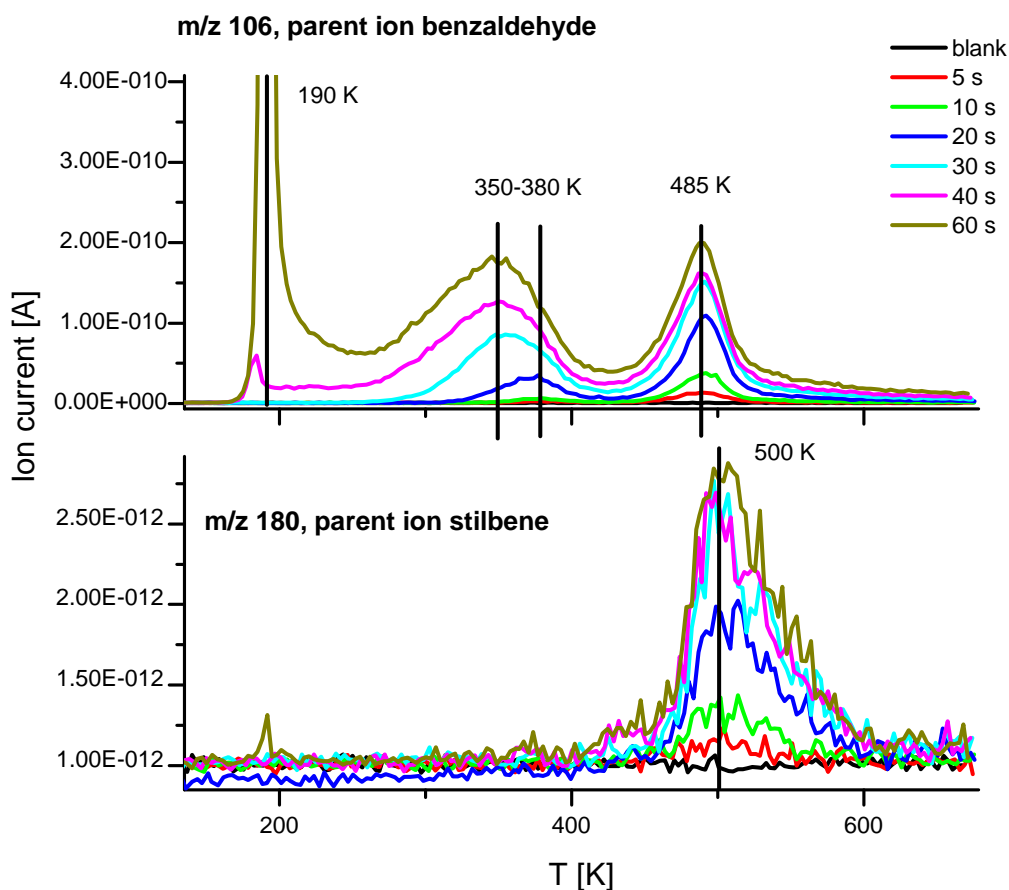


Figure 5.2: TPR spectra of benzaldehyde adsorbed on the vacuum annealed rutile(110) surface for increasing exposure. Three desorption signals are observed: a condensed multilayer signal at 190 K, a physisorbed species which shifts from 380 K to 350 K with increasing coverage and a high temperature species which desorbs at 485 K independantly of coverage. The high temperature species coincides with stilbene desorption at 500 K. No other reaction prodcuts were observed. These own spectra reproduce results from Benz et al.^[28] Benzaldehyde was exposed via a 20 μm pin hole at a pressure of 0.1 mbar (see section 3.5). The crystal was reduced by 50 preparation cycles.

5.3 Adsorption and reaction of benzaldehyde on reduced rutile(110)

trast, stilbene formation was observed in consecutive TPRS experiments without intermediate heating to restore the BOVs. This observation indicated that BOVs are not consumed in the reaction. Furthermore, no benzaldehyde adsorption in BOVs was observed in STM.^[138]

The involvement of interstitials has been strongly suggested by STM images, which have shown the growth of new islands on the terraces after desorption of stilbene, and the quenching of the reaction by oxygen.^[28] Wendt et al.^[130] observed similar islands after exposing a rutile(110) surface to oxygen and heating to 448 K. They concluded that these islands form by oxidation of interstitials which diffuse onto the surface. Dosing oxygen prior to benzaldehyde was observed to quench the high temperature benzaldehyde signal and the stilbene formation in TPRS. This observation suggested that oxygen competes with benzaldehyde for the charge donated by interstitials. Thus, without the interstitials charge no intermediate has been formed on the surface. The surface reactivity was restored in a consecutive TPRS experiment which suggested, that interstitials diffuse from the bulk to the surface.

STM studies (figure 5.3) visualized the pairing of benzaldehyde on the surface.^[138,139] After adsorption, benzaldehyde has been imaged as round features centered on the Ti_{5c} rows, which diffused across the surface at room temperature. After heating, new elongated features appeared along the rows which suggested the formation of dimers. In agreement with TPRS experiments, no dimers were observed when benzaldehyde was adsorbed after exposing the surface to oxygen. Exposing the dimers to oxygen was reported to induce desorption of benzaldehyde, which illustrated to competition of oxygen and benzaldehyde for the surface charge of interstitials.^[139]

5.3 Adsorption and reaction of benzaldehyde on reduced rutile(110)

In contrast to metal surfaces, IR spectra on dielectric surfaces give additional information on the orientation of the adsorbed dipoles. The surface selection rule for dielectric surfaces, which was derived in section 2.3, states that dipoles aligned parallel and perpendicular can be detected. Absorbance spectra recorded with p-polarized light show negative peaks for dipoles oriented perpendicular to the surface. Dipoles aligned parallel to the surface and parallel to the plane of incidence appear as positive peaks. Dipoles oriented parallel to the surface but perpendicular to the plane of incidence are observed as negative peaks in s-polarized spectra. The results presented herein were recorded

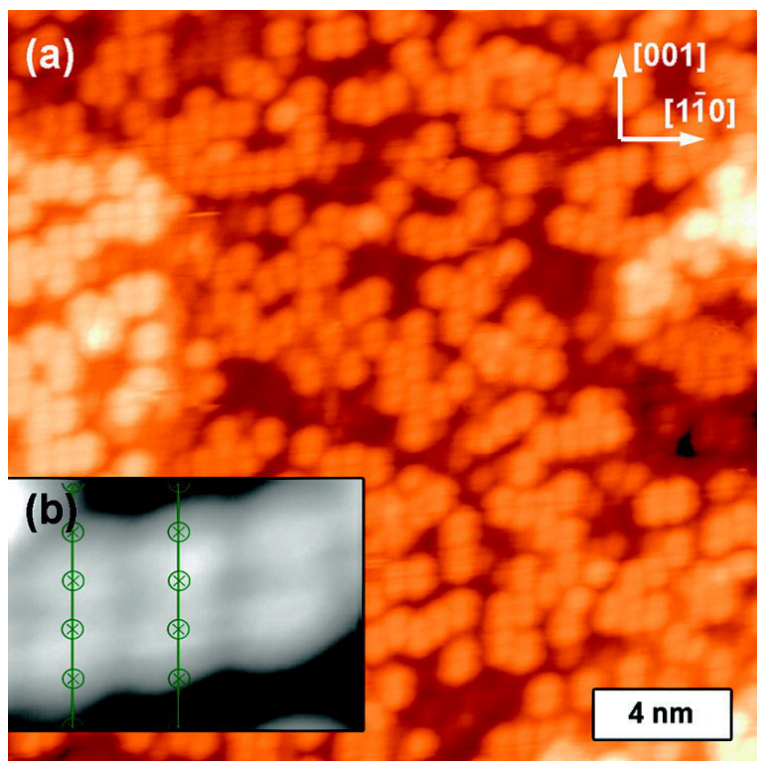


Figure 5.3: STM image indicating pairing of benzaldehyde: a) STM image of benzaldehyde adsorbed on $\text{TiO}_2(110)$, heated to ≈ 350 K and imaged at 50 K. b) Detail scan of paired features ($21 \text{ \AA} \times 14 \text{ \AA}$). The green markings suggest the position of Ti_{5c} . Adapted with permission from L.Benz, J. Haubrich, S.C. Jensen, C.M. Friend, *ACS Nano*, **2011**, *5*, 834-843. Copyright 2011 American Chemical Society.

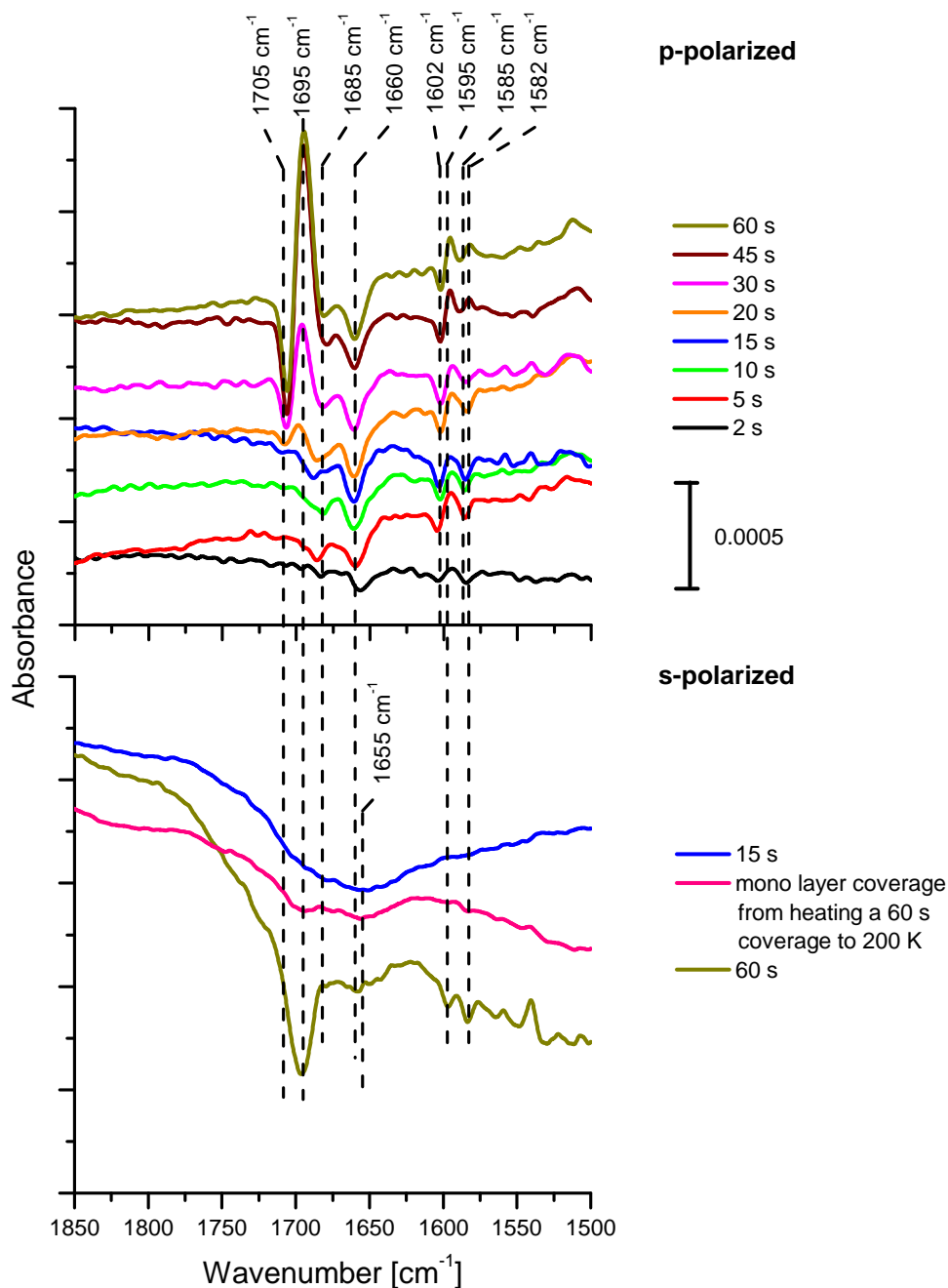


Figure 5.4: p- and s-polarized IR spectra of benzaldehyde adsorbed at 110 K show three carbonyl species: a multilayer signal at 1695 cm^{-1} , a physisorbed species at 1685 cm^{-1} and a species presumably adsorbed at defect sites at 1660 cm^{-1} . The 1705 cm^{-1} signal is most likely an artifact (see section 3.7). Benzaldehyde was exposed via a $20\text{ }\mu\text{m}$ pin hole at a pressure of 0.1 mbar (see section 3.5). The crystal was reduced by 60 preparation cycles.

with the plane of incidence parallel to the $\langle 001 \rangle$ direction which is parallel to the bridging oxygen rows on the surface.

IR spectra of benzaldehyde adsorbed at 110 K (figure 5.4) show three carbonyl (C=O) species: a multilayer signal at 1695 cm^{-1} , a physisorbed species at 1685 cm^{-1} and a species presumably adsorbed at defect sites at 1660 cm^{-1} (see table 5.1 for an overview of all signals). The multilayer signal appears at high coverages as positive signal in p-polarized spectra and a negative signal in s-polarized spectra. This observation indicates that the carbonyl group of this species is aligned parallel to the surface. Heating to the multilayer desorption temperature in TPRS (200 K) removes the signal. The two other species appear as negative signals in p-polarized spectra and a broad unresolved signal in s-polarized spectra, which indicates an alignment mostly perpendicular to the surface. The 1685 cm^{-1} species is barely shifted from the liquid phase spectra^[184] at 1703 cm^{-1} which indicates a weak binding to the surface. Therefore, this species is most likely due to physisorption at Ti_{5c} atoms as observed in STM images.^[138] Qiu et al^[183] observed a signal at 1694 cm^{-1} for physisorbed formaldehyde adsorbed on oxygen annealed rutile(110). The second benzaldehyde species at 1660 cm^{-1} is more strongly shifted which suggests adsorption at more strongly binding defect sites. Haubrich et al.^[148] predicted a stabilization effect for formaldehyde adsorption by a sub-surface interstitial. The calculated mode shifts from 1694 cm^{-1} for formaldehyde bound on Ti_{5c} on the stoichiometric surface to 1640 cm^{-1} for adsorption with a subsurface interstitial in a $\langle 110 \rangle$ channel, or 1658 cm^{-1} with an interstitial between two $\langle 110 \rangle$ channels. Henderson^[185] observed for acetone a shift of the carbonyl signal from 1690 cm^{-1} to 1660 cm^{-1} upon heating to 285 K. The adsorption at defect sites is probably hindered for acetone at high coverages by intermolecular repulsion, which is resolved by partly desorbing acetone at 285 K. At this temperature only a stabilized species remains on the surface in agreement with TPRS results.^[185]

The IR spectrum recorded after heating to 300 K (figure 5.5) provides further evidence for the assignment of the 1660 cm^{-1} species to adsorption at interstitial defect sites: the IR signal at 1685 cm^{-1} gets weaker after heating to 300 K which indicates that the more weakly bound species desorbs faster than the stabilized species, which remains on the surface. This observation suggests that the stabilized species is the one which is reduced to the dimer. As the involvement of interstitials has been established^[28,138] and will further be confirmed in the following section, this finding further supports assignment to the adsorption at interstitial defect sites.

Other possible explanations for the stabilized species include a resonance effect

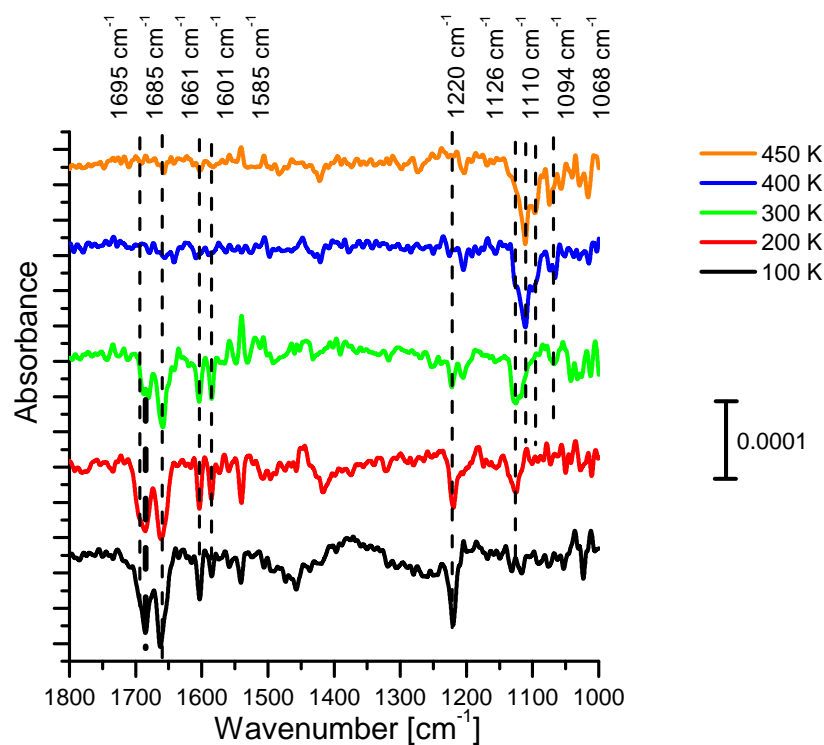


Figure 5.5: p-polarized IR spectra recorder after heating to increasing temperatures. The IR spectra were recorded after adsorption of a sub saturation coverage of benzaldehyde (see 20 s dosage in figures 5.2 and 5.4) and heating to the given temperatures. Upon heating to temperatures above 300 K, the benzaldehyde signals disappear and a new alkoxy signal around 1100 cm^{-1} appears. Signals observed for benzaldehyde are assigned to the carbonyl stretch modes at 1695, 1685 and 1661 cm^{-1} , the phenyl ring modes at 1601 and 1585 cm^{-1} and the C–C stretch modes between the phenyl ring and the carbonyl carbon atom at 1220 cm^{-1} (see table 5.1). The crystal was reduced by 65 preparation cycles.

in a physisorbed dimer or an intra molecular resonance effect. A similar signal at 1663 cm^{-1} is observed in liquid film spectra of benzaldehyde,^[184] but not in spectra of a diluted solution.^[186] The presence of the signal at higher concentrations suggests a hydrogen bridge bonded dimer, which is confirmed by DFT calculations for gas phase benzaldehyde.^[187] However, this dimer probably could not bind to the surface due to steric hindrance and is therefore discarded here. An intra molecular resonance effect involves the collective excitation of vibrational modes and is discarded based on the different desorption behavior (figure 5.5): at 300 K the physisorbed species is partly desorbed in contrast to the stabilized species. If the two signals were due to an intra molecular resonance effect both signals should disappear simultaneously.

Upon heating to temperatures above 300 K, the benzaldehyde signals disappear and new alkoxy signals at 1100 cm^{-1} appear (figure 5.5). These results are in agreement with the TPRS results (figure 5.2): At the onset of desorption of the physisorbed benzaldehyde species in TPRS at 300 K, the carbonyl signals begin to disappear. No carbonyl signal is observed at 400 K, even though benzaldehyde desorbs at 485 K in TPRS. Instead, new signals at 1100 cm^{-1} appear. These signals indicate an alkoxy species (C–O) based on similar signals at 1113 and 1153 cm^{-1} which are observed for adsorption of formaldehyde on rutile (110) in HREEL spectra.^[43,183] Qiu et al.^[183] attributed these signals to the polymerization product para-formaldehyde. The alkoxy signals of di-benzyl-ether in liquid films are observed at 1095 and 1072 cm^{-1} .^[184] In conclusion, the high temperature species observed in TPRS is chemically bound to the surface and the carbonyl group is reduced to an alkoxy group. Together with the previous STM results, these spectra provide strong evidence for the proposed stilbene diolate intermediate (figure 5.1).^[138]

Besides the carbonyl signals, IR spectra of benzaldehyde show signals of the phenyl ring at 1601 cm^{-1} and 1585 cm^{-1} and the C-phenyl stretch mode at 1220 cm^{-1} . The signals appear as negative signals in p-polarized spectra, indicating the phenyl ring stands mostly perpendicular to the surface in contrast to metal surfaces where it often lies flat.^[188] The wavenumbers are barely shifted compared to the reference spectra, which indicates a minor influence of adsorption. The phenyl ring modes in benzaldehyde show a relatively strong signal which suggests that the carbonyl group induces a strong dipol moment due to the conjugated π -electron system. For the stilbene diolate no phenyl signals are observed.

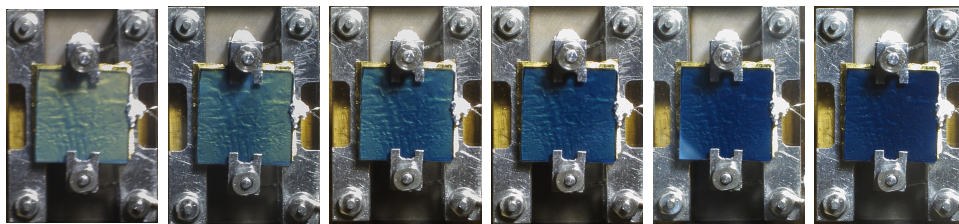


Figure 5.6: Photos of the used rutile(110) crystal after 10, 20, 30, 40, 50 and 60 cycles of argon bombardment and annealing at 600°C. The blue color indicates the presence of bulk defects.

Table 5.1: Overview of observed signals and references taken from the Spectral Database for Organic Compounds (SDBS) and National Institute of Standards and Technology (NIST).^[184,186] Formaldehyde and acetone are references from HREELS data, all data given in cm^{-1} .

	measured	SDBS ^{[184]1}	NIST ^{[186]2}	formaldehyde ^[183]	acetone ^[185]
carbonyl	1685, 1660	1703, 1664 ³	1708	1694	1690, 1660 ⁴
phenyl ring	1601, 1585	1597, 1584	1587, 1549	-	-
phenyl-C	1220	1204	1202	-	-
alkoxy	≈ 1100	1095, 1072 ⁵	-	1113, 1153 ⁶	-

¹ benzaldehyde liquid film

² benzaldehyde 2% solution

³ presumably a monomer and a dimer, see text

⁴ shifts to 1660 cm^{-1} after heating to 285 K^[185]

⁵ dibenzylether, liquid film

⁶ from para-formaldehyde after heating, ν_{asym} and ν_{sym}

5.4 Influence of bulk defect density

In order to further study the role of bulk defects and their influence on the reaction yield, experiments on a crystal with an increasing bulk reduction were conducted. A rutile(110) crystal was reduced by repeated cycles of ion bombardment at 1 kV at room temperature and tempering at 873 K (see section 3.3 for details). It is known that this preparation procedure introduces bulk defects (section 4.2). The density of these defects can be judged by the gradually darkening blue color (see figure 5.6). Special care was taken to prevent exposure to oxygen, e.g. no experiments with coadsorbed oxygen were conducted,

to prevent reoxidation of defects. Further quantification of the bulk defect density was not possible with the available methods: a titration of BOVs with water was not possible. This method relies on the ratio of a high temperature TPD signal from hydroxyl recombination from BOV sites to the total amount of water desorbing from the surface. In this case the recombination signal was covered up by the pump tail of the physisorbed water signal and could therefore not be quantified. Electron paramagnetic resonance (EPR) measurement to quantify the amount of Ti^{3+} was not possible as the crystal would have to be characterized ex-situ and cut to fit into the EPR test tube. Exposure of the crystal to oxygen would have falsified the results. Furthermore, a new crystal would have to be used for every reduction step which would involve issues with the reproducibility of the reduction procedure. Exposure to oxygen is an issue for XPS or STM experiments as well, as for these methods the sample needs to be transferred to another vacuum system. Furthermore, these methods, like the titration of BOVs with water, would only quantify the amount of (near) surface defects, which are presumably extremely prone to reoxidation upon oxygen exposure. For this work however, the density of bulk defects is more important.

p-polarized IR spectra of the carbonyl signal recorded after adsorption at 110 K for each reduction step show no measurable influence of the bulk defect density on adsorption. As one of the two signals is tentatively assigned to adsorption of benzaldehyde at defect sites, the intensity of this signal should increase compared to the physisorbed signal. Based on DFT calculations, Deskins et al.^[144] proposed that BOV would donate their charge to form Ti^{3+} defects on regular Ti sites. These defects have been found to be most stable at the first sub-surface layer. The crystal structure at the surface was proposed to be more flexible than in the bulk and therefore could compensate more easily for the perturbation by the defect. Though the model used by Deskins et al. only considers BOV as charge donors for the formation of the point defects, Finazzi et al.^[145] showed that interstitials additionally donate charge to neighboring Ti atoms. Based on the aforementioned assumption that one of the carbonyl signals is due to adsorption at defect sites, this would indicate, that the available defects at the surface saturate quickly during annealing, even after 10 preparation cycles. A light blue color after 10 preparation cycles confirms the presence of various kinds of defects as seen in the first image on the left in figure 5.6.

The lack of dependency between bulk reduction and absorbance of the carbonyl modes indicates that the optical properties, e.g. the dielectric constant, of the titania crystal do not change significantly in the IR wavelength range,

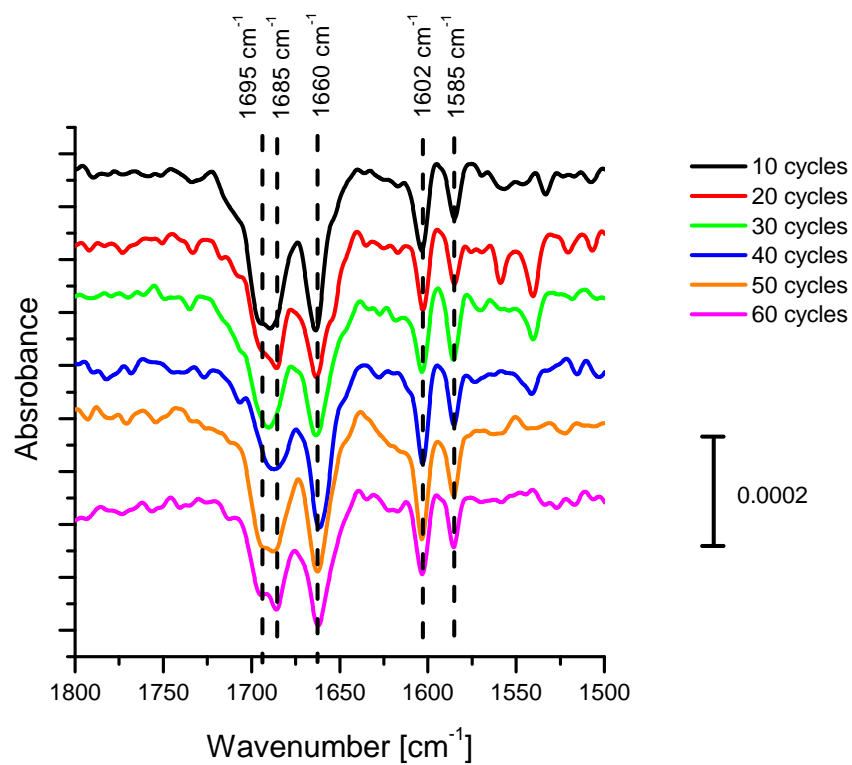


Figure 5.7: p-polarized IR spectra of a sub saturation coverage of benzaldehyde (see 20 s dosage in figures 5.2 and 5.4) adsorbed on a crystal with increasing bulk defect density shows no measurable effect on adsorption at 110 K.

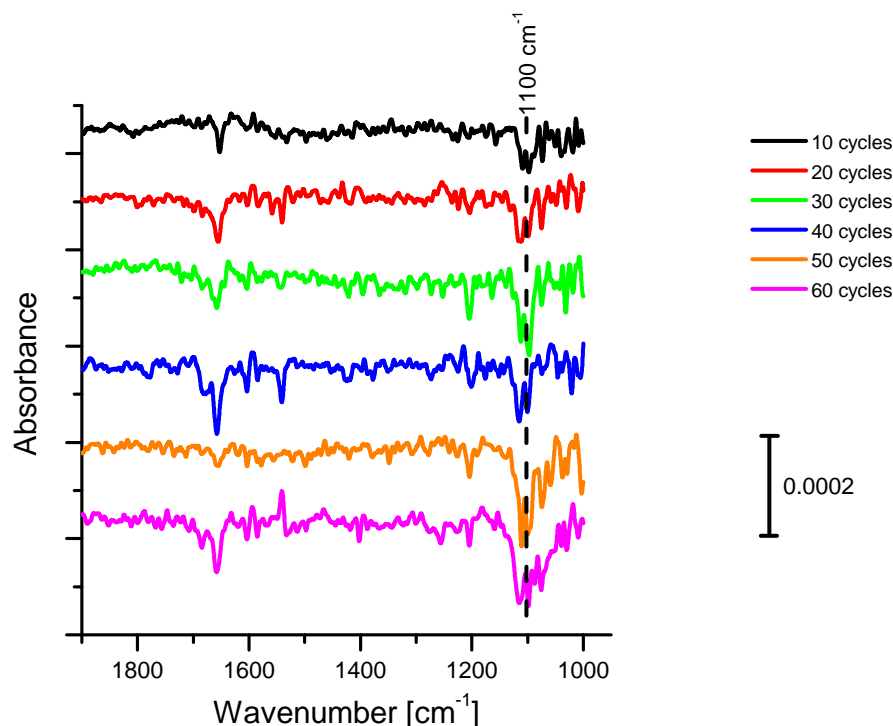


Figure 5.8: Influence of bulk defect density on intermediate formation - p-polarized IR spectra of a sub saturation coverage of benzaldehyde (see 20 s dosage in figures 5.2 and 5.4) adsorbed on a crystal with increasing bulk defect density recorded after heating to 400 K show an increase in the intensity of the alkoxy signal around 1100 cm^{-1} .

even though the blue color indicates an impact of bulk defects in the visible range. This observation refutes the interpretation for the observed switching between a positive and a negative signal in absorbance spectra of NO adsorption on oxidized and reduced titania by Xu et al.^[50] Their model to explain the observed sign reversal is incomplete as it does not consider the x and z components of the p-polarized electric field separately. Furthermore, they used crystals prepared by annealing in oxygen which, as discussed in section 4.3, creates an undefined rough surface. Such a surface has a high concentration of step edges which could shift the relative abundance of molecules adsorbed perpendicular to the surface at terrace sites to adsorption mostly parallel to the surface at kink sites.

The yield in stilbene and stilbene diolate intermediate scales with the bulk defect density (figure 5.8), which confirms the importance of bulk defects. The intensity of the alkoxy signal in IR spectra of benzaldehyde, which was heated to 400 K, increases with the number of preparation cycles (figure 5.8). Quantification of IR spectra in reflectance is unreliable. Although the absorbance is in principal proportional to the number of dipoles (see equation 2.13), small changes in alignment of the dipole with respect to the surface can severely

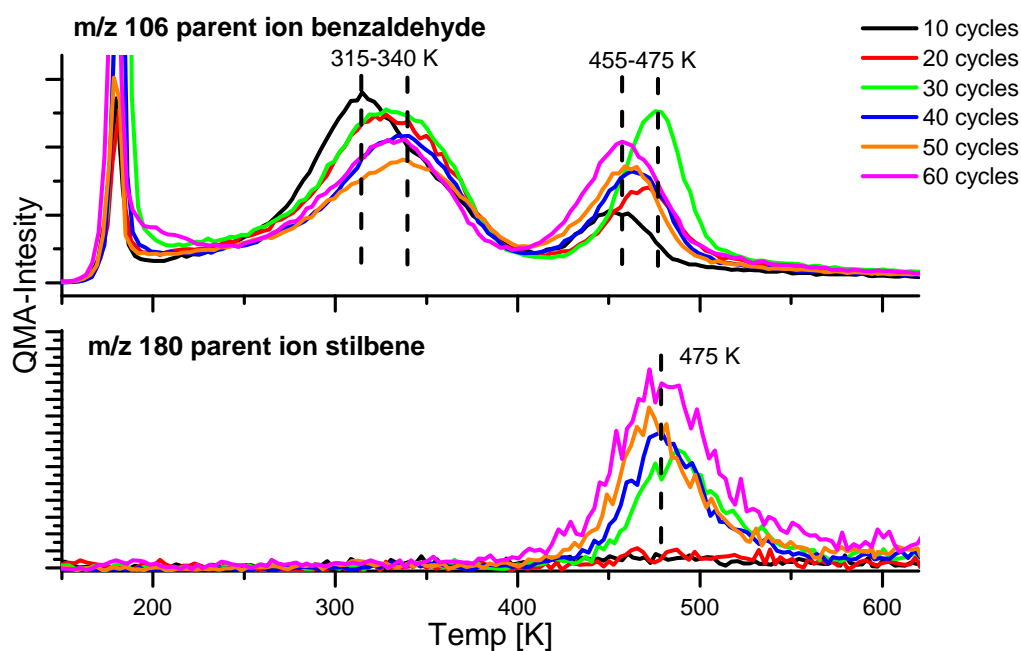


Figure 5.9: TPR spectra of a sub saturation coverage of benzaldehyde (see 20 s dosage in figures 5.2 and 5.4) adsorbed on a crystal with increasing bulk defect density. The stilbene signal scales with increasing bulk defect density. The high temperature benzaldehyde desorption signal peaks after about 30 preparation cycles.

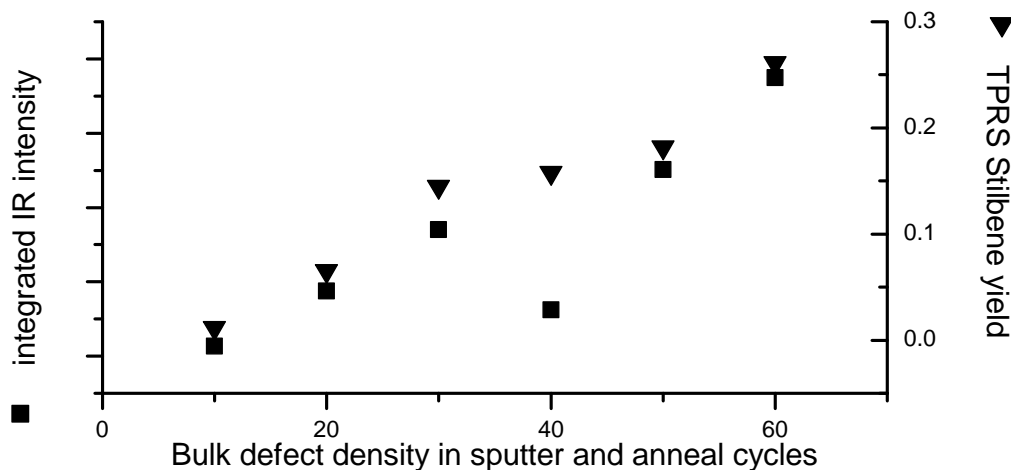


Figure 5.10: TPRS stilbene yield from figure 5.9 and integrated intensity of the alkoxy signal from figure 5.8 show that the stilbene yield and apparent concentration of the intermediate scale with the bulk defect density.

change the absorption cross section, which falsifies the result. Herein, TPRS results confirm the influence of the defect density (figure 5.9). The high-temperature benzaldehyde desorption signal increases with defect density; a maximum is observed after 30 cycles. In contrast, the stilbene desorption increases continuously. The IR spectra indicate that with increasing defect density, the amount of stilbene diolate that forms on the surface increases. Therefore, the yields in the high temperature benzaldehyde desorption and stilbene desorption in TPR spectra increase as well. The stilbene diolate either dissociatively desorbs as benzaldehyde or reacts to form stilbene. Both reaction channels compete with each other. At higher defect concentrations the reduction to stilbene benefits from additional charge and ultimately dominates the dissociative desorption pathway. This model explains the saturation of the benzaldehyde desorption. The common scaling of the stilbene diolate and the stilbene yield in TPRS further confirm that the diolate is a reaction intermediate and not a side product formed on the surface.

The quantification of the TPR spectra used in the previous paragraph relies on an estimated value for the ionization cross sections and uses the NIST fragmentation pattern as reference (see section 3.6).^[34] Despite the uncertainty about the absolute stilbene yield, the deviation is expected to be systematic. Therefore, this model is sufficiently precise to reproduce general trends. For the analysis, the integrated desorption signal of m/z 106 for benzaldehyde for temperatures above 250 K was compared to the integrated desorption signal of m/z 102 for stilbene. This mass fragment was used instead of the shown m/z 180 parent ion to minimize the influence of the mass dependent sensitivity of the quadrupole mass spectrometer. The signals were corrected for the ionization cross sections and the relative fragmentation probability calculated from NIST reference mass spectra.^[34]

5.5 Oxygen

In agreement with previous results, no stilbene is formed from reductive coupling from a surface covered with oxygen.^[28] In TPR spectra with preadsorbed oxygen (figure 5.11) neither stilbene nor the high temperature benzaldehyde signal are observed.^[28] This concurs with previous TPRS results and STM results which indicated that no dimer forms under such conditions.^[28,138,139] The oxidation of interstitials by coadsorbed oxygen is the faster reaction. Recent STM results showed that this reaction occurs at 180 K, whereas the reaction with benzaldehyde is neglectable below 300 K (figure 5.5).^[189] The low temperature benzaldehyde species signal is more intense than in the case of the

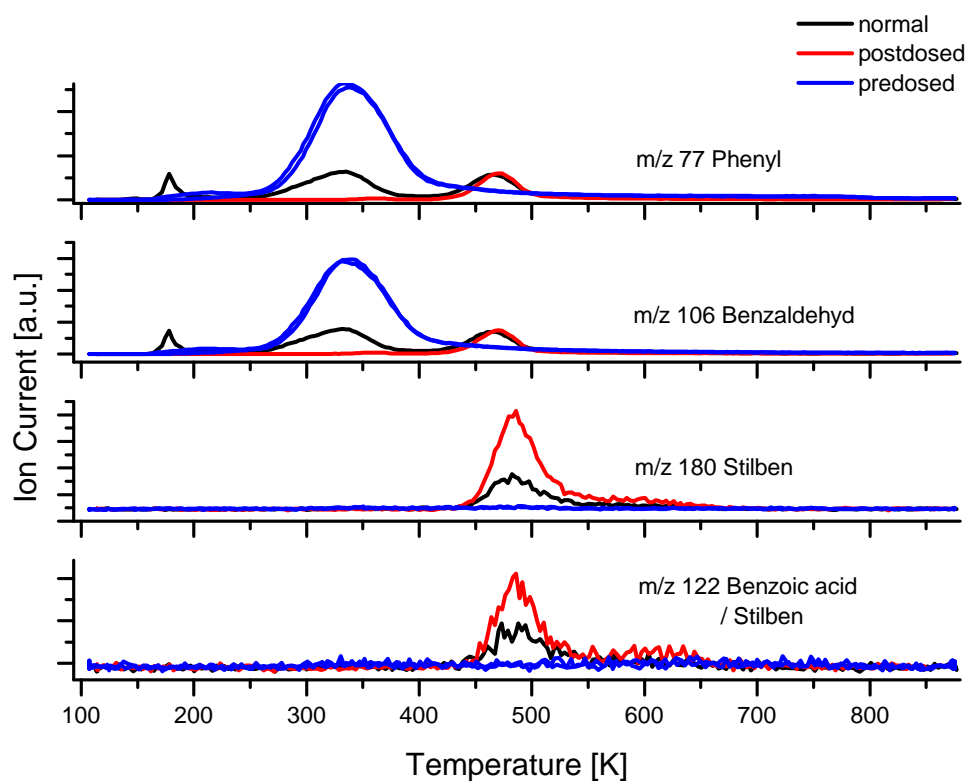


Figure 5.11: TPR spectra of a sub saturation coverage of benzaldehyde (see 20 s dosage in figures 5.2 and 5.4) with coadsorbed oxygen show no stilbene formation. A spectrum with 30 L oxygen adsorbed prior to oxygen exposure only shows the low temperature signal (blue graph). Oxygen exposure at 300 K after adsorption of benzaldehyde does not quench the stilbene yield. The crystal was reduced by 75 preparation cycles.

TPR spectrum without coadsorption of oxygen, which further indicates that less benzaldehyde has reacted. IR spectra (figure 6.4) show an oxidation to benzoic acid, which will be discussed in the following chapter.

The benzaldehyde desorption signal shifts slightly to higher temperatures with preadsorbed oxygen and has a high temperature desorption tail, which suggest a stabilisation effect of coadsorbed oxygen on benzaldehyde. A similar effect was observed for acetone.^[185] Based on DFT calculations, Plata et al.^[190] proposed a stabilization mechanism for acetaldehyde based on charge transfer. Upon adsorption the carbonyl group transfers charge to titanium atoms which accumulates at the surface and reduces the binding energy for further adsorbates. Oxygen withdraws this charge and therefore enhances adsorption of high coverages on the surface.^[190]

In contrast to previous STM results, oxygen from the gasphase is not observed to react with the interstitials once the stilbene diolate has been formed.^[139] For the red TPR spectrum in figure 5.11 benzaldehyde was adsorbed on the

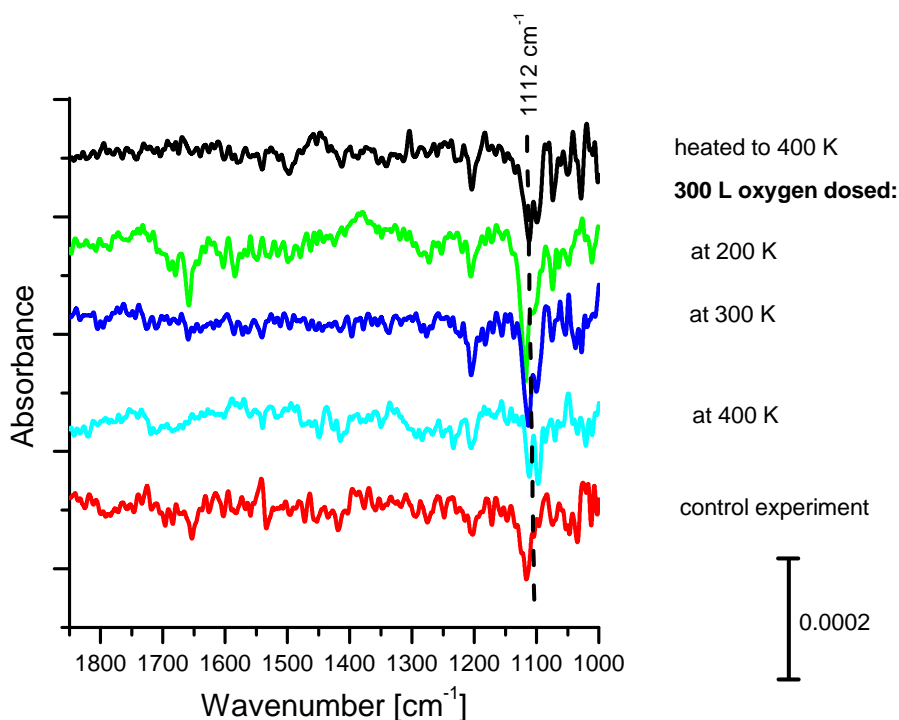


Figure 5.12: IR spectra of the effect of post dosed oxygen on the stilbene diolate. The stilbene diolate was exposed to 300 L of oxygen at various temperatures. No measurable change in intensity is observed compared to the reference experiment. For the control experiment, the sample was heated to 400 K for five minutes, which is the same thermal treatment as used during dosing oxygen at this temperature. The stilbene diolate coverage was prepared by heating a sub saturation coverage of benzaldehyde (see 20 s dosage in figures 5.2 and 5.4) to 300 K prior to exposing the sample to oxygen. The crystal was reduced by 80 preparation cycles.

surface and then heated to 300 K to form the stilbene diolate intermediate. The intermediate was then exposed to 300 L of oxygen at 300 K to reproduce the reaction conditions used by Jensen et al.^[139] Due to the temperature treatment, the low temperature species completely desorbes. However, both stilbene and high temperature benzaldehyde species are observed. Even more stilbene is formed than in the reference experiment. During heating to 300 K for 5 min for the oxygen exposure, more interstitials diffuse to the surface and are available for the reaction.

The TPRS results are confirmed by IR spectra (figure 5.12), which indicate the presence of the stilbene diolate after oxygen exposure. Changing the oxygen exposure temperature shows no significant effect on the diolate signal. Therefore, the inconsistency in the results is not due to a problem with temperature calibration. A slight reduction in intensity is observed when the sample was exposed to oxygen at 400 K. However a control experiment showed that this

effect is due to thermal desorption. For the control experiment the sample was heated to 400 K for five minutes, which is the same thermal treatment as used during dosing oxygen at this temperature.

An explanation could be the different sample preparation: The rutile crystal used in these experiments is highly reduced which suggest that there are plenty of interstitials available for the reaction. All interstitials consumed by reaction with oxygen are therefore replenished by the bulk. Assuming the crystal used by Jensen et al.^[139] was less reduced, in their case fewer interstitials were available for the reaction and the bulk defect reservoir could not sustain the surface defect density.

5.6 Conclusion

In summary, the herein presented results confirm the stilbene diolate intermediate and the involvement of interstitials in the reductive coupling of benzaldehyde to stilbene. The conversion of the adsorbed benzaldehyde to an alkoxy species is demonstrated in the heating experiments (figure 5.5) and the role of interstitials by the experiments on crystals with increasing bulk defect densities (figure 5.10). Upon heating the sample, benzaldehyde desorbs or reacts forming the alkoxy species, which presumably is the stilbene diolate. The yield of this intermediate as observed in IR spectra and stilbene observed in TPR spectra scales with the bulk defect density.

The nature of the two adsorbed benzaldehyde species could further be studied by preparation of defect rich or defect free surfaces. Such surfaces could be prepared by oxidation of the crystal, electron or ion bombardment. However, these procedures are known to change the surface structure significantly.^[113] Thus, meaningful results can only be obtained by cross checking the surface topology by scanning probe microscopy, which was not available in this study. This work validates IR spectroscopy as a method to study reactions on titania and proofs its value especially when it comes to the chemical structure of an adsorbate. The results confirm previous TPRS, DFT and STM work. No measurable effect of the bulk defect density on the optical properties in the used spectral range is observed.

6 Oxidation reactions on rutile(110)

Titania is a particularly interesting candidate for redox catalysts, because it is, in contrast to e.g. magnesia or alumina, a reducible oxide.^[15] Reducible oxides, other examples include ceria or vanadia, are easily reduced to lower oxidation states, and can therefore act as a charge buffer during redox reactions.^[191] One prominent example is the catalytic low temperature CO oxidation by gold nano particles supported on titania in which titania has been proposed to activate oxygen dissociation.^[18] Oxygen species, such as molecular oxygen, oxygen adatoms (O_{ad}) or peroxide species (OOH) are key intermediates in various reactions: For example, O_{ad} react as bases or nucleophiles on coinage metal surfaces: It has been shown that O_{ad} on gold react with methanol to adsorbed methoxy, which in turn reacts to methylformate.^[192–194]

Besides their importance for thermal chemistry, oxygen species are also involved in surface photo chemistry. Oxygen is discussed as an electron acceptor which prevents exciton recombination in hole mediated photo oxidation reactions.^[116] Besides this indirect role as electron scavenger, oxygen also is directly involved in the photo oxidation of acetaldehyde. Zehr and Henderson^[172] have shown that oxygen reacts with the adsorbate to form a photo active intermediate, which in turn decomposes under UV illumination.^[172]

Furthermore, the effect of oxygen coadsorption on chemical reactions is important to understand differences between UHV studies on model systems and applications under more realistic conditions, as oxygen and water are omnipresent in technical applications. For example, oxygen competes with benzaldehyde for the reaction with interstitials on titania and thus quenches the reductive coupling to stilbene which was confirmed by IRRAS in the previous chapter.^[28,139]

In this chapter, the reaction of oxygen with both coadsorbed benzaldehyde and coadsorbed acetone is studied using temperature programmed reaction spectroscopy (TPRS), infrared reflection absorption spectroscopy (IRRAS) and density functional theory (DFT) in order to identify the chemical properties of various oxygen species adsorbed on titania. The herein presented results give

evidence that molecular oxygen reacts as a radical and oxidizes the adsorbates to the corresponding carboxylate. On the other hand, the role of O_{ad} is not as clear. Presumably, they either react as nucleophiles with acetone to an acetal which was proposed in the literature, or as base in an aldol-like reaction which is suggested by the results presented herein.

6.1 Literature overview reaction of oxygen with coadsorbats

Understanding the reactions of oxygen on titania is challenging as various oxygen species coexist on the surface. It is known that depending on the adsorption temperature, the defect density and the surface preparation, molecular and dissociative adsorption takes place at defect sites as discussed in section 4.3. Each oxygen species shows a different chemical behavior, e.g. they can react as nucleophiles, Brønsted bases or radicals. Unfortunately, this aspect is often neglected and not systematically studied in the literature. Therefore, the discussion of literature results in the following section is occasionally ambiguous with respect to the involved oxygen species.

6.1.1 Carbon monoxide

Carbon monoxide can be accounted for the most intensively investigated probe molecule in surface science and its role as intermediate in oxidation reactions has stimulated numerous studies on titania: while the rutile(110) surface is reported to be inert for thermal oxidation of CO,^[195] the photo oxidation of CO at low temperatures is possible in the presence of molecular oxygen.^[196–198] CO was reported to adsorb on the rutile(110) surface, which was annealed in oxygen, at five fold coordinated titanium sites (Ti_{5c}).^[196] Though on a surface, which was prepared in such a way, O_{ad} were revealed by STM results (see section 4.3),^[129] no CO_2 was observed in TPR spectra.^[196] Thus, CO is not thermally oxidized by O_{ad} . However, Lu et al.^[153,154] reported that CO is oxidized by molecular oxygen (see section 4.3) upon UV exposure with energies larger than 3.1 eV. This energy threshold indicated a substrate mediated photo oxidation mechanism. As molecular oxygen requires defects for adsorption, this reaction was only observed on the vacuum annealed surface.^[197] Isotopic labeling experiments have indicated the involvement of the adsorbed molecular oxygen in the CO oxidation.

Petrik and Kimmel have concluded that the active species for CO photo ox-

idation at 30 K is molecular oxygen adsorbed at bridging oxygen vacancies (BOV).^[198] At high oxygen coverages, the CO₂ photo stimulated desorption (PSD) yield was observed to decrease as the sites next to BOVs were blocked by extra oxygen molecules for CO adsorption. Angle dependent PSD experiments showed a CO₂ desorption peak at 40° with respect to the surface and perpendicular to the bridging oxygen rows. Based on this observation, Petrik and Kimmel proposed a transition state, which forms as oxygen adsorbed at a BOV site "leans" toward the carbon atom in a CO molecule adsorbed at a neighboring Ti_{5c}. This intermediate is orientated perpendicular to the bridging oxygen rows and, therefore, explains the observed PSD angular distribution.^[198]

6.1.2 Water

The interaction of water with coadsorbed oxygen is an excellent model system to study the reactivity of the oxygen species as base. Furthermore, hydroxyl and perhydroxyl species that are similar to the ones observed from this reaction are expected due to the abstraction of hydrogen atoms from organic molecules during oxidation reactions, e.g. in the radical oxidation of aldehydes (see figure 6.3):

Oxygen was observed to react with OH groups which were adsorbed in BOV sites (OH_{br}) forming hydrogen peroxide species (HO₂⁻) and terminal OH groups (OH_t) which were both adsorbed on Ti_{5c} atoms.^[128,161] Water is known to dissociate on a vacuum annealed surface in BOV which results in two hydroxyl groups replacing oxygen atoms in the bridging oxygen rows (OH_{br}).^[26,123,199] Exposing this surface to oxygen has been observed to quench an OH_{br} recombination signal in TPRS at 520 K, whereas a new signal attributed to decomposition of an intermediate species appeared at 300 K.^[128] During this reaction, the excess charge from the defect states was consumed as indicated by EELS spectra.^[128] Two types of intermediate species were observed in the reaction at 300 K by STM: First, terminal hydroxyl groups adsorbed at Ti_{5c} sites (OH_t) which presumably formed from the reaction of O_{ad} with OH_{br} and second perhydroxyls (HO₂⁻), which have been proposed to form in the reaction of OH_{br} with molecular oxygen.^[200] DFT calculations suggested, that the perhydroxyl group is the energetically more favorable species.^[201]

Zhang et al.^[202] observed that the various hydroxyl species did not diffuse in STM images at room temperature, from which they concluded that the hydroxyl species bind strongly to the surface. However, molecular water, which was more mobile, facilitated diffusion of these species and therefore catalyzed

various reactions involving hydroxyls, oxygen and BOVs.^[26,202] For example Zhang et al.^[202] observed an indirect diffusion mechanism for O_{ad} into BOVs: water dissociated at BOVs and the resulting bridge bound hydroxyl groups reacted with O_{ad} at Ti_{5c} to regenerate water at Ti_{5c} .

The observation of features attributed to individual OH_t in STM images at room temperature,^[200] even though they should desorb based on the TPRS results,^[128] might be due to a low concentration of these groups. For desorption as water, two OH_t need to recombine leaving an O_{ad} on the surface. However due to low concentration, the OH_t are isolated and thus cannot recombine. Furthermore, these species are immobile and do not benefit from the catalytic effect of molecular water as TPRS results indicated that molecular water does not adsorb at room temperature.^[123]

Besides the thermal reactions, Perkins et al.^[203] reported a product of a photoreaction between oxygen and water, which is trapped at the interface below a thick adsorbed ice layer and desorbs as oxygen in TPRS at 160 K.

6.1.3 Carbonyl compounds

The various oxygen species on the rutile(110) surface react as nucleophiles, Brønsted bases or radicals. Examples from organic chemistry for reactions of carbonyl species are the base catalyzed aldol condensation, the Cannizzaro disproportionation, which includes nucleophile reaction steps, or the radical auto oxidation. Figures 6.1 to 6.3 show the surface bound analogues¹ of these reactions:^[176,177,204-206]

The aldol condensation (figure 6.1) is a coupling reaction of aldehydes and ketones with acidic α -hydrogen atoms. A strong base abstracts such a hydrogen atom. The resulting resonance stabilized carbanion attacks a second molecule at the carbonyl carbon atom as a nucleophile, forming a β -hydroxy aldehyde. Water can be eliminated readily to give an α, β -unsaturated carbonyl compound. All reaction steps are reversible.^[204,207] The analogue base catalyzed reaction for ketones, as shown in figure 6.1, is less favorable, as van-der-Waals repulsion between the alkyl groups destabilizes the β -hydroxy ketone intermediate.^[177] However, aldol condensations with ketones are possible by using metal enolate intermediates. In this case, the metal ion stabilizes the intermediate by binding to both oxygen atoms, which in turn compensates the destabilizing effect of the alkyl groups.^[177] A similar stabilization effect is expected for the aldol reaction at a surface.

The Cannizzaro reaction (figure 6.2) is a disproportionation of an aldehyde

¹In the remainder of this chapter, the distinction between the conventional and surface bound analogs of the reactions is neglected for better readability

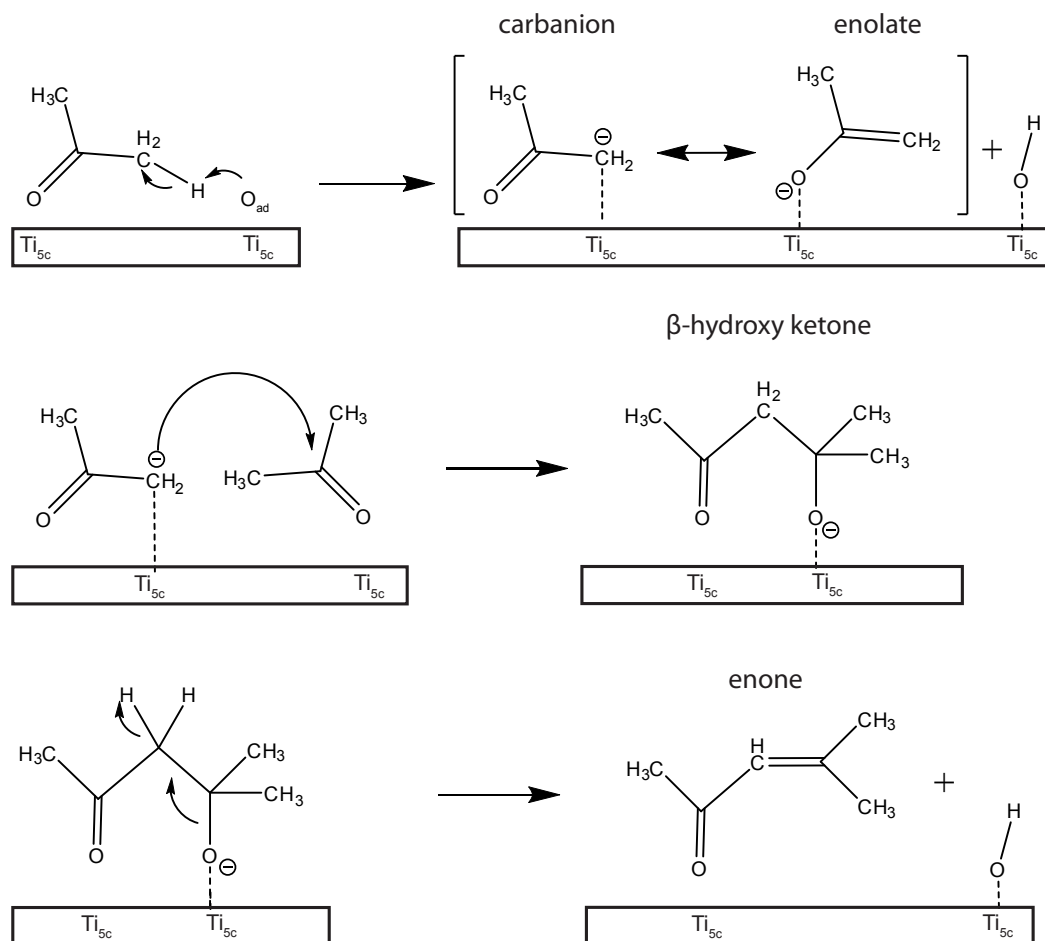


Figure 6.1: The surface analogue of the aldol condensation: The classical aldol condensation is a reaction of carbonyl components with acidic α -hydrogen atoms.^[204] A strong base abstracts such a hydrogen atom. The resulting carbanion, which is stabilized by resonance to an enolate, attacks a second carbonyl carbon atom as nucleophile. This results in a β -hydroxy ketone for the reaction of a ketone. Finally, water is eliminated to form an enone in case of the condensation of a ketone or an enal for the reaction of an aldehyde.

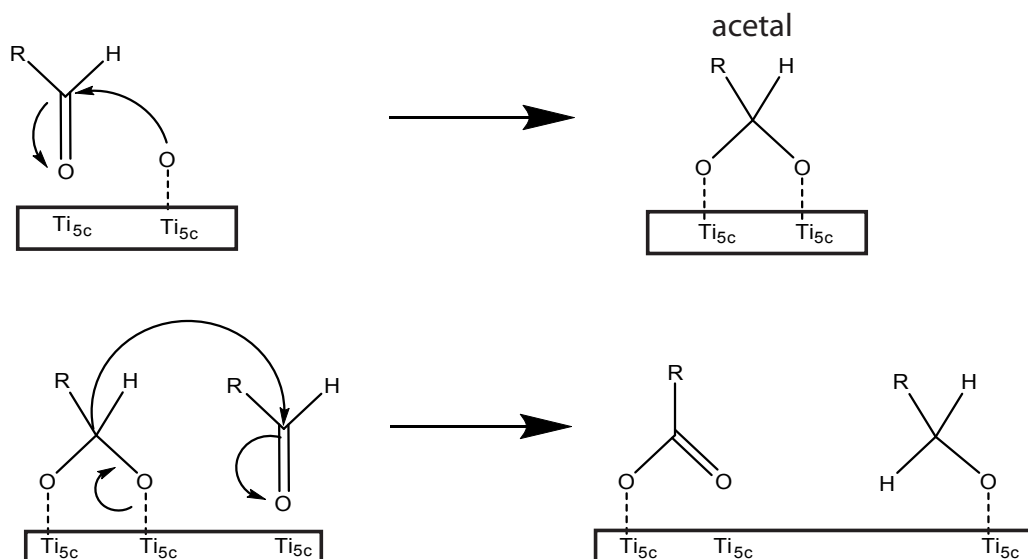


Figure 6.2: The surface analogue of the Cannizzaro reaction:^[204,205] This reaction is a disproportionation of an aldehyde forming the corresponding alcohol and acid. It involves a nucleophile reaction with the carbonyl carbon atom which produces an acetal intermediate.

forming the corresponding alcohol and acid. The reaction involves a nucleophilic attack of a hydroxy ion or an O_{ad} at the carbonyl carbon atom, which yields an acetal. The rate determining step is the subsequent hydride transfer to another aldehyde molecule, which is a second order reaction with respect to the aldehyde concentration.^[204,205] For a ketone the Cannizzaro disproportionation is not possible, but the analogue formation of a ketal² is expected. Figure 6.3 shows an adaptation of the auto oxidation mechanism for aldehydes by molecular oxygen on titania.^[177,206] Molecular oxygen has unpaired electrons and abstracts a hydrogen atom from benzaldehyde forming the allyl radical and a hydroperoxide group. These species recombine forming perbenzoic acid, which decomposes to benzoate and a terminal hydroxyl group. Previous findings reported in the literature suggest that O_{ad} on titania react as Brønsted base.^[16,126,208] For one thing, alcohols are deprotonated by O_{ad} , which yields the analogue alkoxy species on the surface.^[126,208] Therefore, O_{ad} could initiate an aldol condensation. The aldol condensation products of acetone and acetaldehyde were observed on titania nanoparticles^[209,210] and on the oxidized rutile(001) surface.^[179,181] However, neither the reduced nor oxidized rutile(110) surface show any condensation products.^[172] Indications of the initial aldol reaction step, the formation of the enolate, were reported by Henderson.^[211] He observed that O_{ad} promote the H/D exchange of adsorbed

²As acetone is a ketone, it forms a ketal instead of an acetal. For better readability, the distinction between acetal and ketal is neglected in the remainder of this chapter.

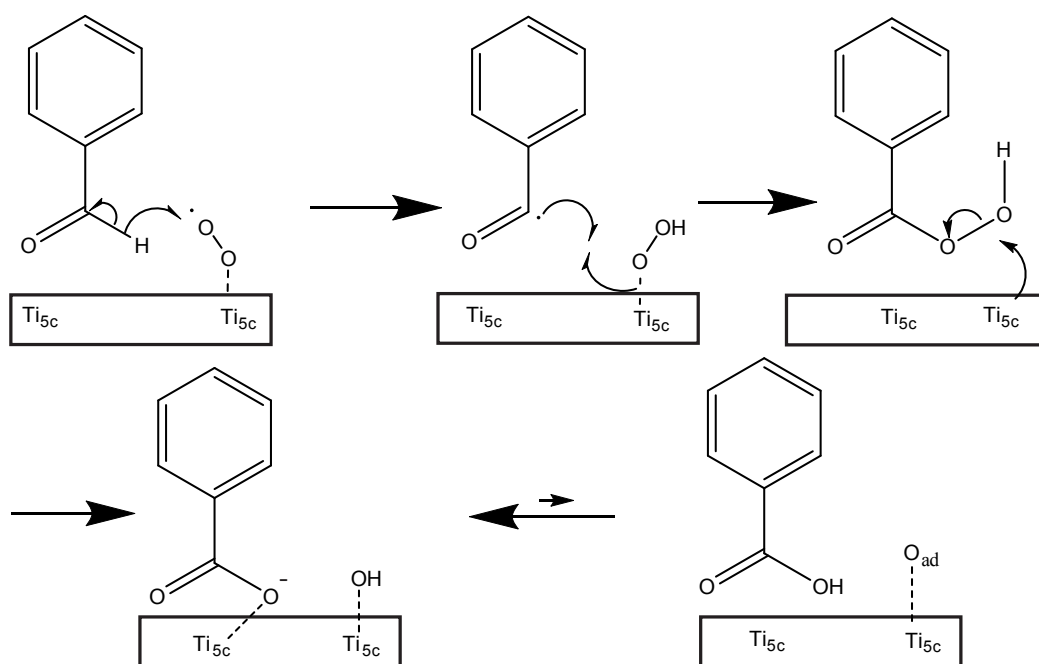


Figure 6.3: A proposed radical oxidation mechanism for benzaldehyde based on the auto oxidation mechanism for aldehydes by molecular oxygen.^[177,206] Having an unpaired electron, molecular oxygen abstracts a hydrogen atom from benzaldehyde forming the acyl radical and a perhydroxyl group. These species recombine forming perbenzoic acid which decomposes to benzoate and a terminal hydroxyl group.

acetone and proposed that an O_{ad} abstracts one of the acidic α -protons, which forms the η_1 -enolate. Deuterium is incorporated in the reverse reaction with OD groups from D_2O coadsorption. An alternative reaction mechanism which was proposed by Henderson involves the formation of an acetone-oxygen complex by a nucleophile attack of oxygen on the carbonyl carbon atom.^[211] This complex isomerizes to a propenol intermediate, which also reacts with OD groups.

A proposed nucleophilic reaction with an adsorbed oxygen species is the reaction of acetone with coadsorbed oxygen to a photo active η^2 -acetal (referred to as a diolate).^[172,173,185,212] TPR spectra have shown that acetone is stabilized by coadsorbed oxygen. This stabilized species has been found to desorb at 375 K compared to 354 K, which is the desorption temperature on vacuum annealed titania. Heating the oxygen covered surface to 460 K is known to remove all molecular oxygen as indicated by TPRS and only leaves O_{ad} .^[149] However, this pretreatment prior to acetone adsorption had no effect on the observed stabilization, thus, it was concluded that this effect is due to O_{ad} .^[212] Under UV illumination this diolate was reported to eject methyl radicals.^[172,173] Photo desorption experiments have shown that annealing acetone and oxygen to 250 K prior to illumination increases the photo desorption yield of ejected methyl radicals.^[212] Therefore, it was concluded that the formation of the proposed acetal is a thermal reaction with coadsorbed oxygen, and that this acetal is the photo active species.^[212] The activation temperature for this reaction is consistent with the involvement of O_{ad} as molecular oxygen dissociates at temperatures as low as 150-180 K.^[189] A similar reaction mechanism has been proposed for the photo oxidation of butanone.^[213]

Besides the above mentioned nucleophile reaction, acetone was reported to be converted to acetate by molecular oxygen.^[212] Annealing the preadsorbed oxygen to 460 K is known to desorb all molecular oxygen from the surface and quenches the acetate formation from acetone.^[212] Based on the well known auto oxidation mechanism a radical oxidation mechanism (figure 6.3) is proposed herein.^[177,206] Electron paramagnetic resonance (EPR) and electron energy loss spectroscopy (EELS) spectra indicated that charge was transferred from defect states to adsorbed molecular oxygen, which yielded a superoxide species O_2^- .^[151,152] This superoxide possesses an unpaired electron (like molecular oxygen) which could abstract a hydrogen atom from an aldehyde forming a perhydroxyl species and leaving an acyl radical. A similar hydrogen perhydroxyl species was reported for the reaction of water with oxygen.^[200] Furthermore, in support of the acyl radical, Jenkins et al.^[151] observed a peroxyacyl radical, which formed from the reaction of the acyl radical with oxygen, in

EPR spectra during photo oxidation of acetaldehyde on rutile powder. The acyl radical itself was not observed in that study, the authors suggested that it is too reactive to be isolated.^[151] Another example that presumably involves a radical mechanism, is the reported photo oxidation of propane by oxygen on anatase.^[214] As alkanes are chemically inert, e.g. very weak acids, bases, nucleo- or electrophiles, this reactions probably occurs via a radical mechanism as well.^[205]

6.2 Results

In this section the results for the oxidation of benzaldehyde (section 6.2.1) and acetone (section 6.2.2) are presented. These probe molecules were chosen because they show different chemical behavior: acetone has acidic hydrogen atoms and is therefore a candidate for an aldol condensation. On the other hand benzaldehyde has no acidic hydrogen atoms and therefore cannot undergo an aldol condensation but should be more easily oxidized to the benzoate either by radical oxidation or Canizarro disproportionation. Furthermore, both adsorbates were previously studied: benzaldehyde in this work and acetone in previous work by Henderson.^[185,212,213] This work extends Henderson work by IRRAS results, which differ significantly from Henderson HREELS results.

To identify the reaction products, which are observed in IR spectra, several possible intermediates are simulated using DFT. Section 6.2.3 presents DFT results on the adsorption structures and vibrational modes of several candidates.

The experiments reported herein were conducted on a strongly reduced crystal showing a dark blue colour. The crystal was reduced by roughly 80 preparation cycles (see section 3.3) for benzaldehyde and 100 cycles for acetone experiments which were conducted subsequently on the same crystal.

6.2.1 Oxidation of benzaldehyde

IR spectra of benzaldehyde (figure 6.4) with preadsorbed oxygen show the formation of benzoate at temperatures above 400 K. Benzaldehyde was adsorbed after exposing the surface to 30 L of oxygen, and IR spectra were recorded with p-polarized light. At temperatures up to 200 K, the spectra show the benzaldehyde signals: two carbonyl signals ($\nu(\text{C}=\text{O})$ 1685 and 1660 cm^{-1}), two phenyl ring modes ($\nu(\text{phenyl})$ 1601 and 1585 cm^{-1}) and the C–C stretch mode between the phenyl ring and the aldehyde carbon atom ($\nu(\text{phenyl-C})$ 1220 cm^{-1}) (see chapter 5 and table 5.1 on page 55). In agreement with the TPRS results

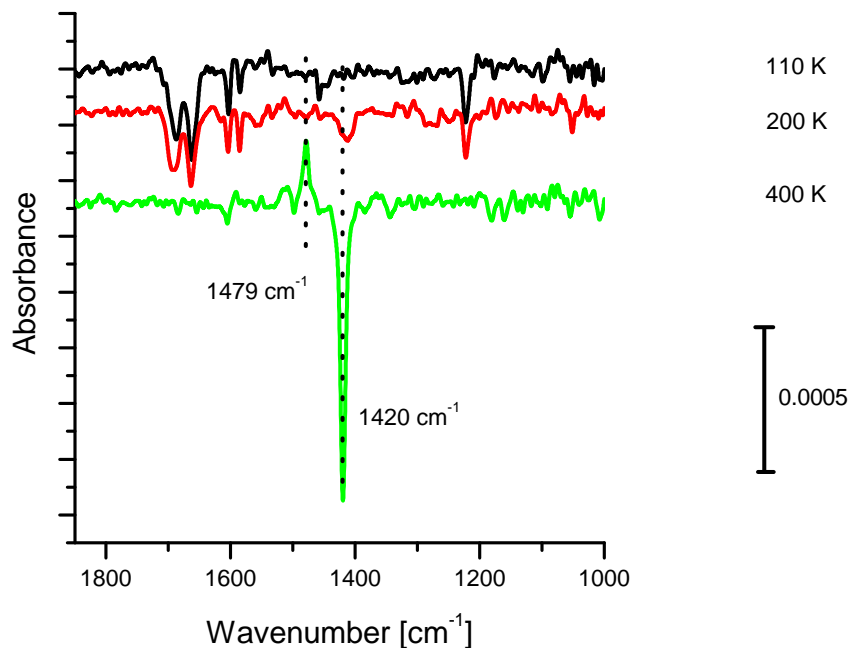


Figure 6.4: IRRA spectra of benzaldehyde oxidation - p-polarized IR spectra of benzaldehyde with 30 L of preadsorbed oxygen show the oxidation of benzaldehyde to benzoate at 400 K. The benzaldehyde signals ($\nu(\text{C}=\text{O})$: 1685, 1660 cm^{-1} , $\nu(\text{phenyl})$: 1601, 1585 cm^{-1} and $\nu(\text{phenyl-C})$: 1220 cm^{-1}) disappear and two new signals are observed for the symmetric (ν_{sym} : 1420 cm^{-1}) and asymmetric (ν_{asym} : 1479 cm^{-1}) valence stretch modes of the carboxylate group in benzoate. The sample was exposed to benzaldehyde via a 20 μm pinhole for 20 s at a pressure of 0.1 mbar (for details see section 3.5). The crystal was reduced by 80 preparation cycles.

which were presented in section 5.5, no stilbene diolate (1100 cm^{-1}) is observed which indicates that the reductive coupling is quenched. Two new signals are observed after heating the sample to 400 K: a negative signal at 1420 cm^{-1} and a positive signal at 1479 cm^{-1} . Based on comparison with sodium benzoate spectra^[184] and spectra of adsorbed formate on rutile(110),^[47] these signals are tentatively assigned to the symmetric and asymmetric stretch modes of adsorbed benzoate (see table 6.1).

Further evidence for benzoate formation is given in the TPR spectra (figure 6.5). Benzoate is difficult to detect in TPRS, as it binds very strongly to the surface and decomposes above 700 K. The main decomposition products are a benzaldehyde fragment (m/z 105) and the decarboxylation products benzene (fragment m/z 78) and CO_2 (fragments m/z 44, 28).^[215] Though the benzaldehyde fragment is covered by the pump tail of the benzaldehyde desorption signal at 350 K, the decarboxylation signals (m/z 78, 44, and 28) indicate benzoate decomposition at 760 K. A quantitative analysis of the TPR

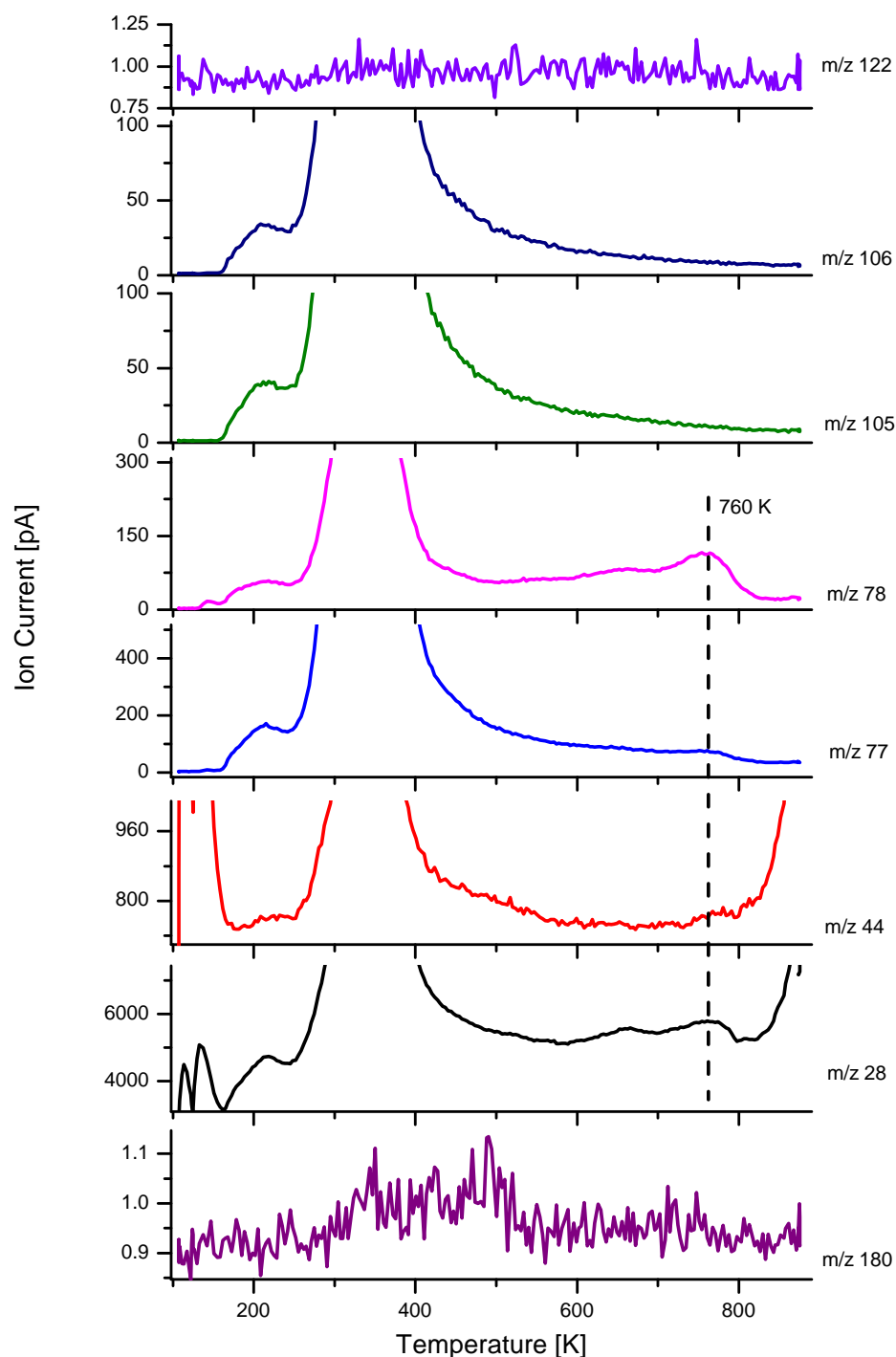


Figure 6.5: TPRS fragments indicating benzoate: benzoate is difficult to detect in TPRS as it decarboxylates at high temperatures.^[215] Observed fragments are benzene (m/z 78) and CO_2 (m/z 44, 28). Other fragments such as m/z 105 and 77 are covered by the pump tail of the benzaldehyde desorption signal at 350 K (m/z 106 etc.). No benzoic acid is observed (m/z 122) and the stilbene formation from reductive coupling is quenched by the coadsorbed oxygen (m/z 180). The sample was exposed to benzaldehyde as described in figure 6.4, the crystal was reduced by 75 cycles.

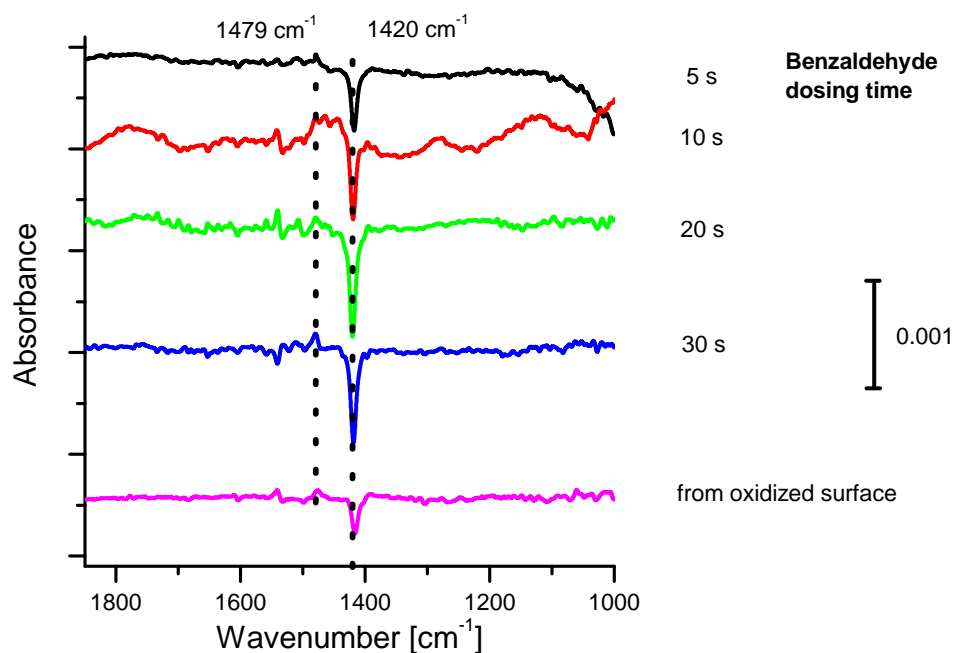


Figure 6.6: Influence of benzaldehyde coverage on the oxidation yield, increasing the initial benzaldehyde exposure only slightly increases the benzoate yield observed in IR. The decrease in yield is observed by preparing an oxidized surface without molecular oxygen. In each case the surface is saturated with 30 L of oxygen at 110 K prior to dosing benzaldehyde. The sample is exposed to benzaldehyde as described in figure 6.4. Based on the TPR spectra in figure 5.2, a 30 s dosage corresponds to dosing a mono layer of benzaldehyde. The crystal was reduced by 80-90 preparation cycles.

spectra based on the relative integrated areas of the high temperature CO signal at 760 K, including a shoulder at lower temperature to the total amount of m/z 28 signal indicates that less than 8% of the adsorbed benzaldehyde is oxidized to benzoate. This estimation is based on the assumption that the ionization cross section and the formation probability of CO^+ fragments from benzaldehyde fragmentation and benzoate decomposition, is similar (for details see section 3.6). As m/z 28 is only a minor fragment of benzaldehyde, this value presumably overestimates the benzoate yield.^[34]

The IR spectra indicate that benzoate adsorbs with the carboxylate group orientated parallel to the Ti_{5c} rows. No benzoic acid is formed as indicated by the presence of the carboxylate signals and the absence of a carbonyl signal in the wavenumber range from 1650 cm^{-1} to 1700 cm^{-1} .^[43] The surface selection rules for IR on titania (see section 2.3) indicate that the symmetrical stretch mode (ν_{sym}) is aligned perpendicular to the surface. However, the asymmetrical stretch mode (ν_{asym}) appears as a positive signal in IR spectra, which indicates an alignment parallel to the surface and the plane of incidence. Ac-

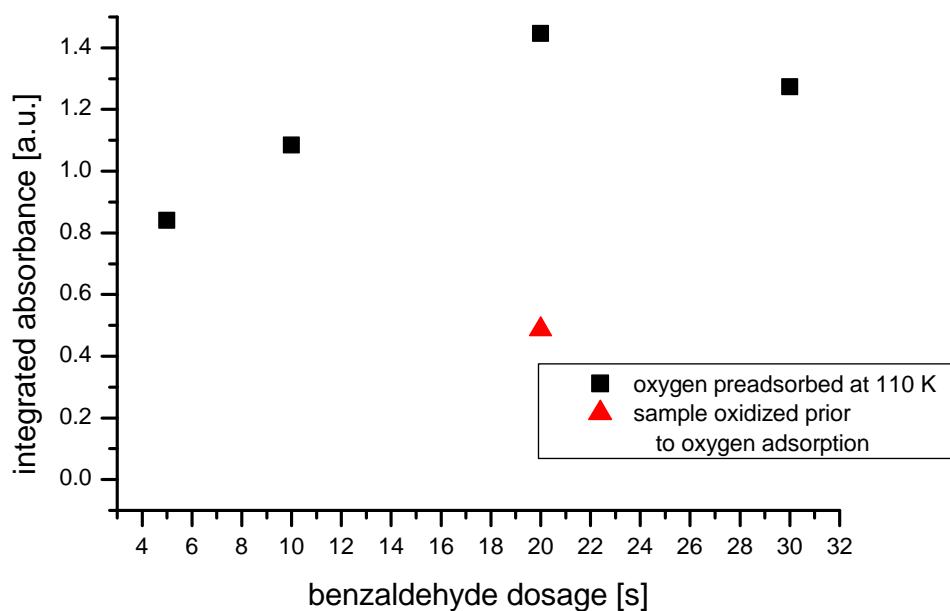


Figure 6.7: Coverage dependent benzoate yield based on the integrated IR intensities (figure 6.6). The benzoate yield saturates at roughly 1 ML coverage.

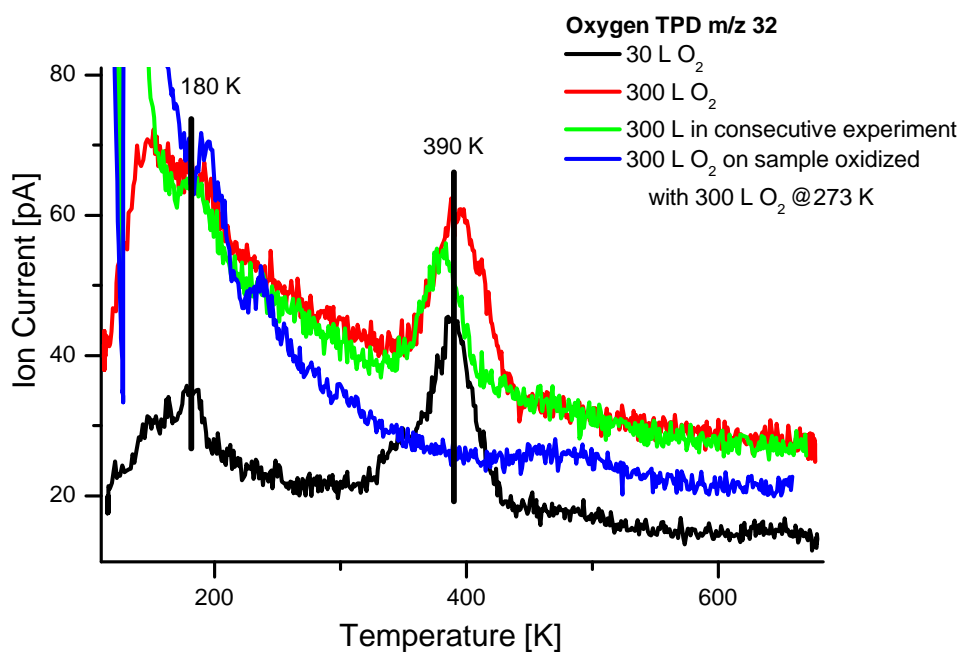


Figure 6.8: Preparation of an oxidized surface - Only oxidation of the surface by an exposure to 300 L oxygen at 273 K quenches the molecular oxygen desorption peak at 390 K (blue spectrum). Oxygen was dosed at 110 K.

ording to LEED diffraction, the crystal is oriented in such a way that the plane of incidence of the IR-beam is parallel to the $\langle 001 \rangle$ direction which is parallel to the Ti_{5c} rows. Thus, the data gives strong evidence that benzoate adsorbs parallel to the Ti_{5c} rows. A similar alignment was observed for formate on rutile(110).^[47]

The benzoate yield slightly increases with benzaldehyde coverage (figures 6.6 and 6.7). The TPR spectra (figure 6.5) indicate that only a small percentage of benzaldehyde is oxidized to benzoate, which suggests that the amount of oxygen is limiting the reaction yield in the presence of an excess of benzaldehyde. However, the yield increases slightly with benzaldehyde coverage up to a coverage of roughly one mono layer. An Arrhenius plot of the logarithm of the integrated IR area vs. the logarithm of the dosing time, (data not shown) indicates a reaction order in benzaldehyde of less than 0.5.

Benzaldehyde is oxidized by molecular oxygen, as indicated by the loss in reaction yield on an oxidized surface. The spectrum labeled "from oxidized surface" in figure 6.6 was recorded after oxidizing the surface in 300 L oxygen exposed at 300 K prior to adsorption of oxygen at 110 K. This procedure quenches the molecular oxygen desorption signal in TPR spectra (figure 6.8) but leaves O_{ad} on the surface.^[129,189] Therefore, a molecular oxygen species is involved in the oxidation of benzaldehyde. Additionally, Henderson observed a similar oxidation of acetone to acetate by molecular oxygen.^[185] This reaction was quenched after heating the oxygen covered surface to 450 K to remove adsorbed molecular oxygen.^[185] Even though the surface is oxidized, a small amount of benzoate is still formed. This is probably due to a small amount of molecular oxygen which is adsorbed on the surface, but not detected in TPRS.

6.2.2 Oxidation of acetone

The surface chemistry of acetone has been previously studied by Henderson using TPRS and HREELS, and the results were discussed in the literature section.^[185] In this work, initially the TPRS results were reproduced to ensure consistency with Henderson's result prior to the IRRAS experiments.

TPR spectra (figure 6.9) of acetone show the stabilization of acetone by coadsorbed oxygen and the formation of acetate.^[185] The TPR spectra in figure 6.9 show the fragment m/z 42, which is a common fragment of acetone and ketene from acetate decomposition for two acetone exposures. With preadsorbed oxygen, the 240 K acetone signal, which is assigned to acetone desorbing from Ti_{5c} atoms, shifts to 285 K.^[185] This signal shows a shoulder at 320 K. An extra

signal appears at 385 K. The broad desorption signal >600 K is due to acetate decomposition.^[185] In contrast to Henderson's results, the 385 K signal in these spectra is less pronounced.^[185] This difference is possibly due to differences in the preparation history of the crystal, which changes the defect density.

IR spectra of acetone (figure 6.10) suggest the formation of acetate and an intermediate which could either indicate an acetal or an enone. At 110 K, two carbonyl signals are observed at 1727 cm^{-1} and 1698 cm^{-1} . The 1727 cm^{-1} signal disappears upon heating to 250 K whereas the 1698 cm^{-1} species grows in intensity and two new species appear at 1196 cm^{-1} and 1018 cm^{-1} . The 1196 cm^{-1} signal suggests an acetal (see figure 6.12), this species is discussed in more detail below. The 1018 cm^{-1} signal indicates an alkoxy species, e.g. methoxy from a radical oxidation or the $\nu_{\text{sym}}(\text{C-O})$ stretch mode in an acetal. Upon heating to 300 K, the carbonyl signal disappears, though acetone desorption is observed up to 385 K in TRPS.

In contrast to benzaldehyde, only one monolayer carbonyl signal is observed. The 1727 cm^{-1} signal is only slightly shifted from the reference IR spectrum of a liquid acetone film at 1715 cm^{-1} .^[184] Additionally, it completely desorbs after heating to 250 K. Thus, this species is probably due to the physisorbed species which desorbs at 140 K in TPR spectra. In analogy to the signals observed for benzaldehyde, the 1698 cm^{-1} species suggests a η_1 -bound acetone adsorbed at Ti_{5c} atoms. The herein reported value concurs with previously reported HREELS results at 1690 cm^{-1} on rutile titania and 1710 cm^{-1} on silver(111).^[185,192] In contrast to benzaldehyde, no second carbonyl species is observed. The second benzaldehyde species was assigned to adsorption at defect sites (see chapter 5). A possible explanation is that the acetone's methyl groups prevent alignment of the carbonyl group to bind to an exposed Ti_{5c} atom.

The species at 1196 cm^{-1} is either an acetal or a β -hydroxy ketone, which forms in an aldol reaction. An acetal was proposed by Henderson and Zehr.^[172,173] In previously reported HREEL spectra, this species was not observed.^[185] It was probably covered by a multiple phonon loss at 1210 cm^{-1} .^[185] A similar signal was observed in HREELS for reaction of acetone with O_{ad} on silver(111) at 1190 cm^{-1} , which was assigned to the $\nu_{\text{asym}}(\text{COC})$ of an acetal.^[192] This assignment was based on HREEL spectra of the reaction product of formaldehyde with O_{ad} .^[216] The transition dipole moment of the ν_{asym} is parallel to the surface. Therefore, it should appear as a positive signal in IR spectra on titania. However, DFT calculations on selected model components presented in figure 6.12 in the following section show symmetrical in plane bending modes ($\delta(\text{CCC})$) in the frequency range 1140 cm^{-1} to 1260 cm^{-1} (see table 6.2).^[187]

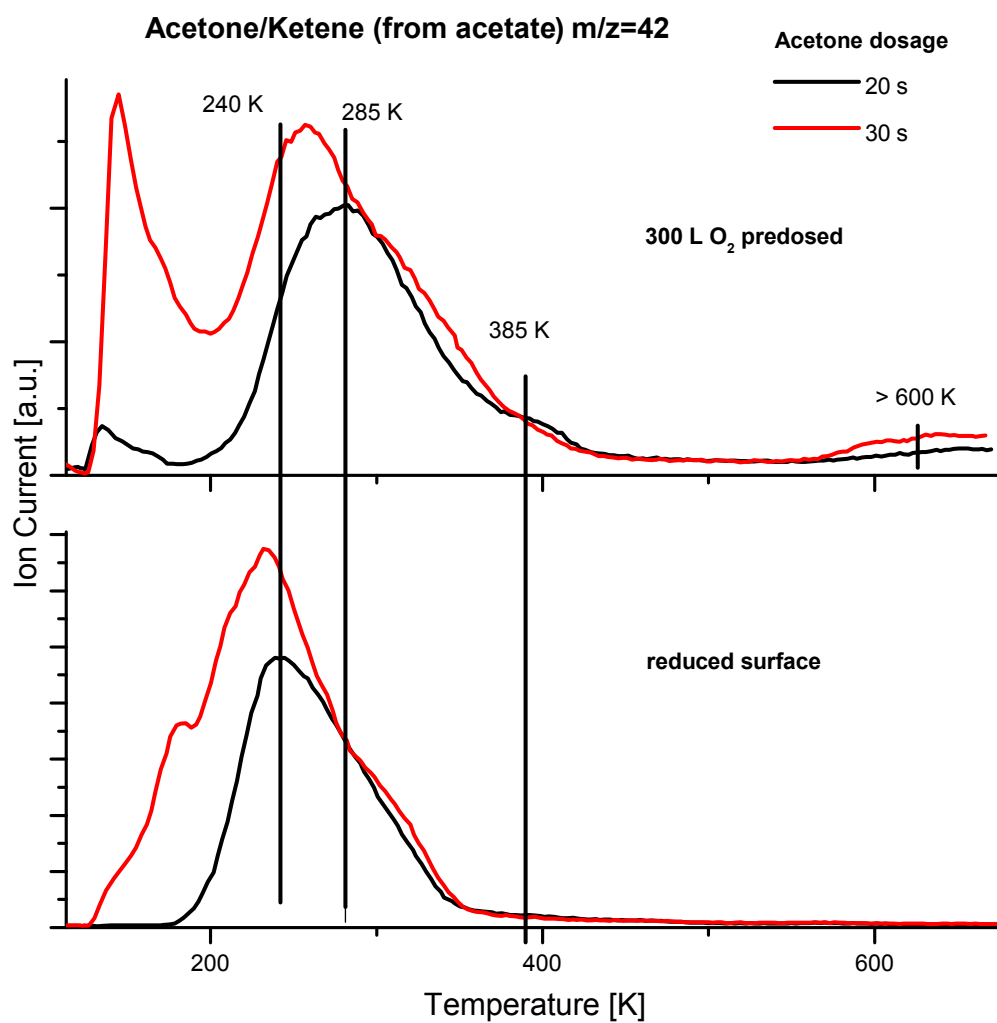


Figure 6.9: TPR spectra of acetone adsorbed on a reduced surface and with coadsorbed oxygen. After 30 s of exposure, the mono layer is saturated. With preadsorbed oxygen, the desorption signals are shifted to higher temperatures and a new signal at 385 K is observed. Acetone was dosed via a $20\ \mu\text{m}$ pin hole at a pressure of 0.1 mbar. The crystal was reduced by 110 preparation cycles.

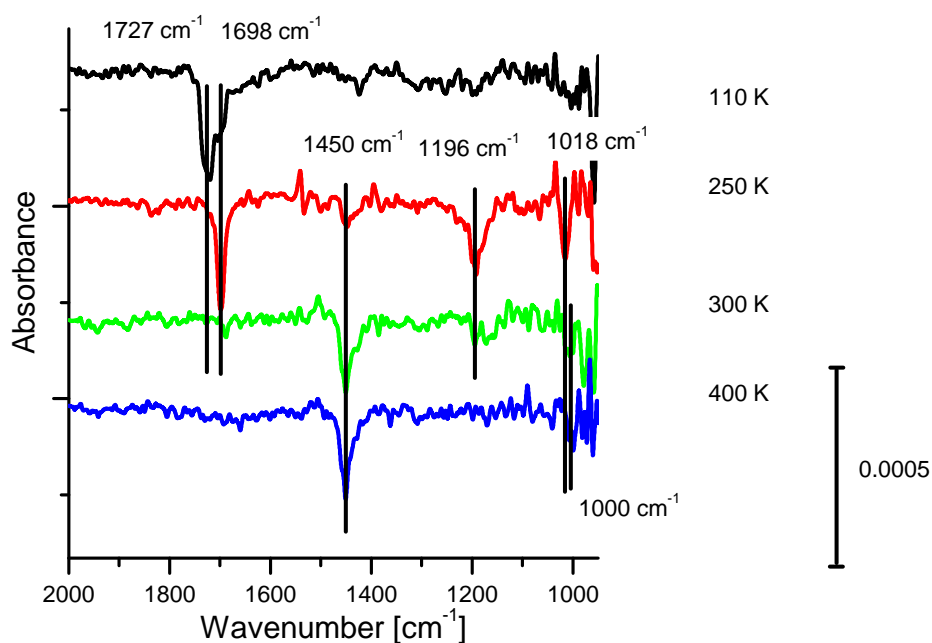


Figure 6.10: P-polarized IRRA spectra of the reaction of acetone with coadsorbed oxygen. Upon heating the carbonyl signals at 1727 cm^{-1} and 1698 cm^{-1} disappear. Two new signals suggest the formation of acetate ($\nu_{\text{sym}}(\text{OCO})$: 1450 cm^{-1}) and possibly an acetal ($\nu_{\text{sym}}(\text{CCC})$: 1196 cm^{-1}). Roughly one mono layer of acetone was adsorbed as described in figure 6.9 on a crystal reduced by 115 preparation cycles.

Another interpretation of this signal is a β -hydroxy ketone, an intermediate in the aldol condensation, which will be discussed in detail in section 6.3.

The IR spectra suggest that the stabilization effect for acetone observed in TPRS is due to the formation of the intermediate species indicated by the signal at 1196 cm^{-1} . The IR spectra show that the intermediate forms below 250 K and is mostly desorbed at 300 K, which coincides with the observed desorption in TPR spectra. The coexistence of the 1196 cm^{-1} signal and carbonyl signal hints to the formation of a β -hydroxy ketone in an aldol reaction, or an acetal which is coadsorbed with unreacted η_1 -bound acetone.

Based on DFT results, Plata et al.^[190] proposed an alternative model for stabilization of acetaldehyde by oxygen: Upon adsorption, acetaldehyde donates charge to the surface, which accumulates with increasing coverage. This charge lowers the lewis acidity of the titanium atoms and thus destabilizes further adsorbats. The stabilization effect of oxygen is based on the consumption of this excess charge. The IR spectra show a carbonyl signal, which indicates the presence of η_1 -acetone, which would concur with the model by Plata et al. However, the intermediate signal at 1196 cm^{-1} suggests that the stabilization effect is more likely due to the formation of this acetone-oxygen product as proposed by Henderson.^[185]

The residual intermediate signal observed in IR spectra at 300 K is likely due to a minority species adsorbed at point defect or kink sites, which desorbes at 385 K in TPRS. Due to the exposure with oxygen, the surface is presumably covered with small TiO_2 islands from the reaction of oxygen with interstitials at 300 K (section 4.3). The density of these islands, and thus the amount of kink sites, increases with the bulk defect density. Therefore, a difference in reduction of the sample would explain the higher intensity of the TPRS signal observed at 385 K in Hendersons work, compared to the results presented in this work.^[185]

6.2.3 DFT results

In order to identify the reaction intermediates observed in the IR spectra, several possible intermediates were simulated using density functional theory (DFT) calculations. The B3LYP hybrid functional^[81,82] and a 6-311+G(d,p) basis set^[83-85] were applied as implemented within the Gaussian 09 software package.^[217] Tests with several adsorbate models suggest that this functional is sufficiently accurate for the purpose of this work (see appendix 2). For all calculations the adsorbate geometry was optimized prior to the frequency calculation.

Generally, DFT methods overestimate the vibrational frequencies for two reasons: first they are based on the harmonic oscillator model and, therefore, neglect anharmonicity and second they do not fully describe electron correlation. However, as the deviation is systematic for most systems, it can be compensated by an according empirical scaling factor.^[76,218,219] For the B3LYP functional with a 6-31++G** basis set, a factor of 0.964 was determined from comparison of calculated spectra with experimental spectra.^[218,219] However, these scaling factors were determined for free molecules and possibly do not apply for adsorbates on a cluster. Therefore, the frequencies reported herein are tentatively not scaled and should systematically deviate to higher values. For each intermediate relevant in this work, a molecular reference and the species adsorbed on a $\text{H}_8\text{Ti}_2\text{O}_8$ cluster were simulated. The $\text{H}_8\text{Ti}_2\text{O}_8$ cluster was chosen to resemble the Ti_{5c} adsorption sites on the rutile(110) surface. It consists of two Ti atoms each coordinated by five oxygen atoms, which are saturated by hydrogen atoms. This model is only suitable for a preliminary screening of candidates as it neglects several aspects in the surface science of titania, such as the influence of bridging oxygen atoms, adsorbates in adjacent sites and all kinds of defects. The coordinates for the atoms in the cluster were taken from DFT results by Jan Haubrich and frozen during the geometric optimization of the system.^[100] The input coordinates are listed in section 1. The results for the molecular reference, e.g. a methyl ether for an alcoholate, were compared to NIST or SDBS reference spectra to estimate the reliability of the used computational method.^[184,186]

Additionally, a sodium adduct was used as a very simple model for the lewis acid centers on the surface to estimate the impact of coordination for some intermediates. For systems containing two sodium atoms, the distance between the two atoms was fixed at 2.9 Å, which is the distance between two Ti_{5c} atoms on the rutile(110) surface.^[118] In some cases an adsorption geometry parallel to two sodium atoms was enforced, e.g. for the acetal compounds, the dihedral angle between the two oxygen and sodium atoms was fixed at 0° for the geometry optimization. This model was chosen in this work based on experience with reference spectra for sodium benzoate, which reproduced the carboxylate IR signals very well (see table 6.1).

Even though the used cluster model is simplified and only intended for preliminary investigations of potential intermediates, the herein presented results are most helpful to identify vibrational modes of adsorbates. The main benefit compared to using simple reference spectra from databases, where the molecules were measured in e.g. liquid films, is that computational results indicate the alignment of the transition dipole moment with respect to the

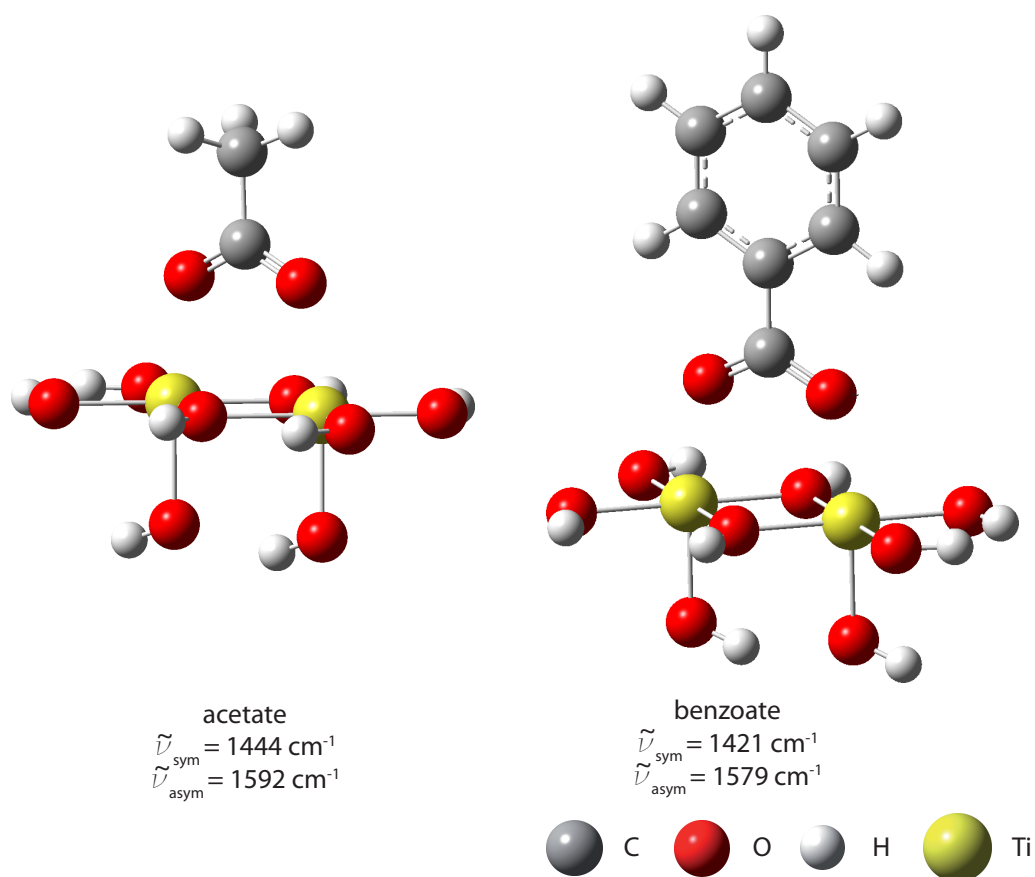


Figure 6.11: DFT results for acetate and benzoate on the $\text{H}_8\text{Ti}_2\text{O}_8$ cluster model. The simulated spectra show strong signals for the symmetric (ν_{sym}) and asymmetric (ν_{asym}) modes of the carboxylate group.

surface. This information is crucial to the interpretation of IRRA spectra, due to the surface selection rules discussed in section 2.3. Furthermore, the assignment of vibrational modes in reference spectra based on handbooks is not always unambiguous. Especially in the frequency range from 1000 cm^{-1} to 1500 cm^{-1} , several vibrational modes overlap in their expected frequency range.^[43]

Benzoate and acetate

To provide further evidence for the IR spectra assignment of the carboxylate species (figures 6.4 and 6.10), the IR spectra of the acetate and benzoate model compounds were simulated (see figure 6.11): The calculated spectra show two strong vibrational modes, namely the symmetric carboxylate stretch mode $\nu_{\text{sym}}(\text{OCO})$, which is orientated perpendicular to the surface, and the asymmetric stretch mode $\nu_{\text{asym}}(\text{OCO})$, which is orientated parallel to the surface. The computational results for the symmetric stretch mode ν_{sym} of benzoate

Table 6.1: Carboxylate vibrations for acetate and benzoate (see figure 6.11).
 p: mostly parallel to surface, +/-: observed as positive or negative
 absorbance signal, n.o.: not observed

	$\nu_{\text{sym}}[\text{cm}^{-1}]$	$\nu_{\text{asym}}[\text{cm}^{-1}]$
Benzoate		
free benzoate anion	1333	1671
sodiumbenzoate	1409	1559
sodiumbenzoate KBr disc ^[184]	1413	1553
benzoate on $\text{H}_8\text{Ti}_2\text{O}_8$ cluster	1421	1579(p)
IRRAS this work	1420(-)	1479(+)
Acetate		
free acetate anion	1345	1648
sodiumacetate	1428	1571
sodiumacetate KBr disc ^[184]	1413	1553
acetate on $\text{H}_8\text{Ti}_2\text{O}_8$ cluster	1444	1592(p)
IRRAS this work	1450(-)	n.o.
Formate (as reference)		
formate on $\text{H}_8\text{Ti}_2\text{O}_8$ cluster	1382	1611(p)
formate on rutile(110)(IRRAS) ^[47]	1363(-)	1566(+)
formate on rutile(110)(HREELS) ^[220]	1365	
sodiumformate KBr disc ^[184]	1352	1611

are in good agreement with the reference spectra from the SDBS database for the sodium salts and the herein reported experimental value for adsorption on rutile(110) (see table 6.1).^[184] Upon coordination, the mode shifts from 1333 cm^{-1} for the free benzoate anion to 1420 cm^{-1} for adsorption on the cluster model. In contrast to the symmetric mode of benzoate, the asymmetric mode is overestimated by 100 cm^{-1} for adsorption on the cluster compared to the experimental value. The animation of the asymmetric mode shows a coupling of this mode with vibrations of the lattice oxygen atoms within the cluster. Therefore, this deviation is most likely due to an inaccurate representation of the lattice oxygen atoms within the cluster model. Qualitatively similar results are obtained for acetate except for that the asymmetric mode is not observed in the IRRA spectra.

Acetals

One possibility for the interaction of acetone with coadsorbed oxygen is a nucleophilic reaction at the carbonyl carbon atom, which is similar to the initial step of the Cannizzaro reaction (figure 6.2). This reaction forms an acetal intermediate as presented in figure 6.12 for acetone and 6.13 for the analogue benzaldehyde species. The calculated spectra for the acetone acetal show two strong signals: a symmetric inplane bending mode of the carbon bonds $\delta(\text{CCC})$

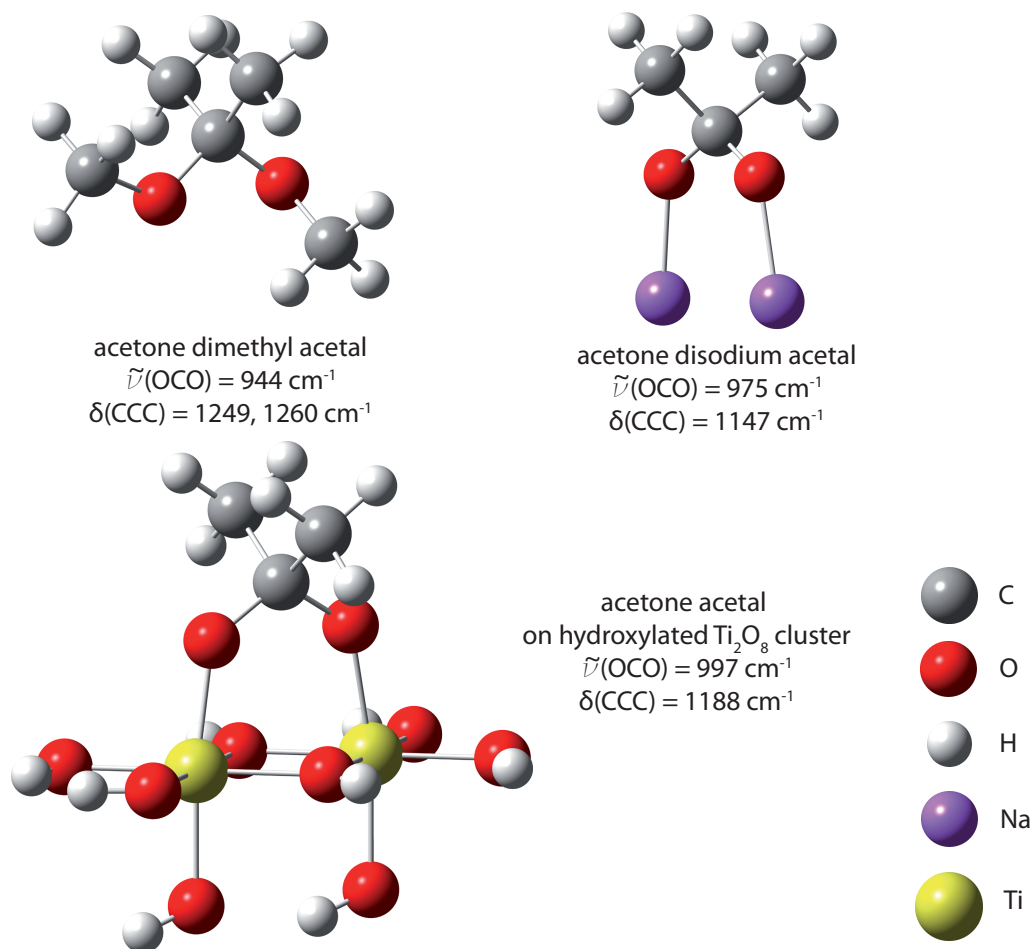


Figure 6.12: DFT results for acetone acetals: The various acetals show two modes: $\nu_{\text{sym}}(\text{OCO})$ and $\delta(\text{CCC})$. Due to coupling with the two differently aligned methoxy groups, two $\delta(\text{CCC})$ are observed for the dimethyl acetal.

and a symmetric stretch mode of the C–O bonds $\nu_{\text{sym}}(\text{OCO})$ (see table 6.2). The transition dipole moment of both modes is orientated perpendicular to the surface. For the $\delta(\text{CCC})$ of the dimethyl acetals, two different signals are observed e.g. at 1249 cm^{-1} and 1260 cm^{-1} for the calculated spectrum, due to coupling with the methoxy groups, which have a different orientation. The signals shift to 1188 cm^{-1} for the adsorbate on the cluster and 1147 cm^{-1} for the disodiumacetal. The analogue $\delta(\text{CCH})$ for the benzaldehyde acetals shows a similar trend.

Aldol intermediates

Another possibility for the reaction of acetone with oxygen is an aldol-like reaction. The initial step would be the abstraction of an acidic hydrogen atom, which would lead to isopropenolate (see figure 6.14). This isopropenolate

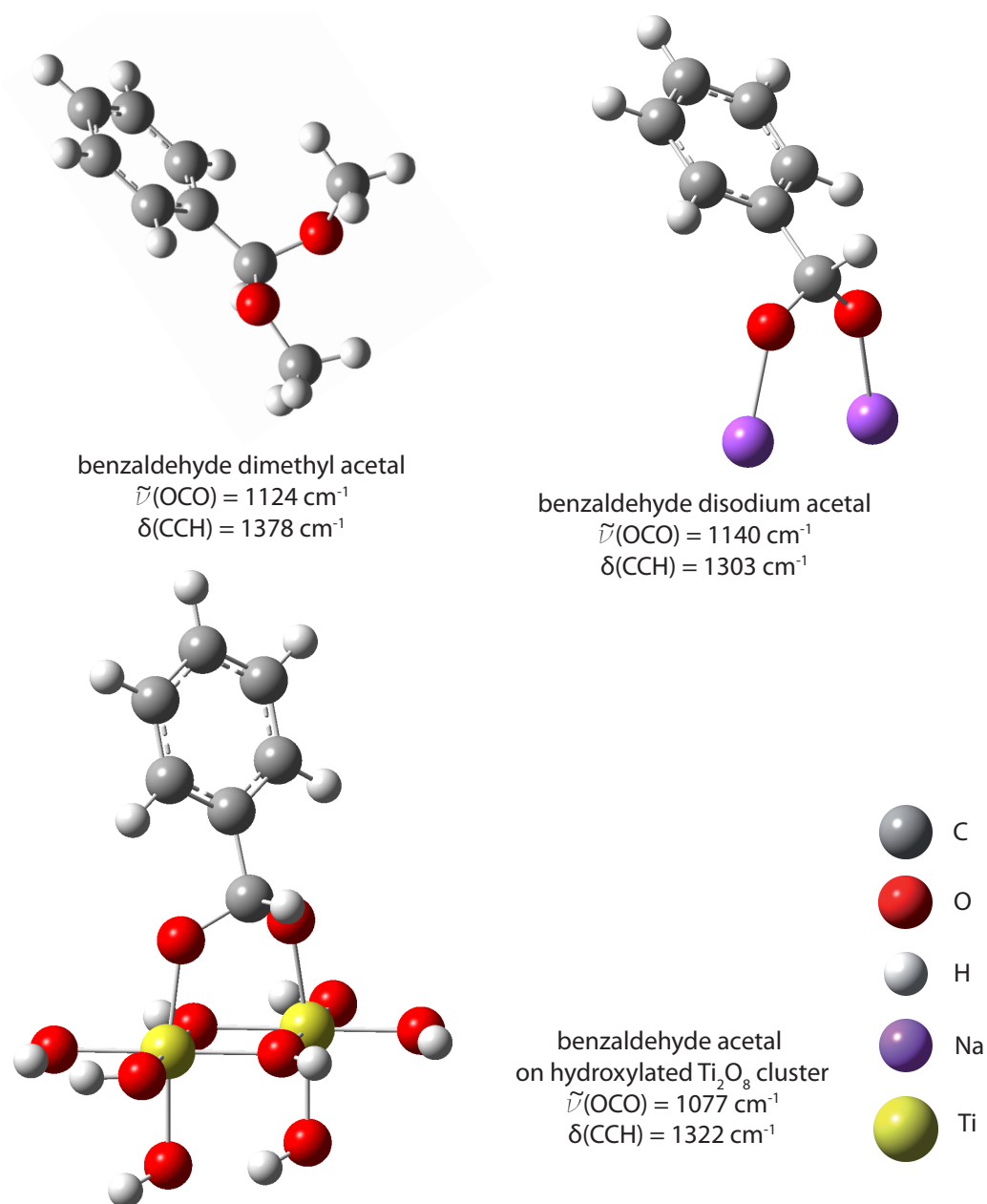


Figure 6.13: DFT results for benzaldehyde acetals. Also see description figure 6.12. In contrast to the acetone acetals, the benzaldehyde acetals show a $\delta(\text{CCH})$ instead of a $\delta(\text{CCC})$ mode.

Table 6.2: Reference vibrations for acetals (see figures 6.12 and 6.13).

p: mostly parallel to surface, +/-: observed as positive or negative absorbance signal, n.o.: not observed

	Acetone		Benzaldehyde	
	$\delta(\text{CCC})$ [cm ⁻¹]	$\nu_{\text{sym}}(\text{COC})$ [cm ⁻¹]	$\delta(\text{CCH})$ [cm ⁻¹]	$\nu_{\text{sym}}(\text{COC})$ [cm ⁻¹]
dimethylacetals	1249,1260	944	1378	1124
dimethylacetals liquid film ^[184]	1217,1182	929?	1358	1106,1056
disodiumacetals	1147	975	1303	1140
acetals on H ₈ Ti ₂ O ₈ cluster	1188	997	1322	1077
IRRAS this work	1196(-)	1018(-)	n.o.	n.o.

could react with a second acetone molecule to form a β hydroxy-ketone which in the case of acetone is 4-hydroxy-4-methylpentane-2-one (figure 6.15). Because there are no α -hydrogen atoms in benzaldehyde, this reaction pathway is only possible for acetone.

For isopropenolate two possible orientations were simulated: one with the C=C double bond orientated perpendicular (figure 6.14) and one parallel to the surface (not shown). Within the limits of the cluster model, both structures are almost identical in energy ($\Delta E = 0.04$ eV). Thus both the C–C and C=C modes can be oriented parallel and perpendicular to the surface.

The 4-hydroxy-4-methylpentane-2-one shows a strong carbonyl signal and various C–C stretch modes, which are, some more, some less, orientated perpendicular to the surface. These modes show relatively large differences between the sodium adduct and the adsorbate on the H₈Ti₂O₈ cluster (see table 6.3). Presumably, the pentane backbone of this molecule is more flexible than e.g. the phenyl ring in benzaldehyde and its orientation is more sensitive to environmental effects. Since the herein used cluster model neglects most of these effects, especially the impact of the bridging oxygen rows, the results for this species are less reliable than for the aforementioned intermediates.

In summary, the obtained unscaled vibrations for the $\nu_{\text{sym}}(\text{OCO})$ of benzoate and acetate are in excellent agreement with the experimental results. The discrepancy for the $\nu_{\text{asym}}(\text{OCO})$ for benzoate was further examined in appendix 2 and is most likely due to the limitations of the used H₈Ti₂O₈ cluster model (see appendix 1), and not due to the computational method. Presumably, the discrepancy is due to the inaccurate description of the coupling of the ν_{asym} mode with vibrations of the oxygen atoms in the cluster. Thus, the previously reported scaling factors appear not to apply for the adsorbates studied in this work. These results suggest, that the used computational model is sufficiently

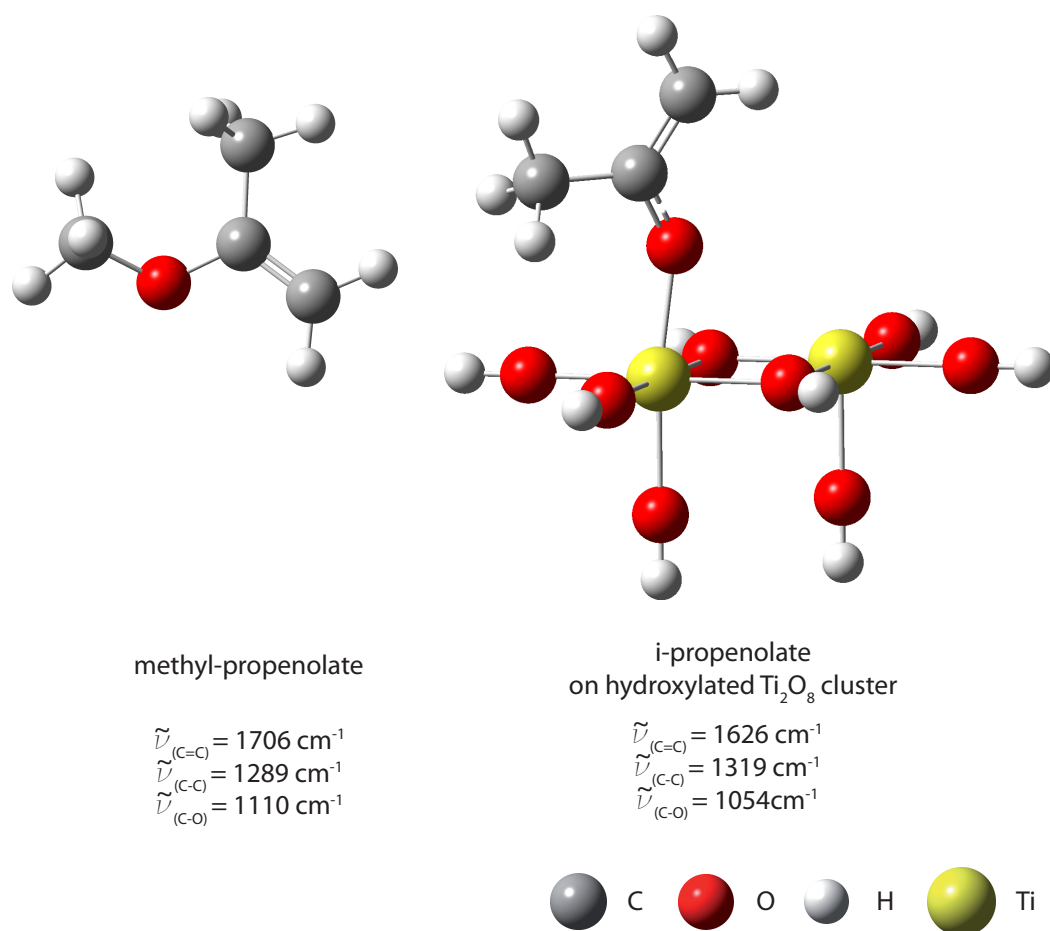


Figure 6.14: DFT results for isopropeneolate. For the isopropeneolate on the $\text{H}_8\text{Ti}_2\text{O}_8$ cluster, adsorption with the $\text{C}=\text{C}$ double bond parallel to the surface is possible as well (not shown). Thus both the $\nu(\text{C}-\text{C})$ and $\nu(\text{C}=\text{C})$ modes can be oriented parallel and perpendicular to the surface.

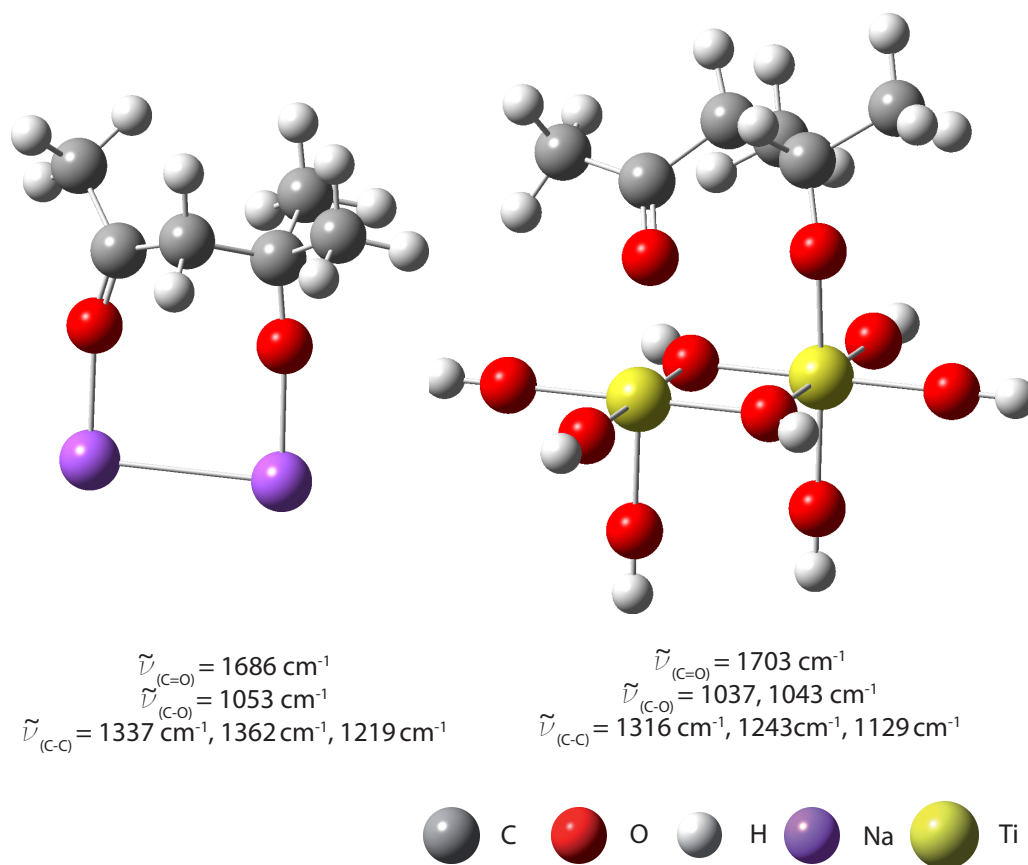


Figure 6.15: 4-hydroxy-4-methylpentane-2-one forms as an intermediate on the surface in an aldol-like reaction. The spectra show a $\nu(\text{C}=\text{O})$ and a $\nu(\text{C}-\text{O})$ stretch mode and various $\nu(\text{C}-\text{C})$ stretch and deformation modes which have a transition dipole moment oriented perpendicular to the surface.

Table 6.3: Reference frequencies for aldol intermediates (see figures 6.14 and 6.15).

w: weak, p: mostly parallel to surface, +/-: observed as positive or negative absorbance signal

	$\nu(\text{C}=\text{C})$ [cm ⁻¹]	$\nu(\text{C}-\text{C})$ [cm ⁻¹]	$\nu(\text{C}-\text{O})$ [cm ⁻¹]
methylisopropeneolat	1706	1289	1110
methylisopropeneolat in CCl ₄ ^[184]	1650	1286	1088
isopropenolat on H ₈ Ti ₂ O ₈ cluster perpendicular C=C	1626	1319(p)	1054
isopropenolat on H ₈ Ti ₂ O ₈ cluster parallel C=C	1638(p)	1317	1050
4-hydroxy-4-methylpentane-2-one	$\nu(\text{C}=\text{O})$ [cm ⁻¹]	$\nu(\text{C}-\text{C})$ [cm ⁻¹]	$\nu(\text{C}-\text{O})$ [cm ⁻¹]
sodium adduct	1686	1337 1362 1219	1053
on H ₈ Ti ₂ O ₈ cluster	1703	1316 1243 1129(p)	1037(w) 1043(w)
IRRAS this work	1698(-)	1196(-)	1018(-)

precise to model adsorbate-surface interactions that are determined by the influence of the Ti_{5c} atoms, but fails to describe the interactions with the oxygen atoms at the surface.

6.3 Discussion

The experimental results show that both acetone and benzaldehyde are oxidized to acetate and benzoate, but only acetone forms an intermediate species observed at 1196 cm⁻¹. The identification of the carboxylate products is confirmed by TPRS results (figure 6.5) and IR spectra, the latter spectra being consistent with the presented DFT results (table 6.1). In both cases, the oxidation to the carboxylate requires the surface bound molecular oxygen species, which is responsible for the 410 K signal in TPRS (see figures 6.6 and 6.8).^[185] In contrast, the extra acetone species has been found to form from reaction with O_{ad}.^[185]

6.3.1 Oxidation to the carboxylates

The IR and TPR spectra give strong evidence for a radical oxidation mechanism as suggested in figure 6.3 for the thermal formation of benzoate and

acetate and rule out a nucleophile oxidation mechanism:

In contrast to a radical oxidation (see below), a nucleophile oxidation should be possible with O_{ad} , as they have been reported to react as nucleophiles e.g. on silver(111).^[192] Furthermore, a nucleophile reaction mechanism should show various intermediates, e.g. the acetal intermediate of the Cannizzaro reaction (figures 6.2, 6.13). Such an intermediate was not observed for benzaldehyde, even though DFT results suggest strong vibrational modes orientated perpendicular to the surface for this intermediate (see table 6.2). It should be noted that, if the benzoate was formed in a Cannizzaro-like disproportionation, it would be unlikely that the acetal intermediate was missed, as the following step in the reaction mechanism, the hydride transfer, is known to be the slow, rate limiting step.^[205] Thus, a nucleophile oxidation is very unlikely. For acetone oxidation, the Cannizzaro reaction is not an option either, as it only applies to aldehydes.

Based on the radical character of molecular oxygen and an analogue reaction mechanism in the gasphase, the radical oxidation is the most plausible candidate for the oxidation to the carboxylate species. The adsorbed molecular O_2 species, which is involved in the oxidation, has an unpaired electron and could therefore initiate a radical reaction. The benzaldehyde oxidation experiments, which start from the oxidized surface, indicate the involvement of the molecular oxygen species (see figures 6.6 and 6.8). Free (not absorbed) molecular oxygen exists in the triplet state with two unpaired electrons, which is known to initiate radical reactions. This mechanism has long been established for the auto oxidation of aldehydes in the gas phase (figure 6.3).^[177] As it has been observed that charge is transferred from defects to the oxygen molecule upon adsorption (see section 4.3), presumably one of the unpaired electrons forms a bond to the surface. Thus, as indicated by EPR spectra, the resulting O_2 species adsorbed on the surface still has an unpaired electron.^[151] It is therefore a radical, which can initiate a radical reaction.

The radical oxidation mechanism (figure 6.3) starts by abstraction of the aldehyde hydrogen atom, which leaves an acyl radical and a perhydroxyl species. Acyl radicals have been proposed as being reaction intermediates in the photo oxidation of aldehydes on titania before, but react too quickly in a consecutive reaction to be experimentally detectable.^[151] A similar perhydroxyl species has been reported to form from the reaction of molecular oxygen with bridging hydroxyl groups.^[128,161,200] Considering the low basicity of molecular oxygen, this reaction is possibly due to a radical reaction as well instead of a simple acid base reaction. The acyl radical reacts with the perhydroxyl species to perbenzoic acid, which then decomposes to the benzoate and a terminal hydroxyl

Table 6.4: Overview bond dissociation energies in kJmol^{-1} for the reaction $\text{O}\cdot + \text{R}-(\text{C}=\text{O})-\text{X} \rightarrow \text{O}-\text{X} + \text{R}-(\text{C}=\text{O})$.^[221]

X=H		X=CH ₃	
C–H (methane)	439.3	C–C (ethane)	377.4
O–H (water)	497.1	O–C (methanol)	384.9
total	-57.8		-7.5

group. These hydroxyl groups were reported to recombine and desorb as a water molecule, leaving an O_{ad} on the surface.^[128] A water TPRS signal is indeed observed at this temperature (data not shown), but coincided with the desorption signal of benzaldehyde. Therefore, this observation is questionable to confirm this mechanism. Furthermore, detection of the hydroxyl group using IRRAS was not possible due to the interference from ice layers which grew on the liquid nitrogen cooled detector. However, the formation of a methoxy species during the analogue oxidation of acetone was observed in IR spectra (figure 6.10).

The low observed reaction yield (less than 8%) is explained by the low mobility of adsorbates on the surface. The intermediate reactants are bound to the surface and cannot diffuse freely. Therefore, the radical intermediates formed in the reaction stay in proximity to each other, which in turn favors recombination reactions over radical propagation reactions with other molecules. The dominant recombination limits the reaction rate. Slow reactions for water and oxygen intermediates due to a low mobility of the involved species, such as the diffusion of an O_{ad} into a BOV, have been observed in STM studies at room temperature by Zhang et al.^[202]

The IR spectra suggest that the radical reaction is more favorable for benzaldehyde than for acetone, which can be explained by the different bond dissociation energies. Based on the IR spectra, a small amount of benzoate is observed to form at 200 K, whereas a similar amount of acetate is observed at 250 K. Furthermore, based on the relative signal ratio in the IR spectra, the total amount of acetate formed is roughly one third of the amount of benzoate. This difference is also evident when comparing the signal intensities of the carboxylate with the according carbonyl signals (see figures 6.4 and 6.10). Though quantification of products based on IR spectra is questionable, this observation is consistent with a radical mechanism: The oxidation of acetone involves the homolytic cleavage of a C–C bond and the formation of a new C–O bond. Although the dissociation energy for a C–H bond for an aldehyde is higher than for a C–C bond, this higher activation barrier is compensated by the formation of an O–H bond (see table 6.4). Therefore, the reaction is

in total energetically more favorable for the benzaldehyde oxidation than for the acetone oxidation but acetone oxidation is still possible.

In summary, the radical oxidation mechanism is the most likely candidate to explain the oxidation to the carboxylate species. It is consistent with all experimental results, whereas a nucleophile mechanism is excluded.

6.3.2 Acetone-oxygen intermediate

In addition to the carboxylate signals, the acetone IR spectra show a second reaction intermediate at 1196 cm^{-1} , which was previously not observed. This intermediate is presumably either an acetal or a β -hydroxy ketone.

Henderson proposed based on TPRS, isotopic labeling experiments and HREEL spectra the formation of an acetal, which is responsible for the stabilization effect of acetone by coadsorbed O_{ad} .^[173]³ This acetal was further confirmed by DFT results and proposed based on STM images.^[222,223] The formation of this acetal intermediate was suggested to involve a nucleophile attack at the carbonyl carbon atom.^[223] Ayre et al.^[192] reported such an acetal, which formed from the reaction of acetone with O_{ad} on silver(111).

The acetate is very unlikely a follow up product of a Cannizzaro like reaction. Henderson showed, that different oxygen species are responsible for the formation of the acetate and the acetal.^[185] If the formation of the acetate was a follow up reaction of the acetal, the stabilization effect and the acetate formation would depend on the presence of the same oxygen species. However, acetate formation was observed to depend on molecular oxygen, whereas the intermediate forms on a surface free of molecular oxygen. The latter dependence has been indicated by TPRS results.^[185] Furthermore, the reactions appear to occur independently from each other, as only the benzoate formation is observed for benzaldehyde.

The assumption that the intermediate formed in the reaction of acetone with oxygen is an acetal, is inconsistent with the absence of an analogue benzaldehyde species. The reaction involves switching the hybridization state of the carbonyl carbon atom from sp^2 to sp^3 . This change in hybridization state is energetically less favorable for benzaldehyde as it involves the loss of the resonance stabilization between the carbonyl π -electrons and the phenyl ring. However, this cannot explain the complete absence of the intermediate. Nucleophile reactions are known for benzaldehyde, e.g the benzoin condensation involves a nucleophilic reaction with a cyanide anion.^[176] Furthermore, the DFT results confirm the presence of IR active modes for the benzaldehyde

³Henderson called this intermediate a "diolate".

acetal, which are orientated perpendicular to the surface (see table 6.2).

An alternative candidate for the intermediate species, which is consistent with the absence of a benzaldehyde intermediate, is a β -hydroxy ketone. This ketone is an aldol reaction intermediate. Benzaldehyde cannot undergo an aldol reaction as it does not have any acidic α -hydrogen atoms. Neither the simulated DFT spectra of the isopropenolate nor the β -hydroxy ketone 4-hydroxy-4-methylpentane-2-one (figures 6.14 and 6.15) fit the experimental spectra as well as the acetal. However, especially in the case of the $\nu(\text{C}-\text{C})$ of the β -hydroxy ketone, the computational model might not be sufficiently precise to correctly reproduce the spectra and the orientation of the adsorbate on the surface.

In previous work, Henderson considered an aldol condensation, but only the first intermediate, the isopropenolate and the final reaction product, the enone (in the case of acetone called mesityl oxide).^[185] Based on his HREELS data, Henderson discarded these species as intermediates. However, Henderson's HREELS spectra showed multiple phonon losses at 1515 and 1210 cm^{-1} . Presumably, he therefore did not observe the signal at 1196 cm^{-1} , which is observed in this work, and focused on a signal at 1425 cm^{-1} . This signal is presumably due to the formation of acetate. It is a shoulder of the multiple phonon loss at 1515 cm^{-1} , which could explain why it seemingly disappeared after heating to 400 K, which is also in disagreement with the IR spectra reported herein. Another explanation for the decrease of the acetate signal is the reduction or desorption of acetate by electrons which are used to probe the surface in HREELS. Furthermore, the STM results reported by Yasuo et al.^[223] would have missed the intermediate. The IR spectra (figure 6.10) show that the intermediate is decomposed at 300 K, whereas the STM experiments were conducted at room temperature. Thus, the intermediate presumably was not formed at all. Finally, the DFT results by Márquez et al.^[222] have confirmed that the acetal is stable on the surface, but did not consider any aldol intermediates.

The absence of mesityl oxide, the final aldol condensation product, is plausible, as the final elimination step in the aldol condensation (see figure 6.1) requires a base to abstract one of the central hydrogen atoms. This atom is surrounded by methyl groups and therefore blocked by steric hindrance. Therefore, upon heating, the intermediate decomposes releasing acetone instead of eliminating water. Though aldol condensation products were not observed on rutile(110) single crystals,^[172,185] they were reported on titania nanoparticles and on the oxidized rutile(001) surface.^[179,181,209,210] Furthermore, a H/D exchange which was observed between acetone and coadsorbed D_2O suggests the presence of

the enolate intermediate.^[211] The following reaction of the enolate with a second acetone molecule is presumably fast due to the high mobility of acetone as indicated by the onset of desorption at 200 K in TPRS (figure 6.9).

Further evidence for the importance of α -hydrogen atoms was reported by Zehr et al. for the stabilization effect of oxygen on hexafluoroacetone (HFA) and 1,1,1-trifluoroacetone (TFA).^[224,225] HFA was reported to desorb at 320 K in TPRS from the vacuum annealed surface.^[224] Upon coadsorption of O_{ad} , this desorption signal was shifted to 355 K.^[224] This shift is negligible compared to the shift from 265 K to 360 K which was reported for TFA.^[225] As HFA has no acidic hydrogen atoms, it cannot undergo an aldol condensation. Thus, the stabilization for HFA is possibly due to consumption of excess charge by oxygen as proposed by Plata et al.^[190] (see section 6.2.2) instead of formation of an oxygen adduct. In contrast, TFA has acidic hydrogen atoms and therefore can undergo the aldol condensation, which in turn explains the higher stabilization effect. It should be noted that due to the strong inductive effect of the CF_3 groups in TFA and HFA, a nucleophilic reaction is more likely than for non halogenated carbonyl compounds. Unfortunately, TFA and HFA have shown different photo decomposition mechanisms as non halogenated carbonyl compounds.^[224,225] For one thing, TFA and HFA both decomposed releasing CO, which neither acetone, acetaldehyde nor butanone did.^[172,173,212,224,225] Otherwise, the photochemistry could provide further insights.

Open questions concerning an aldol intermediate are the photo oxidation to acetate and an oxygen exchange mechanism. Previous work by Henderson and Zehr has shown, that the acetone-oxygen and acetaldehyde-oxygen complex are photo oxidized to acetate via methyl ejection.^[172,212] Though a methyl ejection is plausible for the β -hydroxy ketone as well, the consecutive reaction to acetate is not clear. Furthermore, Henderson observed oxygen exchange between acetone and coadsorbed $^{18}O_2$.^[185] Such an exchange supports the acetal intermediate. However, the exchange was indicated by fragment m/z 48 ($D_3C^{18}O$) which could also be due to oxidation e.g. in the mass spectrometer to $C^{18}O_2$.

In summary, based on the reasons discussed above, the β -hydroxy ketone is the more likely candidate for the intermediate. However, further experiments are needed to confirm the findings presented here. First the absence of the benzaldehyde acetal needs to be confirmed: For this further experiments with preadsorbed oxygen and heating to temperature between 200 and 400 K need to be conducted to ensure that the intermediate was not missed because of a poorly chosen temperature. Additionally, an IR study of acetaldehyde could confirm the formation of the intermediate. As acetaldehyde possesses acidic

hydrogen atoms like acetone, a similar intermediate should be observed. Due to the lack of repulsion from methyl groups, the formation of the intermediate for acetaldehyde is expected to be more favorable than in the case of acetone (see section 6.1.3). If no intermediate was observed, the herein reported absence of the analogue benzaldehyde intermediate signal would likely be due to a lack of sensitivity of IRRAS, which in turn would point to the formation of an acetal. An other candidate probe molecule is acetophenone, which can undergo an aldol reaction and is also an aromatic species like benzaldehyde. Further studies could focus on nucleophilic substitution reactions with various oxygen species: For example if O_{ad} were nucleophiles, they would react with halogenated alkanes to the corresponding alcoholates. Thus, if alcoholates were observed, the acetal would become a more plausible candidate. Finally, a more reliable computational model for the β -hydroxy ketone would help with the interpretation of the IR spectra and a mechanistic ab-initio study would provide further insights into the relevance of the various possible reaction pathways.

If the intermediate was an aldol product, the photo decomposition pathway proposed by Henderson would only apply to aldehydes and ketones containing acidic α -hydrogen atoms. The intermediate that forms from reaction of acetone or acetaldehyde with oxygen is the photoactive species for photo oxidation.^[172,212] Illumination of this species induces methyl radical ejection.^[172,212] Zehr and Henderson have demonstrated that the methyl photo desorption yield increases upon annealing oxygen and acetaldehyde on rutile(110) to 200 K and decreases above 300 K.^[172] They concluded from this observation that the photo oxidation depends on the formation of the intermediate, which desorbes or decomposes at 300 K.^[172] The observation of the formation of the acetone-oxygen intermediate in the IR spectra (figure 6.10) at 250 K and desorption or reaction at 300 K suggest that this is the analogue species to the one observed by Zehr and Henderson. If the photo active intermediate is not an acetal but a β -hydroxy ketone, this would suggest, that carbonyl species without α -hydrogen atoms, such as benzaldehyde, were more photo stable than those containing such atoms.

6.4 Conclusion

In summary, the herein presented results give new insights into the interaction of adsorbates with coadsorbed oxygen. Molecular oxygen was shown to oxidize benzaldehyde to benzoate and acetone to acetate. The oxidation mechanism is most likely similar to the radical auto oxidation of aldehydes by molecular

oxygen (figure 6.3).

Besides the radical oxidation, an additional intermediate was observed for acetone, that forms upon heating to 250 K and decomposes at 300 K (figure 6.16).

Presumably, this intermediate is either an acetal or a β -hydroxy ketone:

The formation of an acetal in a nucleophilic reaction from acetone and O_{ad} has been previously proposed by Henderson.^[172,212] This reaction is similar to the first step in the Cannizzaro reaction (figure 6.2). Furthermore, the IR spectra (figure 6.10) in conjunction with the DFT results (table 6.2) obtained for the reaction of acetone presented within this chapter provide strong evidence for the formation of an acetal.

However, the absence of a similar acetal for benzaldehyde points to the formation of the β -hydroxy ketone instead of the acetal. It is formed in an aldol reaction (figure 6.1) which requires an acidic α -hydrogen atom. As benzaldehyde does not possess such an atom, it can not undergo an aldol reaction. The β -hydroxy ketone is also consistent with the experimental data and DFT simulations.

Previously, the formation of the intermediate has been identified as a key step in the photo oxidation of carbonyl compounds e.g. the acetone intermediate is photo oxidized to acetate.^[172,173,212] Thus, the herein presented results suggest a higher photo stability of carbonyl compounds, which lack acidic α hydrogen atoms. Therefore, the herein presented results are of great significance for the photo stability of organic linker molecules on titania, e.g. in Grätzel cells, or for the design of photo catalysts for photo oxidation of pollutants, e.g. in wast water purification.

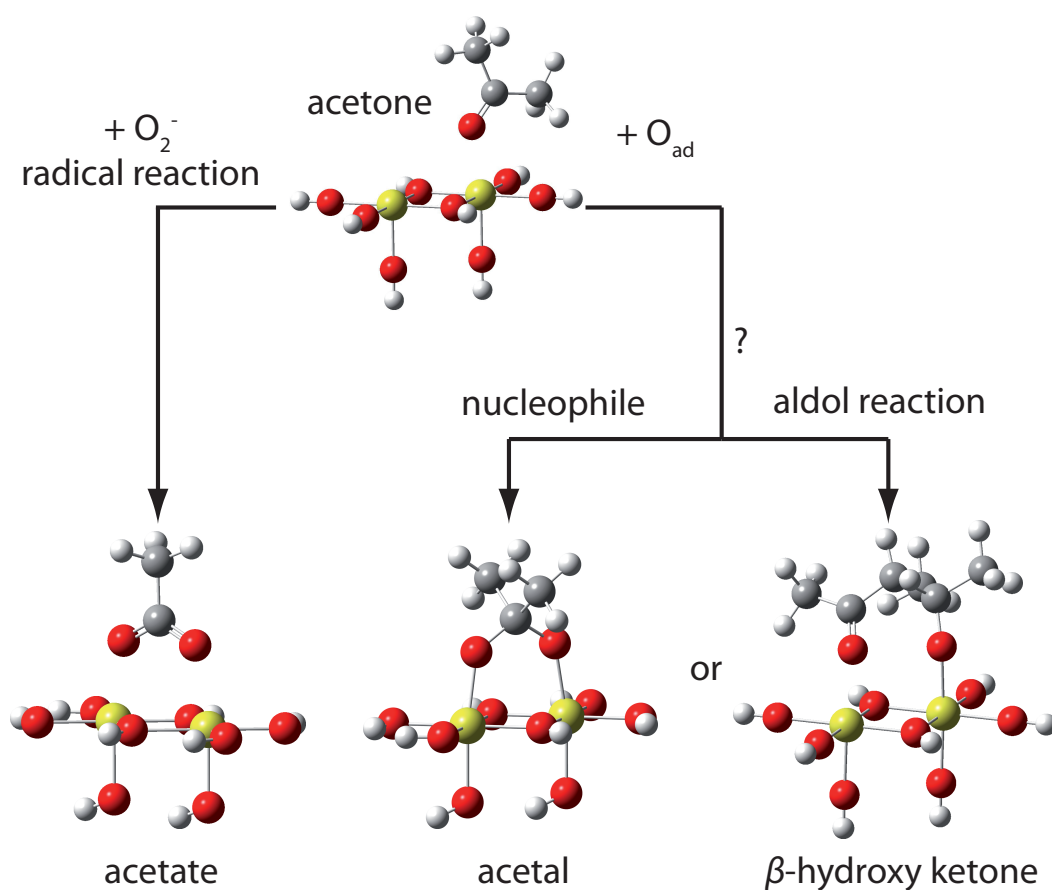


Figure 6.16: Summary acetone oxidation: Acetone reacts with molecular oxygen to form acetate and with oxygen adatoms to an intermediate. This intermediate is either an acetal or a β -hydroxy ketone. For benzaldehyde only the radical oxidation with molecular oxygen to benzoate is observed.

7 Deprotonation, dehydrogenation and disproportionation of alcohols

Besides aldehydes and ketone alcohols are an important class of oxygenates. For example, they are commonly used as solvents in industrial processes.^[8] Methanol is the simplest alcohol and therefore, it is frequently used as a probe molecule to study thermal oxidation and photo oxidation reactions on surfaces.^[126,226,227] Furthermore, natural organic materials, such as carbohydrates, contain hydroxyl groups. Thus, the understanding of chemical reactions e.g. the cracking of organic substances in sediments, which generates crude oils, benefits from knowledge of alcohol surface chemistry.^[4,5] Additionally, methanol plays a key role in chemistry based on natural gas and catalytic CO₂ reduction: For example methanol generated from biogas could be used as liquid fuel for fuel cells.^[228]

Within this chapter the surface chemistry of benzylalcohol is studied using temperature programmed reaction spectroscopy (TPRS), infrared reflection absorption spectroscopy (IRRAS) and density functional theory (DFT). The preliminary results suggest that benzylalcohol dehydrogenates and disproportionates, and that the activation barrier for these reactions is lower than for the analogue methanol reactions, which were reported in the literature.^[126,229] Furthermore, the results presented herein are an important reference for the stilbenediolate which is observed as an intermediate in the reductive coupling of benzaldehyde (see chapter 5).

The results presented in this chapter were a starting point for further work on the surface chemistry of methanol by Milena Osmić and Borchert Jasper.^[92,230] Therefore, additional DFT simulations were conducted to distinguish between deprotonated and molecular alcohol species observed in IR spectra.^[92] Additionally, the DFT calculations showed up differences in the chemical behavior of methanol and benzylalcohol.

7.1 Surface chemistry of alcohols

Methanol is the prototypical alcohol and its surface chemistry on rutile has been studied extensively.^[16,126,227] Methanol was proposed to adsorb molecularly on five coordinated titanium atoms on the reduced and oxidized surface (Ti_{5c} , see figure 7.1 a), and observed to desorb at 295 K in TPR spectra.^[126,208] At higher coverages two additional signals were reported: one signal at 145 K, which was ascribed to desorption of condensed multi layers, and a second signal at 165 K, which was, analogue to previous results for water, ascribed to methanol which binds to bridging oxygen atoms (O_{br} , see figure 4.1 on page 38) via hydrogen bridge bonds.^[126] This observation suggests, that methanol molecules bind more strongly to O_{br} than to each other in a condensed multi layer.

On adsorption, part of the methanol was reported to deprotonate either due to adsorption at defect sites such as bridging oxygen vacancies (BOV) on the reduced surface or upon reaction with coadsorbed oxygen atoms (O_{ad}).^[126,208] Upon adsorption at defect sites the proton was proposed to bind to a neighboring bridging oxygen atom (O_{br} , figure 7.1 c), whereas a reaction with coadsorbed oxygen lead to a terminal hydroxyl group adsorbed at Ti_{5c} (figure 7.1 b).^[126,208] This dissociation¹ leads to methoxy groups adsorbed at Ti_{5c} or BOV, the latter were observed by Zhang et al.^[127] in scanning tunneling microscopy (STM). Part of the dissociated methoxy groups recombine as methanol which was observed in TPRS at 480 K for recombination from Ti_{5c} sites and 540 K for recombination from BOV sites.^[126] Static secondary ion mass spectroscopy (SSIMS) results confirm, that at these high temperature a methoxy species is present at the surface whereas at 295 K molecular methanol was observed.^[126] Besides the dissociation at BOVs, Martinez et al.^[167] observed in STM experiments that e.g. ethanol also dissociates at step edges. Methoxy and methanol could not be distinguished in high resolution electron energy loss (HREEL) spectra,^[126] but IR spectra of methanol adsorbed on rutile nano particles showed several methoxy signals ranging from 1153 cm^{-1} to 1020 cm^{-1} .^[232] In HREELS, the methoxy signal was observed to shift from 1025 cm^{-1} for methanol multi layers to 1050 cm^{-1} after desorption of the multilayers, but no further $\nu(\text{C} - \text{O})$ signals were resolved.^[126] Upon adsorption of methanol on 4 nm rutile particles at 295 K, Panayotov et al.^[232] observed signals at 1153, 1109, 1050 and 1020 cm^{-1} . Based on the DFT results presented herein, these signals are probably due to various molecular and deprotonated methanol species at different adsorption sites with various degree of hydrogen

¹Dissociation for alcohols in this chapter refers to deprotonation.

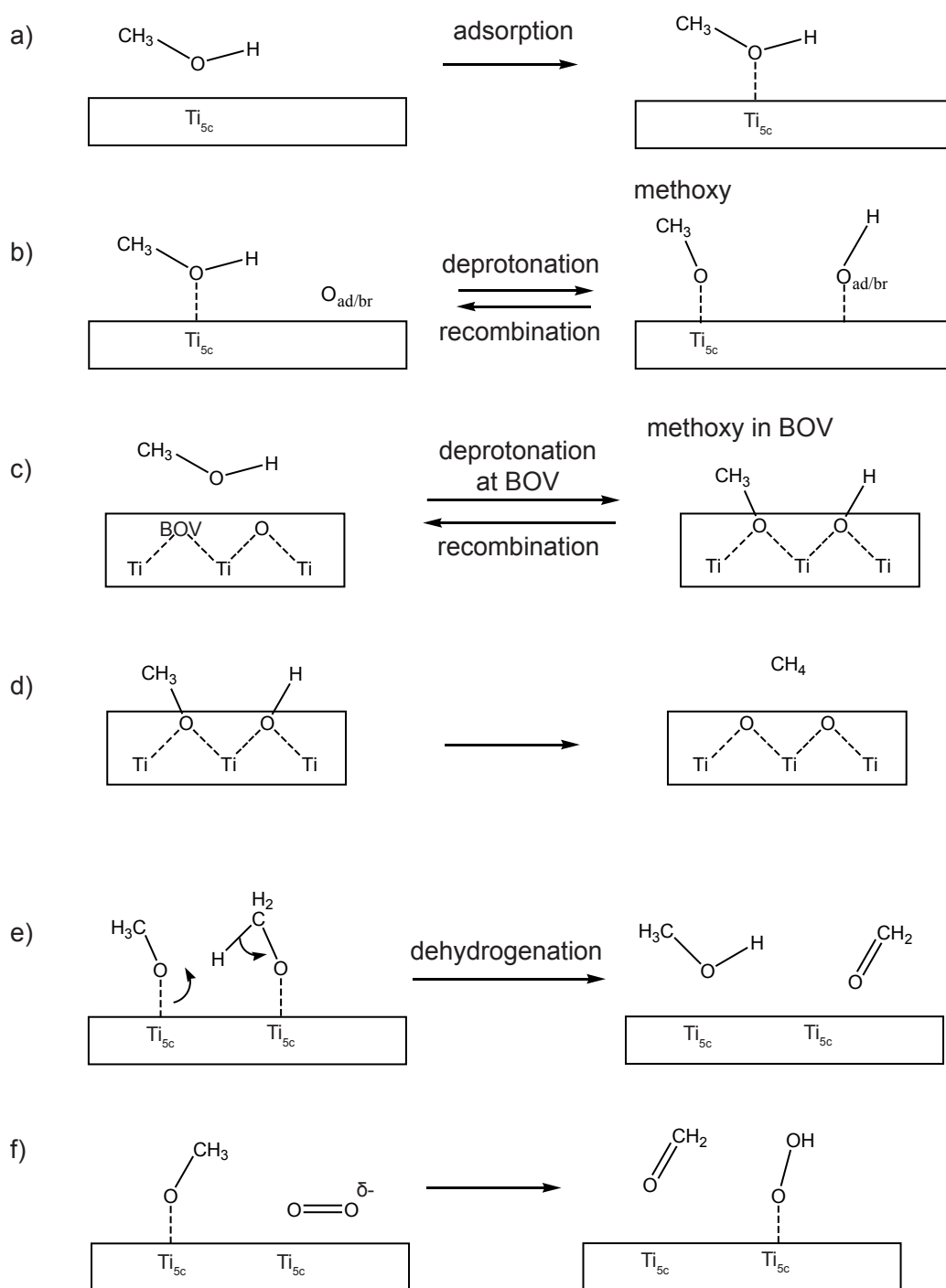


Figure 7.1: Overview of surface reactions which were proposed for methanol on rutile(110):^[126,208,231] a) adsorption at Ti_{5c} , b) deprotonation at coadsorbed oxygen atoms, c) deprotonation in a BOV, d) recombination of methoxy in a BOV to form methane and healing the vacancy, e) dehydrogenation of two methoxy to methanol and formaldehyde, f) oxidation of methoxy (or methanol) with coadsorbed molecular oxygen to formaldehyde.

bridge bonding. Furthermore, Panayotov et al.^[232] observed that methanol adsorption red shifts the adsorption band of coadsorbed CO. They concluded that methanol transfers charge to the surface, which reduces the lewis acidity of the Ti_{5c} atoms and therefore weakens the binding to CO.

DFT results suggested, that dissociation of methanol at Ti_{5c} to methoxy groups at Ti_{5c} and bridging hydroxyl groups, is also possible.^[233,234] Both dissociated and molecular methanol were found to be energetically degenerated and separated by an energy barrier of approximately 1 eV for coverages of 0.25 mono layers (ML) coverages.^[233] For a higher coverage of 1 ML, Zhao et al.^[234] found that molecular adsorption is 0.3 eV more favorable than dissociative adsorption. They concluded, that hydrogen bridge bonds stabilize the adsorbates.

Besides recombination, the methoxy groups adsorbed at Ti_{5c} were observed to dehydrogenate, forming methanol and formaldehyde (figure 7.1 e).^[126,208] This reaction occurred at higher temperature when due to e.g. desorption of water no hydroxyl groups are available for recombination to methanol. Formaldehyde and methanol desorption was observed at 625 K in TPRS.^[126,208] Thus, isolated alkoxy species are thermodynamically very stable on rutile(110).

Additionally, thermo chemical oxidation of methanol to formaldehyde was observed in a reaction with coadsorbed molecular oxygen (figure 7.1 f).^[126] A similar oxidation to formaldehyde was suggested by a molecular oxygen species which adsorbed in the vicinity of gold cluster on rutile(110).^[235] Similar to this reaction an oxidation of benzaldehyde and acetone to benzoate and acetate is discussed in chapter 6

Like methanol, alcohols with longer alkyl chains such as ethanol adsorb both molecularly and dissociatively on titania.^[229,236,237] However, the alkoxy groups react preferentially in a β -hydrogen elimination forming the corresponding alkene compound (figure 7.2) instead of a dehydrogenation to the aldehyde.^[229,236]

Kim et al.^[229] observed two mechanisms: a low temperature mechanism at 300-425 K (figure 7.2 a) and a high temperature pathway around 575 K (figure 7.2 b). The low temperature mechanism was observed not to depend on BOVs, as preadsorbed water did not quench this reaction. In contrast, the high temperature mechanism was observed to depend on BOVs. Therefore, Kim et al.^[229] proposed that the low temperature mechanism is due to the reaction of an alkoxy species adsorbed at Ti_{5c} , whereas the high temperature pathway involves the reaction of an alkoxy species adsorbed in BOVs as illustrated in figure 7.2. The high temperature pathway was observed to benefit from longer alkyl chains, as indicated by a downward shift in desorption temperature. The alkyl chains were proposed to stabilize an intermediate state in the reaction by inductive effects.^[229]

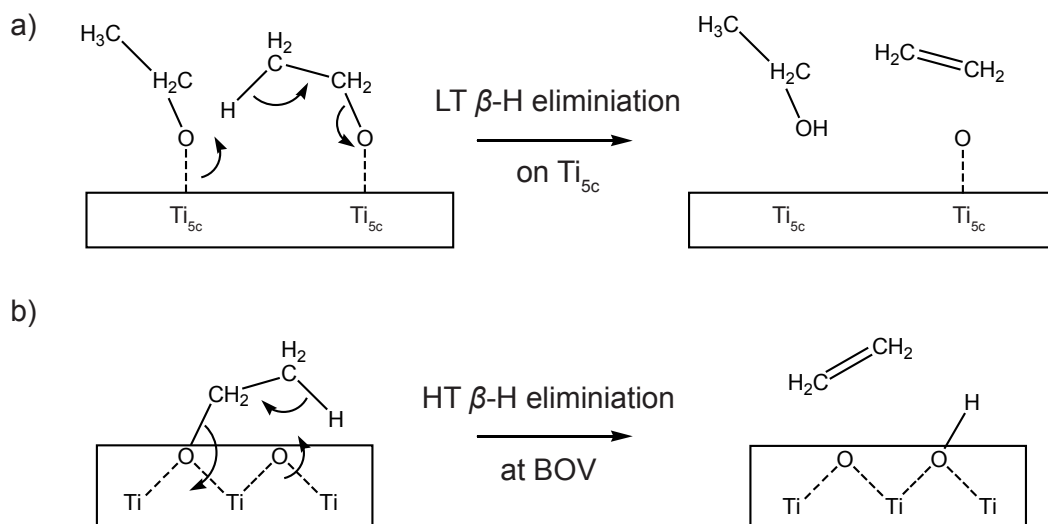


Figure 7.2: β -hydrogen elimination reactions of aliphatic alcohols: In contrast to methanol for aliphatic alcohols such as ethanol, elimination reactions to the corresponding alkene are more favorable compared to the oxidation to the aldehyde / ketone.^[229] a) low temperature elimination from two ethoxys adsorbed at Ti_{5c} , b) high temperature elimination of ethoxy adsorbed in a BOV.

Methanol is photochemically oxidized to formaldehyde.^[231,238] The active species for methanol photochemistry was found to be the deprotonated methoxy species from reaction with O_{ad} .^[231,238] TPR spectra recorded after exposing a surface covered with methoxy to UV light showed desorption signals of formaldehyde and methanol.^[231,238] Methoxy was prepared by coadsorbing oxygen and methanol on the surface and then thermally desorbing methanol by heating to 350 K prior to UV exposure. A multilayer of coadsorbed water was observed to quench the photooxidation.^[231,238] Shen et al.^[231,238] proposed that methoxy is oxidized by a photochemically activated O_{br} which abstracts a hydrogen atom.^[231] This reaction yields a radical ($H_2CO\cdot$) and a bridging hydroxyl group. The radical decomposes to formaldehyde, whereas the bridging hydroxyl group recombines with methoxy to release methanol. A multilayer coverage of coadsorbed water was observed to quench the photooxidation. This water has been found to bind to the O_{br} . Therefore, water was suggested to block the initial abstraction of the hydrogen atom by photoactivated O_{br} .^[231]

Philipps et al.^[116] reported a consecutive photo reaction of formaldehyde with methoxy to methyl formate. The authors proposed that formaldehyde reacts with photoactivated O_{br} yielding a formyl radical ($HCO\cdot$) which in turn reacts with a neighboring methoxy group to methyl formate.^[116,239] The reaction was observed in STM experiments before and after UV exposure and photo

stimulated desorption. Idriss and coworkers^[240,241] observed, that ethanol is photo oxidized to acetaldehyde and acetate in the presence of molecular oxygen (no molecular oxygen was present in the experiments with methanol), but did not report the formation of an ester. Jensen et al.^[239] proposed that the lack of ester is due to a lower reaction enthalpy as indicated by the difference of the C-H bond dissociation energies for ethoxy and acetaldehyde compared to methoxy and formaldehyde. Therefore, the acetyl radical would preferentially react with ethoxy to two acetaldehyde ($\Delta E \approx 4$ kcal/mol), whereas for formaldehyde, where the activation barrier is higher ($\Delta E \approx 8$ kcal/mol), the reaction to methylformate dominates.^[239] This explanation could be tested in a methanol ethanol coadsorption experiment: according to this theory formation of methylacetate should be observed.

Benzylalcohol has been studied for its impact on the stabilization of rutile and anatase nano particles. For example Cooke et al.^[242] observed that benzylalcohol favors the growth of rutile thin films over anatase thin films on carbon nanotubes. Molecular dynamics results suggested, that the phenyl ring of benzylalcohol lies flat on rutile(110) whereas it stands upright on anatase surfaces. As benzylalcohol also lies flat on the carbon nano tubes, binding there via $\pi - \pi$ -stacking, Cooke et al.^[242] suggested that it favors nucleation of rutile seeds.

On Au(111) benzylalcohol was reported to react with oxygen adatoms to yield benzyloxy (benzylalcoholate, $C_6H_5-CH_2-O-Au$).^[243] At low O_{ad} concentrations this intermediate was selectively oxidized to benzaldehyde, and esterification to benzyl benzoate was observed.^[243] Similar reactions were reported for methanol on Au(111).^[226] However, in the presence of excess oxygen, benzylalcohol is oxidized to benzoate and ultimately CO_2 .^[243]

7.2 Results

The surface chemistry of benzylalcohol² was investigated as reference for stilbene diolate, which is an intermediate in the reductive coupling of benzaldehyde discussed in chapter 5. Therefore, the reactions of benzylalcohol were not investigated in great detail in contrast to the work presented in the previous chapters. However, as the work presented herein was a starting point for further work on the surface chemistry of methanol, DFT calculations were conducted to identify signals observed in IRRAS, especially to distinguish between dissociatively and molecularly adsorbed alcohols.

²Special acknowledgements to Verena Böttner and Markus Becker who conducted part of the experiments within a lab class on surface science.

Table 7.1: Relative intensities of key fragments from the NIST fragmentation pattern of benzylalcohol.^[34] Benzaldehyde (m/z 105, 106) and toluene (m/z 92) are not significant fragments for benzylalcohol.

m/z	relative intensity
108	89
107	69
106	2
105	8
92	2

7.2.1 Benzylalcohol results

The experiments in this chapter were conducted on a rutile(110) crystal, which was reduced by 75 preparation cycles. In contrast to other substances used in this work, benzylalcohol has a low vapor pressure (0.027 mbar compared to 1.26 mbar for benzaldehyde)^[244,245] and therefore, was difficult to dose using the pinhole doser. The doser was rigorously purged using benzylalcohol to saturate all metal surfaces and the full vapor pressure of benzylalcohol was used for dosing instead of following the procedure for dosing described in section 3.5. Nonetheless, long exposure times were needed (2 to 5 min) which increased the risk of contamination with oxygen or water and surface coverages in TPRS experiments were difficult to reproduce.

TPR spectra of benzylalcohol (parent ion m/z 108, also m/z 107) recorded at a multilayer coverage (high coverage) and a lower coverage, show desorption signals of benzylalcohol at 445, 350 and 230 K. In analogy to methanol the 350 K signal is tentatively assigned to desorption of benzylalcohol adsorbed at Ti_{5c} , and the 445 K signal to recombination of benzyloxy (benzylalcoholate, $C_6H_5-CH_2-O$). The indefinite growth of the 230 K signal suggests, that this signal is due to multilayer desorption. Assuming that for the high coverage spectrum a multi layer was adsorbed, the intensity of the 350 K signal in this spectrum corresponds to a mono layer coverage of benzylalcohol. Therefore, the intensity ratio of the 350 K signal in the low and high coverage spectra suggests that approximately 0.1 to 0.2 mono layers (ML) of benzylalcohol were adsorbed on the surface for the low coverage spectrum.

All three benzylalcohol signals observed in TPRS are accompanied by benzaldehyde desorption signals (m/z 105, 106) which are most likely due to a reaction and not a contamination of the benzylalcohol. According to the NIST reference spectrum of benzylalcohol (table 7.1), these masses are not due to fragmentation of benzylalcohol.^[34] The presence of benzaldehyde is further indicated by the desorption signal at 170 K in the low coverage and at 190 K in

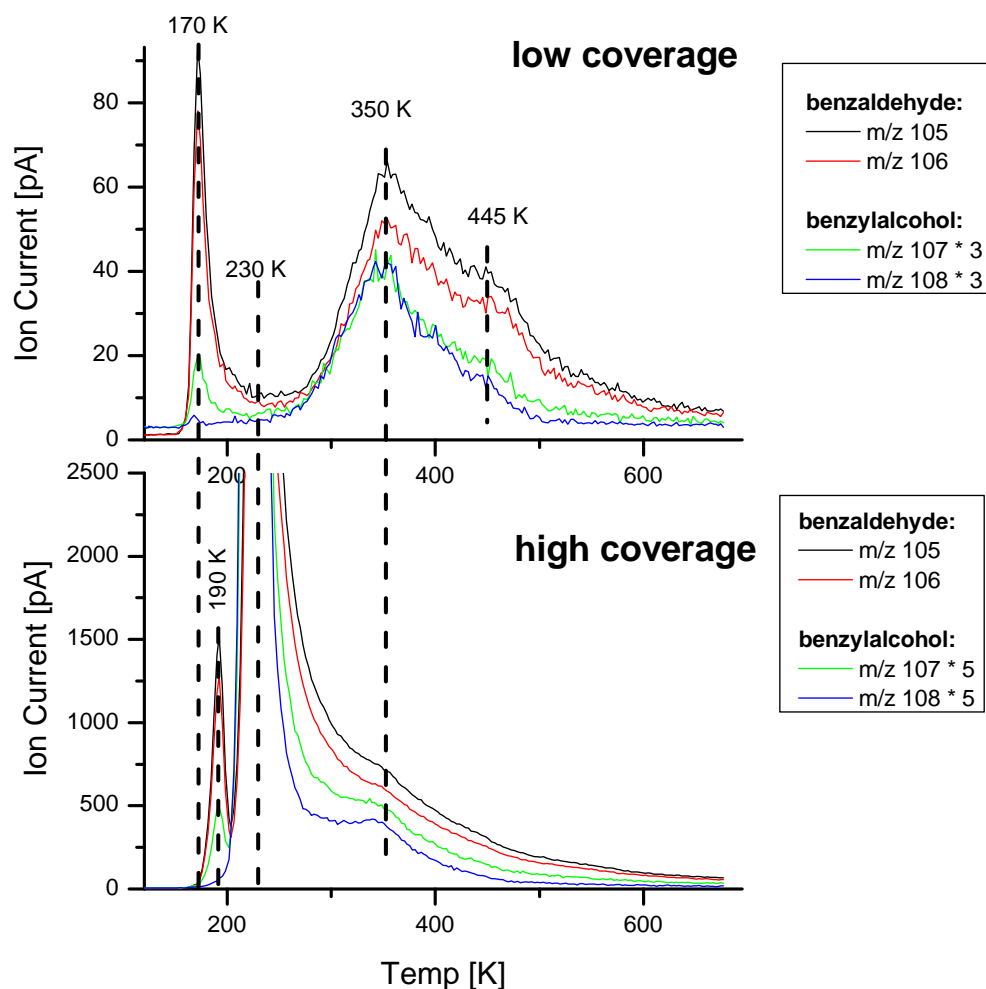


Figure 7.3: TPR spectra of two benzylalcohol (m/z 108, 107) coverages. Based on the signal intensity, the low coverage corresponds to 0.1 to 0.2 ML. Three signals are observed at 445 K and 250 K, which are tentatively attributed to mono layer desorption and 230 K, which is presumably due to multilayer desorption. Remarkably, all signals including the multilayer signal are accompanied by benzaldehyde signals (m/z 105, 106), which is not due to an impurity.

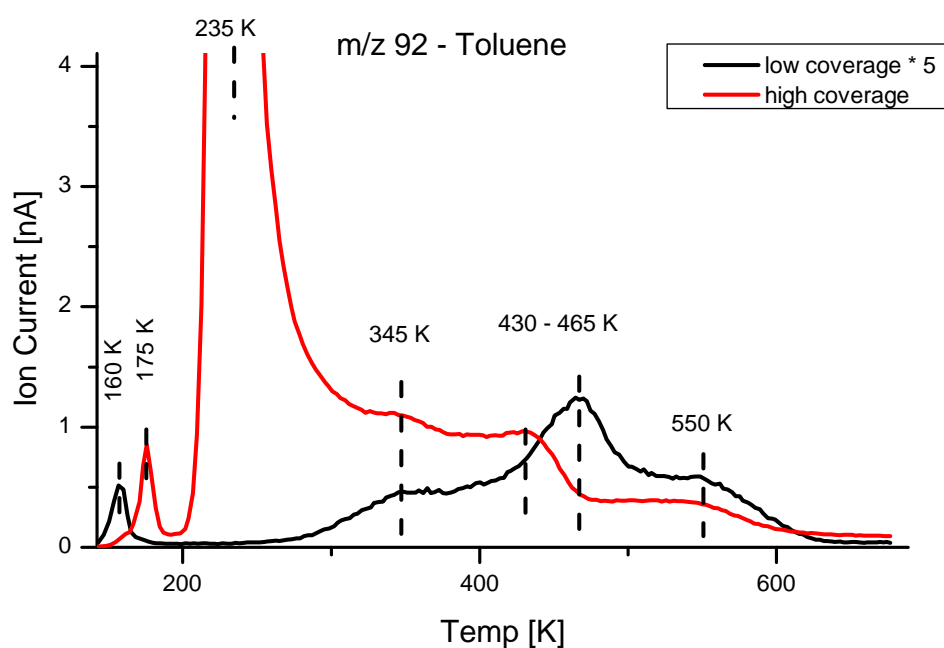


Figure 7.4: Toluene signals observed in benzylalcohol TPRS (m/z 92). Besides codesorption with the benzylalcohol and benzaldehyde signals strong signals are observed around 450 K and 550 K. The 450 K is possibly due to benzyloxy disproportionation (figure 7.11) and the 550 K due to benzyloxy recombination analogue to the reaction for methanol which is illustrated in figure 7.1 d).

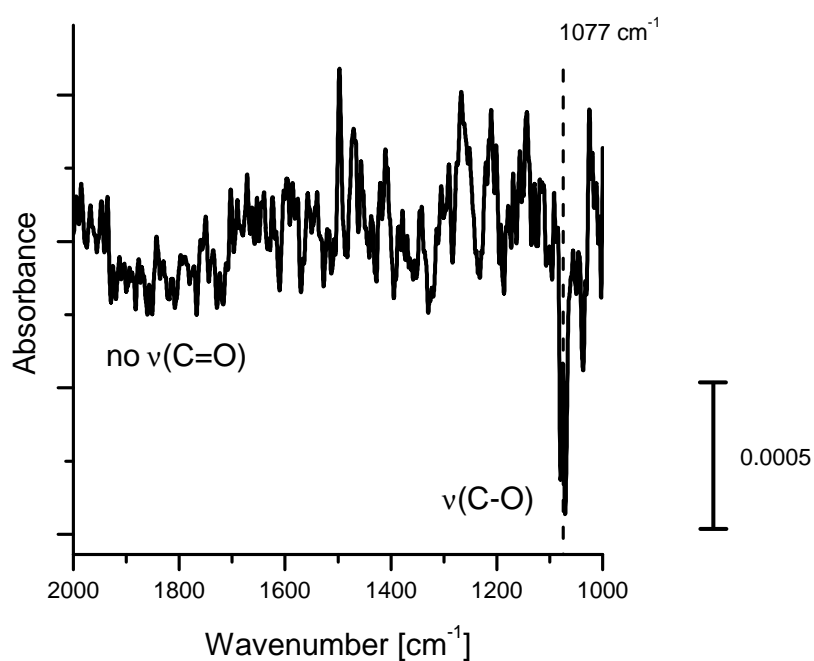


Figure 7.5: IR spectrum of a high coverage of benzylalcohol: The spectrum shows a signal at 1077 cm^{-1} which indicates an alkoxy species. No signals are observed which would indicate a carbonyl species. Therefore, the benzylalcohol is most likely not contaminated with benzaldehyde.

the high coverage spectrum, which is independent of benzylalcohol desorption. These signals indicate the desorption of physisorbed benzaldehyde which previously has been observed in benzaldehyde TPR spectra (figure 5.2 on page 48). Therefore, the m/z 105 and 106 signals are not due to fragmentation of benzylalcohol. Benzaldehyde could be a contamination in the gas lines, which is present from previous experiments. A contamination is strongly supported by the presence of benzaldehyde signals in the multilayer signal at 230 K, as for a condensed multi layer no reactions are expected. However, if benzaldehyde was a contamination, especially to the extent the TPR spectra suggest, it would be indicated by a carbonyl signal in the IR spectrum (figure 7.5). However, such a signal is not observed indicating that no benzaldehyde is present after adsorption at 110 K.

Toluene desorption observed in the TPR spectra (m/z 92, figure 7.4) suggest that benzylalcohol disproportionates. Similar to benzaldehyde and benzylalcohol, toluene desorption is observed at 450 K and 345 K, which coincides with the mono layer desorption signals, and at 235 K which coincides with the multilayer signal of benzylalcohol. However, the signal around 450 K is more pronounced for toluene than for benzylalcohol and benzaldehyde and an additional signal is observed at 550 K. In analogy to the methane evolution observed for methanol (figure 7.1 d), this signal is assigned to recombination of benzyloxy adsorbed in a BOV with a bridging hydroxyl which heals the vacancy. The codesorption of benzaldehyde and toluene indicates a disproportionation reaction of benzylalcohol which appears to be more pronounced for the 450 K signal compared to the 345 K signal. This disproportionation will be discussed in section 7.3.1.

Like benzaldehyde, the observed toluene desorption is most likely not due to a contamination but a reaction. Preliminary TPRS results for toluene (data not shown) indicate that adsorbed toluene desorbs at 250 K. Therefore, the toluene desorption signals above 250 K are most likely due to release of toluene from a reaction instead of desorption of adsorbed toluene.

The IR spectrum of a high coverage of benzylalcohol (figure 7.5) shows an alkoxy signal at 1077 cm^{-1} . The signal is very sharp and slightly blue shifted compared to the SDBS reference spectrum, which shows a broad band at 1016 to 1038 cm^{-1} .^[184] Furthermore, this signal is in good agreement with the observed signal for methanol adsorption at 1050 cm^{-1} .^[92] The DFT results presented below suggest that this signal is possibly due to a molecularly adsorbed benzylalcohol, which forms strong hydrogen bonds to the surface or a multilayer with intermolecular bonds. The spectrum shows no signals, which would indicate the presence of benzaldehyde. Especially, no carbonyl signals in the

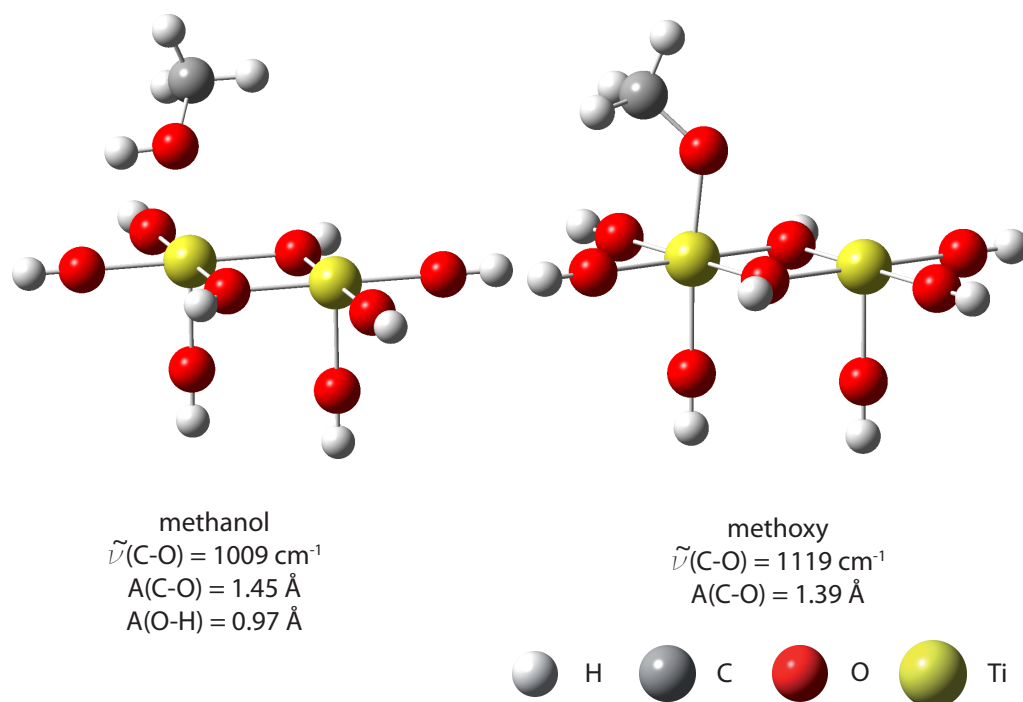


Figure 7.6: DFT results for methanol and methoxy adsorbed on the $\text{H}_8\text{Ti}_2\text{O}_8$ cluster model. Methanol is adsorbed at the Ti_{5c} -atom. For the deprotonated species, the C–O mode is blue shifted and the bond length is shorter than for methanol.

spectral range between 1650 and 1700 cm^{-1} are observed. Previous spectra (see figure 5.4 on page 51) indicate that benzaldehyde should be detectable at the coverages indicated by the TPR spectra even for an alignment of the carbonyl parallel to the surface which is unfavorable for detection in IRRAS.

7.2.2 DFT Results

To distinguish the various alkoxy signals of benzylalcohol which are observed in this work and methanol which have been observed by Milena Osmić, vibrations of methanol and methoxy (figure 7.6) and benzylalcohol and benzyloxy (figure 7.7) were determined as adsorbed on the previously described $\text{H}_8\text{Ti}_2\text{O}_8$ cluster model.^[92]

Both alcohols bind to the Ti_{5c} in the cluster via the oxygen atom and show a strong blue shift of the alkoxy vibration for the deprotonated species. For the adsorbed alcohols, the alkoxy signals is slightly red shifted (see table 7.2) compared to the free alcohol molecules, and the C–O distance is elongated (table 7.3). Upon dissociation, the frequency of the alkoxy signal blue shifts by 110 cm^{-1} for methanol and 204 cm^{-1} for benzylalcohol. Additionally, the

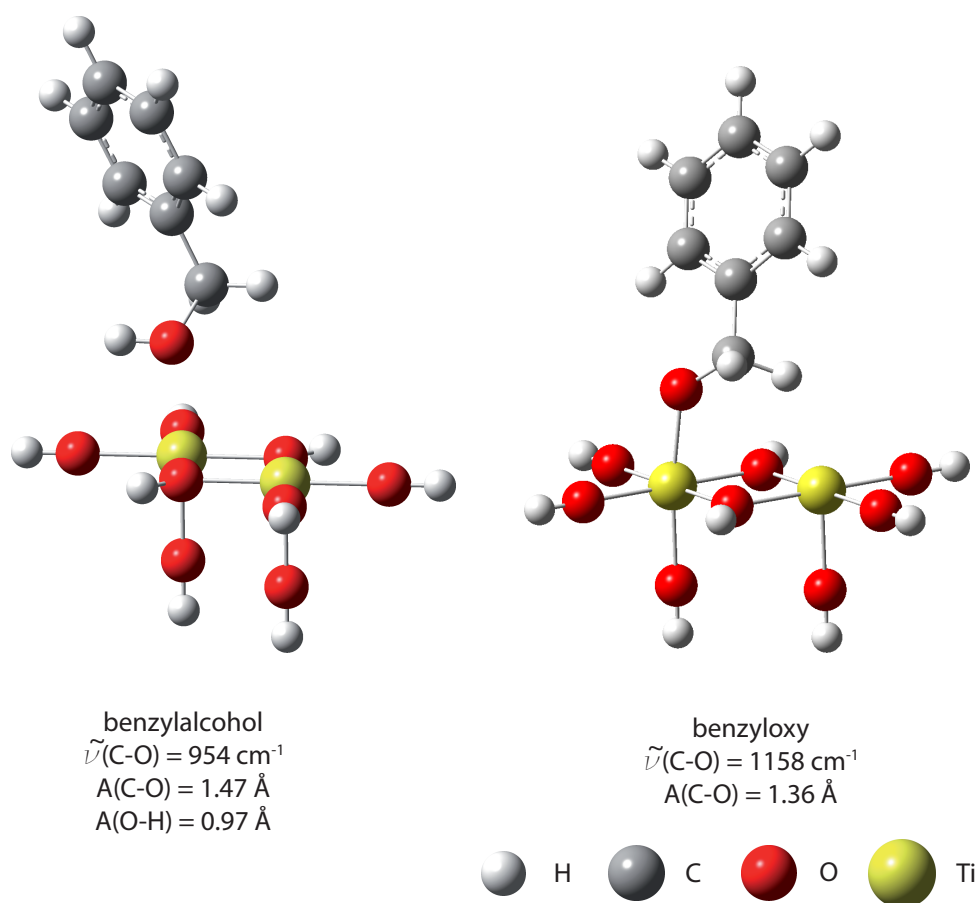


Figure 7.7: DFT results for benzylalcohol and benzyloxy adsorbed on the $\text{H}_8\text{Ti}_2\text{O}_8$ cluster model. The results are similar to the observations for methanol (see figure 7.6).

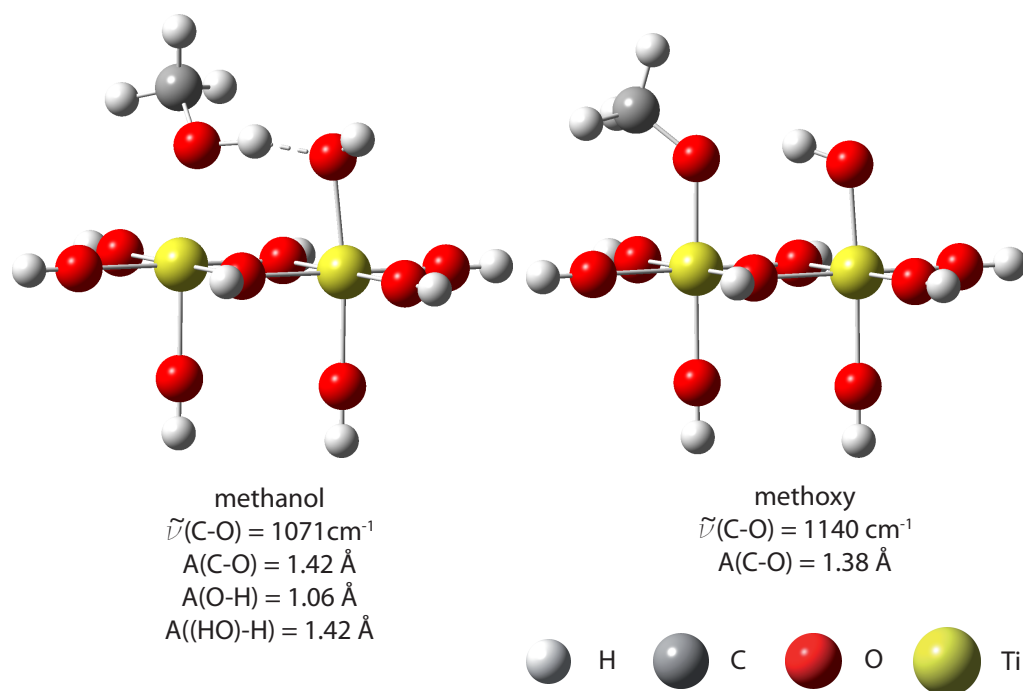


Figure 7.8: DFT results for methanol and methoxy adsorbed on the $\text{H}_8\text{Ti}_2\text{O}_8$ cluster with coadsorbed terminal hydroxyl groups. The hydroxyl group forms a hydrogen bridge bond to the alcohol, which blue shifts the C–O mode to 1071 cm^{-1} . The O–H bondlength is slightly increased from 0.96 \AA to 1.06 \AA , but still significantly shorter than the distance between the proton to the oxygen atom in the hydroxyl group ($A((\text{HO})-\text{H})$). In contrast to methanol, methoxy is barely affected by hydrogen bridge bonds.

C–O bond length is shorter for the alkoxy species, which has been previously found using periodic DFT calculation (see table 7.3).^[233] This observation indicates a strengthening of the C–O bond upon deprotonation.

As Zhao et al.^[234] pointed out, hydrogen bridge bonds play a central role in the stabilization of adsorbed methanol. This is problematic as the used $\text{H}_8\text{Ti}_2\text{O}_8$ cluster does not include the bridging oxygen atoms (O_{br}), which are expected to play a key role in hydrogen bridge bonds. Therefore, as a first approach to study the effect such hydrogen bridge bonds would have on the observed vibrations, the O_{br} are mimicked by adding a hydroxyl group on the used cluster (figures 7.8 for methanol and 7.9 for benzylalcohol). Though this is a simplified model and the absolute results are dubious, this model should suffice to identify the trend hydrogen bridging has on the observed frequencies.

In the presence of coadsorbed hydroxyl groups on the cluster, the alkoxy modes of the alcohols are strongly blue shifted. For methanol, the alkoxy signal is shifted from 1009 cm^{-1} to 1071 cm^{-1} . Furthermore, the O–H stretch mode is red shifted from 3669 cm^{-1} to 2127 cm^{-1} , which indicates a weakening of this

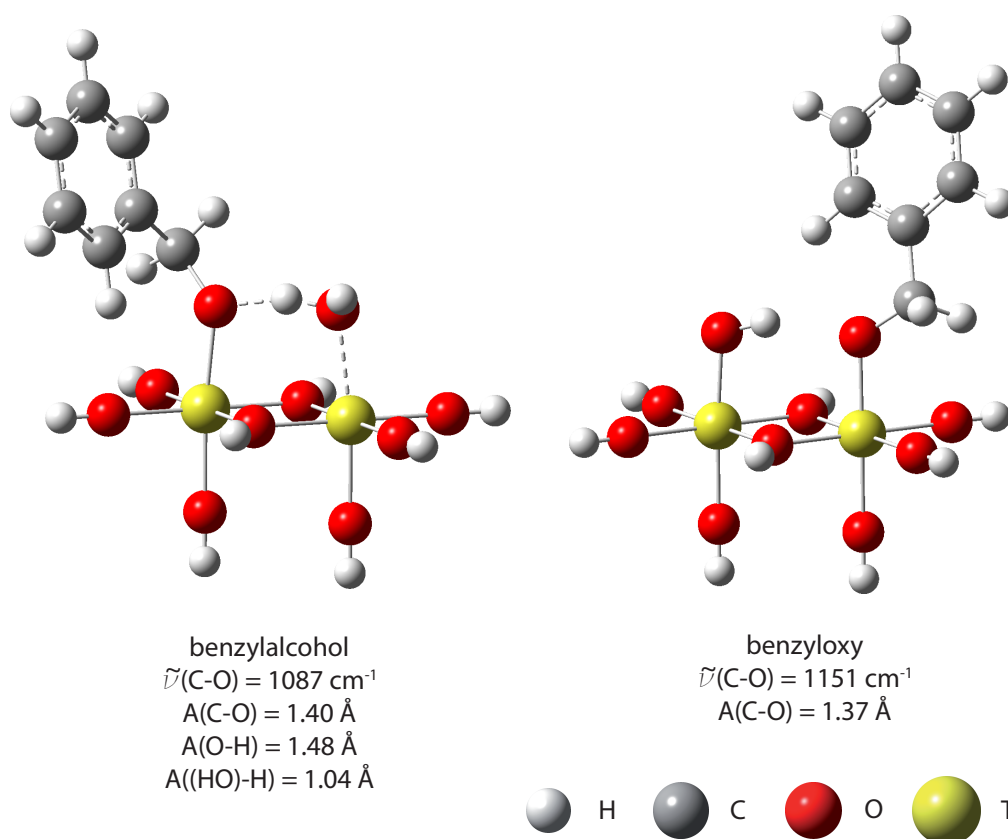


Figure 7.9: DFT results for benzylalcohol and benzyloxy adsorbed on the $\text{H}_8\text{Ti}_2\text{O}_8$ cluster model with coadsorbed terminal hydroxyl groups. In contrast to methanol (figure 7.8), benzylalcohol dissociates, and the alkoxy mode is shifted to 1087 cm^{-1} . The proton is much closer to the hydroxyl oxygen atom than the oxygen atom of the alcohol. Like methoxy, benzyloxy is less affected.

bond. For benzylalcohol, the effect is more pronounced than for methanol. The alkoxy signal shifts from 954 cm^{-1} to 1087 cm^{-1} and the O–H distance is increased from 0.97 to 1.48 \AA , thus benzylalcohol dissociates. In contrast to the adsorbed alcohols, the corresponding alkoxy species are barely affected by the coadsorbed hydroxyl groups: The alkoxy mode blue shifts by 21 cm^{-1} for methoxy and redshifts by 8 cm^{-1} for benzylalcohol upon introducing a hydroxy species (see table 7.2).

The hydroxyl group is a strong base and using it as a model presumably overestimates the effect of the O_{br} . Therefore, for benzylalcohol, the effect of hydrogen bonds to water, hydroxyl and between two benzylalcohol molecules (dimer) was tested in the gasphase using DFT (see tables 7.2 and 7.3). For the dimer the two benzylalcohol molecules are distinguished: one molecule (termed "proton bound") binds via its proton to oxygen atom in the second molecule ("oxygen bound"). The proton of the oxygen bound molecule is faced away from the proton bound molecule. The proton bound molecule is more affected by the hydrogen bond than the oxygen bound molecule, as indicated by the blue shift of the alkoxy mode from 1046 to 1071 cm^{-1} . In contrast, the alkoxy mode of the oxygen bound molecule is redshifted to 1005 cm^{-1} , which is similar to the effect of adsorption on the cluster.

As expected, the effect of the hydroxyl ion is the strongest among the tested candidates and the alcohol deprotonates as indicated by the O–H distance of 1.48 \AA . The effect for the proton bound benzylalcohol is less pronounced, the molecule is not dissociated ($A(O-H) = 0.97\text{ \AA}$) but the bond is weakend, as indicated by the lower wavenumber (3670 cm^{-1} compared to 3855 cm^{-1} for the uncoordinated benzylalcohol). The results indicate, that water binds even weaker as judged based on the shift of the O-H stretch mode (table 7.2).

The results for the benzylalcohol dimer and benzylalcohol coadsorbed on the $H_8Ti_2O_8$ cluster give a lower and upper limit of 26 to 113 cm^{-1} for the expected shift of the alkoxy mode upon hydrogen bridge bonding of benzylalcohol to O_{br} . The herein used model of using coadsorbed hydroxyl likely overestimates the influence of the O_{br} . Upon introducing the hydroxyl, the alkoxy mode shifts by 113 cm^{-1} which is close to the shift upon coordination of benzylalcohol with a free hydroxyl ion (126 cm^{-1}). However, TPRS results suggest that the influence of the O_{br} is stronger than the effect of water or intermolecular hydrogen bridge bonding (26 cm^{-1}). For example, a desorption signal assigned to methanol or water binding to O_{br} observed in TPR spectra indicates, that these molecules bind more strongly to O_{br} than to neighboring molecules in a condensed multi layer.^[53,123,126]

Furthermore, under the experimental reaction conditions, the alcohols might

Table 7.2: Overview of the vibrations for alcohols (see figures 7.6-7.9).
 p: mostly parallel to surface, +/-: observed in IRRAS as positive or negative absorbance signal, n.o.: not observed, w: weak

	$\nu(\text{C-O})$ [cm^{-1}]	$\nu(\text{O-H})$ [cm^{-1}]
Methanol		
free methanol (DFT)	1041	3845
methanol on $\text{H}_8\text{Ti}_2\text{O}_8$ cluster	1009	3669(p)
with coadsorbed hydroxyl	1071	2127(p)
methoxy on $\text{H}_8\text{Ti}_2\text{O}_8$ cluster	1119	
with coadsorbed hydroxyl	1140	
IRRAS on rutile(110): ^[92]		
multilayer adsorbed at 110 K	1052(-)	n.o.
upon heating to 240 K:		
with coadsorbed O_2	1162(-), 1095(-)	n.o.
without coadsorbed O_2	1162(w,-), 1082(-)	n.o.
Benzylalcohol		
free benzylalcohol (DFT)	1046, 1056	3855
with coordinated hydroxyl	1172	2563
with coordinated water molecule	1071	3713
benzylalcohol dimer proton bound	1071	3670
benzylalcohol dimer oxygen bound	1005	3817
benzylalcohol on $\text{H}_8\text{Ti}_2\text{O}_8$ cluster	954	3694(p)
with coadsorbed hydroxyl	1087, 1112	2373(p)
benzyloxy on $\text{H}_8\text{Ti}_2\text{O}_8$ cluster	1158	
with coadsorbed hydroxyl	1151	
IRRAS this work	1077(-)	n.o.

bind to strong bases such as O_{ad} atoms. These atoms are arguably stronger bases than O_{br} as it has been reported that methanol deprotonates more easily in the presence of coadsorbed oxygen.^[126] Therefore, the added hydroxyl groups might be a suitable model for these stronger bases. However, the discussion of various coadsorbates is beyond the scope of this work and limits of the used computational model.

Besides the molecular and dissociated alcohol species other reaction products and intermediates were considered for methanol (figure 7.10): First, methylformate and a methoxy-formaldehyde adduct were considered based on the observed photo oxidation to methylformate by Phillips et al.^[116] For these species, the alkoxy signal is slightly blue shifted compared to that of molecular methanol, but less than for the hydrogen bridge bound methanol and especially the alkoxy mode of adsorbed methoxy. Additionally, these species show a carbonyl stretch mode at 1784 cm^{-1} for methylformate and 1310 cm^{-1} for the adduct, which is close to the reported 1363 cm^{-1} for formate adsorbed on rutile(110).^[47]

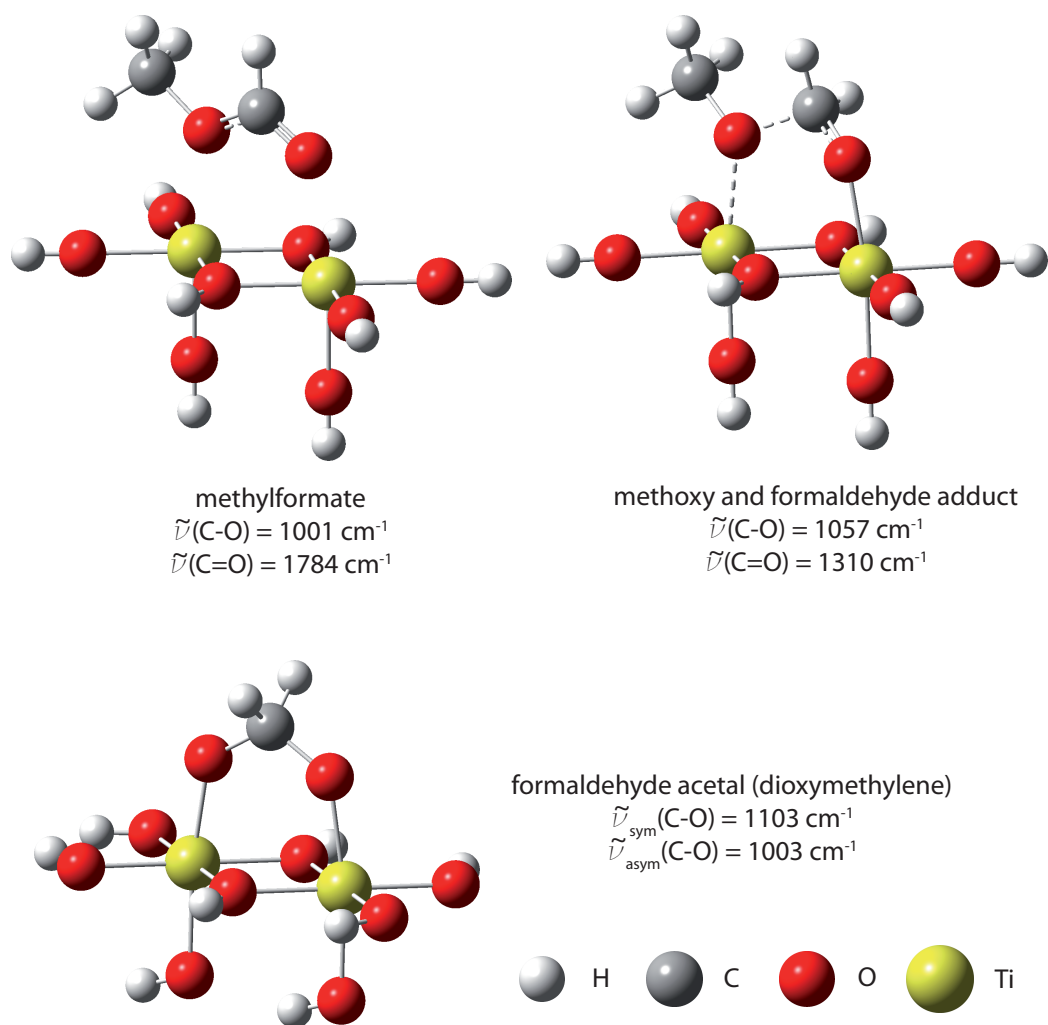


Figure 7.10: Alternative reaction products and intermediates considered for methanol. The methylformate and methoxy-formaldehyde adduct were chosen as they are possible intermediates in the photo oxidation of methanol,^[116] the formaldehyde acetal is based on the experience with acetals in chapter 6. The ester and the adduct are distinguishable from methanol based on the carbonyl modes.

Table 7.3: Overview of the bond lengths for alcohols (see figures 7.6-7.9).

	A(C-O)[Å]	A(O-H)[Å]
Methanol		
methanol	1.42	0.96
on H ₈ Ti ₂ O ₈ cluster	1.45	0.97
on H ₈ Ti ₂ O ₈ cluster with hydroxyl	1.42	1.06
periodic DFT 0.25 ML ^[233]	1.44	1.00
methoxy on H ₈ Ti ₂ O ₈ cluster	1.39	
on H ₈ Ti ₂ O ₈ cluster with hydroxyl	1.38	
periodic DFT 0.25 ML ^[233]	1.40-1.42	
Benzylalcohol		
free benzylalcohol	1.43	0.96
with coordinated water	1.42	0.97
with coordinated hydroxyl	1.35	1.54
benzylalcohol dimer proton bound	1.42	0.97
benzylalcohol dimer oxygen bound	1.44	0.96
benzylalcohol on H ₈ Ti ₂ O ₈ cluster	1.47	0.97
on H ₈ Ti ₂ O ₈ cluster with hydroxyl	1.40	1.48
free benzyloxy	1.33	
benzyloxy on H ₈ Ti ₂ O ₈ cluster	1.36	
on H ₈ Ti ₂ O ₈ cluster with hydroxyl	1.37	

Secondly, the formaldehyde acetal was considered in analogy to the results presented in chapter 6. This species shows a symmetric mode at 1103 cm⁻¹ and an asymmetric mode at 1003 cm⁻¹, which is aligned parallel to the surface. Thus, considering the expected accuracy of the calculation, this species is difficult to distinguish from adsorbed methanol in IR spectra. Therefore, it might be difficult to detect formaldehyde experimentally using IRRAS in the presence of oxygen, as formaldehyde was reported to react with coadsorbed oxygen to this acetal.^[246]

7.3 Discussion

The experimental data for benzylalcohol show an oxidation to benzaldehyde and a reduction to toluene. The IR spectrum confirms, that benzaldehyde forms on the surface and is not a contamination from the gasoline. The oxidation occurs presumably both via dehydrogenation and disproportionation of benzylalcohol. For benzylalcohol the activation barriers are apparently lower than for the analogue methanol reactions. Furthermore, the obtained IR spectrum of benzylalcohol shows an alkoxy signal at 1077 cm⁻¹, which is obtained as a reference for the stilbene diolate discussed in chapter 5.

For methanol, the DFT results allow an identification of the methanol IR sig-

nals which have been observed by Milena Osmić.^[92] In combination, the DFT and IR spectra strongly suggest, that methanol dissociates to methoxy even on the reduced rutile(110) surface. In agreement with previous results,^[126,231] coadsorbed oxygen promotes the dissociation as indicated by a stronger methoxy signal.

7.3.1 Benzylalcohol

The relative intensities of benzaldehyde and toluene observed in the TPR spectra show a different distribution of the reaction products for the signals at 350 and 445 K. The benzaldehyde spectra for the low coverage indicates that less benzaldehyde desorbs at 445 K, but the yield in benzaldehyde relative to the desorption of benzylalcohol is higher. Simultaneously, the toluene signal is more pronounced for the 445 K desorption signal than for the 350 K signal. Therefore, the 350 K desorption signal is due to a reaction that mostly yields benzaldehyde without toluene, such as the dehydrogenation which has been proposed for methanol. On the other hand, this observation suggest that the 445 K signal is mostly due to a reaction that involves the release of the side product toluene, such as the disproportionation.

The dehydrogenation has been previously reported for methanol^[126,208,236] and aliphatic alcohols, though for aliphatic alcohols the β -hydrogen elimination is more favorable.^[229,236] However, due to a lack of β -hydrogen atoms in benzylalcohol, this elimination is not expected for benzylalcohol. For the dehydrogenation of methanol, the reaction mechanism which is illustrated in figure 7.1 e) has been proposed.^[208] Methoxy abstracts an α hydrogen atom from a second methoxy species which react to methanol and formaldehyde respectively.

The desorption of benzaldehyde at 230 K indicates that the activation barrier for the dehydrogenation of benzylalcohol is much lower than for the analogue methanol reaction. Methanol and formaldehyde formation was observed at 630 K.^[208] The DFT results for methanol and benzylalcohol with coadsorbed hydroxyl (figures 7.8 and 7.9) indicate, that benzylalcohol dissociates more easily to benzyloxy than methanol to methoxy. Additionally, for benzylalcohol, the proton transfer is likely favored by resonance stabilization of the intermediate carbanion (not shown in figure 7.1 e) by the phenyl ring. Ultimately, the oxidation of benzylalcohol is thermodynamically favored by the formation of an extended π electron system between the phenyl ring and the carbonyl group in benzaldehyde.

The presence of benzaldehyde in the multilayer signal at 230 K suggest a displacement of benzaldehyde by benzylalcohol from the surface. Benzylalcohol

is neither oxidized in the gas phase nor the liquid phase in the flask. Such a reaction would be indicated by a contamination of benzaldehyde upon adsorption, which is not observed in the IR spectrum. Therefore, benzylalcohol is most likely not oxidized in a multi layer adsorbed on titania at temperatures up to 230 K, too. This assessment is consistent with the proposed mechanism of the reaction mechanism for dehydrogenation, as the initial dissociation of benzylalcohol requires a (weak) base such as the O_{br} . Thus, benzaldehyde is formed at the surface. Based on this assumption, the presence of benzaldehyde in the multilayer indicates the displacement of benzaldehyde from the surface by benzylalcohol. This observation is surprising as TPR spectra of benzaldehyde show that benzaldehyde adsorbed at Ti_{5c} is stable up to 350 K (see figure 5.2). Panayotov et al.^[232] observed a similar effect: coadsorbed methanol weakened the binding of CO on rutile powders as indicated by a red shift of the CO mode in IR spectra. They concluded, that upon adsorption, methanol transfers charge to the surface and, therefore, decreases the lewis acidity of the Ti_{5c} atoms, which in turn weakens the CO adsorption. Thus, the results suggests that benzylalcohol has a similar destabilizing effect on benzaldehyde as methanol has on CO.

The TPR spectra indicate a disproportionation reaction of benzyloxy, which possibly involves an intermolecular hydride transfer. The codesorption of benzaldehyde and toluene indicates a disproportionation of benzylalcohol. At 450 K, the toluene signal in TPRS (figure 7.4) is more pronounced compared to the benzaldehyde signal, than in the 350 K signal, which suggests a higher contribution from disproportionation at 450 K compared to the above mentioned dehydrogenation. Previous SSIMS results on methanol indicated that at temperatures >300 K methanol deprotonates and methoxy is present at the surface.^[126] Thus, in analogy the 450 K signal is most likely due to reaction of benzyloxy and not benzylalcohol. A possible reaction mechanism for toluene formation is a hydride transfer between two adsorbed benzyloxys, similar to the second step described in the Cannizzaro disproportionation for the reaction of aldehydes to the corresponding acid and alcohol (see figure 6.2 on page 70). The hydrid donating benzyloxy is oxidized to benzaldehyde in the process (figure 7.11). The formation of additional benzaldehyde is also observed in the TPR spectrum (figure 7.3): the benzaldehyde signals (m/z 105, 106) at 435 K are more pronounced than the benzylalcohol signals (m/z 107, 108) compared to the desorption signals at 350 K. A similar disproportionation mechanism has been proposed for the reaction of benzylalcohol over zeolites^[247] and alumina.^[248] Similar to the disproportionation, Kim et al.^[229] found C–O bond cleavage as part of an elimination reaction of aliphatic al-

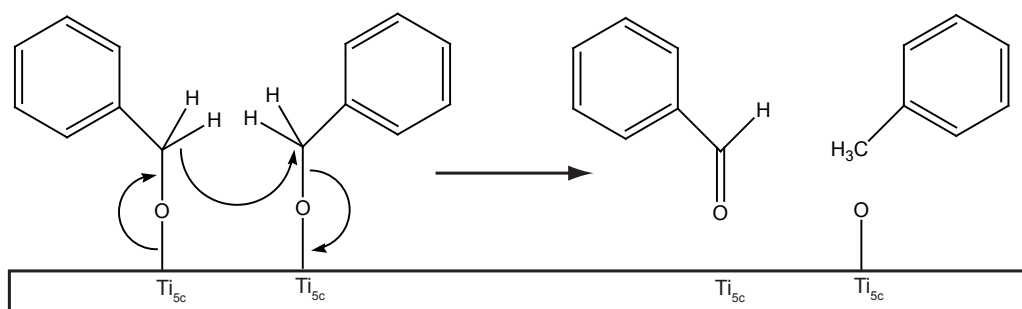


Figure 7.11: Proposed mechanism for toluene formation. The disproportionation of two benzyloxy species possibly occurs via a hydride transfer. The hydride donating species is oxidized to benzaldehyde, whereas the receiving benzyloxy is reduced to toluene.

cohols to the alkene (figure 7.2). However, for benzylalcohol, such elimination reactions are not possible due to the lack of β -hydrogen atoms (see figure 7.2). In contrast to aliphatic alcohols, the oxidation to benzaldehyde benefits from resonance stabilization of an intermediate carbocation and the formation of a conjugated π system between the phenyl ring and the carbonyl group upon oxidation. Presumably, the latter is the thermodynamic driving force for the hydride transfer. This difference to methanol could explain, why the disproportionation is observed whereas for methanol, the abstraction of an α proton (figure 7.1 e) is more likely at 450 K than the hydride transfer.

An open question is the reason for the switching from the dehydrogenation to the disproportionation instead of a complete dehydrogenation of benzyloxy. A possible explanation is the saturation of the surface with hydroxyl groups: The dehydrogenation reaction as indicated in figure 7.1 e) leaves two protons from the initial dissociation step at the surface, which are presumably bound to O_{br} atoms or possibly at sub surface sites.^[249] With progressing of the dehydrogenation, the surface is saturated by hydroxyl groups. This would hinder the formation of benzyloxy by favoring recombination to benzaldehyde and, thus, quench the dehydrogenation. In contrast, the disproportionation as illustrated in figure 7.11 leaves an oxygen adatom at the surface which consumes the protons in a reaction to yield water. Therefore, at a temperature which is high enough to compensate the larger activation energy, the disproportionation predominates.

Admittedly, the herein proposed mechanism is speculative, and not fully supported by the data. As mentioned in the introduction the scope of this work was to obtain a reference for the stilbene diolate intermediate. Especially, the disproportionation mechanism needs further verification. For example, the in-

termolecular hydride transfer could be tested by using isotopic labeling. This way the source of the additional hydrogen atom in toluene could be traced to benzylalcohol or, e.g. coadsorbed water. An other way to test this mechanism is a kinetic study: as the hydride transfer presumably is, analogue to the Cannizzaro reaction, the rate limiting step and a bimolecular reaction step, the disproportionation yield should show a second order reaction kinetic in the concentration of benzyloxy. Furthermore, the quenching of the dehydrogenation could be tested by saturation the O_{br} with one ML of coadsorbed water.

7.3.2 Methanol

The DFT results presented in section 7.2.2 provide a useful guideline to distinguish between various methanol species based on the methoxy frequency ranging from 1009 cm^{-1} for molecularly adsorbed methanol to 1119 cm^{-1} for a dissociated methoxy species. The DFT results further suggested that hydrogen bridges blue shift the alkoxy vibration for methanol and methoxy.

Unpublished IRRAS results by Milena Osmić of methanol adsorbed on a highly reduced (≈ 100 preparation cycles) rutile (110) crystal show a signal at 1052 cm^{-1} for a multilayer coverage of methanol adsorbed at 110 K.^[92] Upon heating the multilayer on the vacuum annealed surface to 240 K, additional signals are observed at 1162 cm^{-1} and 1082 cm^{-1} . Upon heating to 240 K with coadsorbed oxygen, the 1052 cm^{-1} signal disappears and new signals appear at 1162 cm^{-1} and 1095 cm^{-1} . The 1162 cm^{-1} signal is more pronounced when methanol is heated with coadsorbed oxygen. Similar signals were observed in IR spectra of methanol adsorbed on 4 nm rutile particles.^[232]

The DFT and experimental results strongly suggest that the most blue shifted signal at 1162 cm^{-1} is due to a dissociatively adsorbed methoxy species. The DFT calculation indicate that the strongest blue shift is expected for the dissociatively adsorbed methoxy species at 1119 cm^{-1} . The additional shift could be due to further hydrogen bridge bonds. Specifically, the calculation with the coadsorbed hydroxyl group suggest an additional shift to 1140 cm^{-1} . Even without an effect of hydrogen bridging the experimental result is within the expected accuracy of the DFT calculation (see Appendix 2). Furthermore, the increased intensity of this signal in the presence of coadsorbed oxygen compared to the reduced surface confirms this assignment. Coadsorbed oxygen adatoms were reported to deprotonate methanol as indicated by a more intense 640 K observed in TPRS.^[126,231] Additionally, coadsorbed oxygen was reported to heal oxygen vacancies.^[113,129,189] Therefore, the experimental re-

sults with coadsorbed oxygen suggest that this signal is not due to adsorption at BOV sites. Presumably, the density of methoxy adsorbed in BOVs on the surface is too low to be detected in IRRAS. In conclusion, the DFT calculation in combination with the IR spectra strongly suggest, that methanol deprotonates at 240 K. However, it is difficult to judge whether the methoxy signal observed on the vacuum annealed surface is due to dissociation at defects, Ti_{5c} , or due to an accidental coadsorption of oxygen. Oxygen is difficult to distinguish from methanol, as both species are indicated by a signal at m/z 32 in mass spectrometry.

The signals at 1095 and 1082 cm^{-1} are possibly due to methanol which is adsorbed molecularly on the surface. The DFT results suggest that hydrogen bridge bonding blue shifts the alkoxy mode of adsorbed methanol. Previous DFT results pointed out the importance of hydrogen bridge bonds on the adsorption of methanol.^[234] Possible candidates for hydrogen bridge bonds are O_{br} , O_{ad} , terminal hydroxyl groups from dissociation of methanol with O_{ad} , and intermolecular bonds to coadsorbed methanol or methoxy species. The stronger blue shift of this mode compared to the blue shift from intermolecular hydrogen bonds in methanol multi layers is consistent with TPRS results: Methanol bound to O_{br} was reported to desorb 20 K above the multilayer, which indicates a stronger binding of methanol to O_{br} compared to intermolecular binding within the condensed methanol multi layer.^[126]

Future work will focus on the surface chemistry of methanol. One planned project is to investigate the mechanism of photo oxidation of methanol to methylformate, which was proposed by Phillips et al.^[116,230] Another project will use methanol as a probe molecule to assess the surface reactivity of metal particles supported on titania, with a special interest in the interaction of the metal particle with the support.^[92] In some cases thin Ti_2O_x layers were reported to grow on supported metal particles which strongly affected the catalytic properties.^[136] This effect is known as the strong metal support interaction effect (SMSI).^[13]

7.4 Conclusion

In summary, the surface chemistry of benzylalcohol and methanol was studied in this chapter. The experimental data suggest, that benzylalcohol dehydrogenates to benzaldehyde and disproportionates to benzaldehyde and toluene. The dehydrogenation occurs most likely similar to the analogue reaction which has been proposed for methanol (figure 7.1 e). For the disproportionation, an intermolecular hydride transfer is proposed (figure 7.11). The dehydrogenation

is dominant at lower temperatures, whereas the disproportionation is mainly attributed to the 450 K signal in TPRS. This switching in reactivity is proposed to occur due to a saturation of the surface with protons from the initial dissociation step, which are not accounted for in the dehydrogenation mechanism.

The data suggest, that the activation barrier for these reactions is lower than for the analogue reactions of methanol. The reaction products of benzylalcohol are observed at lower temperatures in TPRS than the analogue methanol products. Furthermore, the DFT result indicate that benzylalcohol dissociates more easily to benzyloxy than methanol to methoxy.

Additionally, the benzylalcohol IR spectrum provides a reference for the stilbene diolate, which is an intermediate in the reductive coupling of benzaldehyde (see chapter 5). The spectrum clearly indicates that alkoxy compounds are detectable in IRRAS on titania. Furthermore, the signal of stilbene diolate (1100 cm^{-1}) is further blue shifted than the benzylalcohol reference (1077 cm^{-1}). Based on the DFT results, this shift suggest that the stilbenediolate is an alcoholate and not an alcohol.

The DFT results presented herein suggest that the signals, which were observed in methanol IRRAS experiments,^[92] are due to molecular methanol with various degrees of hydrogen bridge bonding and a methoxy species. The identification of the methoxy species is confirmed by the effect of coadsorbed oxygen, which promotes deprotonation of methanol, and therefore is observed to increase the intensity of the methoxy signal.^[92] This finding suggest, that methanol dissociates on the vacuum annealed rutile (110) surface. In general, the results for methanol demonstrate the advantage of using IRRAS compared to HREELS: In previously reported experiments, the various methanol species could not be distinguished by using HREELS which is accomplished herein.^[126]

8 Summary and Outlook

In summary new insights were gained on the surface chemistry of oxygenates on titania:

The results, which are presented in chapter 5, demonstrate a reduction reaction which involves defects: the reductive coupling of benzaldehyde. The IR spectra strongly suggest the formation of an intermediate, which is, based on previous DFT results, most likely a stilbene diolate. The amount of this diolate is found to scale with the crystals defect density whereas the adsorption of benzaldehyde is not measurably affected. This result indicates that the reaction involves bulk defects. The importance of interstitials is further confirmed by experiments with coadsorbed oxygen: Similar to the reduction of benzaldehyde, oxygen has been found to react with interstitials to form new titania islands on the surface.^[130] In this work, oxygen is observed to quench the formation of the intermediate, which strongly suggest that the interstitials preferentially reacts with oxygen instead of benzaldehyde.

Besides quenching the reductive coupling, oxygen is also found to oxidize coadsorbed carbonyl compounds. Chapter 6 presents results on the oxidation of benzaldehyde and acetone. The IR spectra show that benzaldehyde and acetone are both oxidized by molecularly adsorbed oxygen to benzoate and acetate respectively. However, only for acetone a second species is found which is indicated by a signal at 1196 cm^{-1} in the IR spectra. This species is found to form upon heating acetone with coadsorbed oxygen adatoms to 250 K and to decompose above 300 K. This observation suggests that this species is the photo active acetone-oxygen complex which previously has been described by Henderson.^[185,212] He proposed, that this species is an acetal, though he did not observe a signal in high resolution electron energy loss spectroscopy (HREELS) to support this theory.^[185,213] However, the DFT calculations show that the acetal is consistent with the herein reported IR spectra. Nonetheless, the absence of an analogue benzaldehyde species points at the importance of acidic α hydrogen atoms, which would suggest an aldol like reaction instead of the acetal.

Besides carbonyl compounds the surface chemistry of alcohols is studied in chapter 7 to understand the chemistry of the intermediate in the reductive

coupling. In contrast to methanol, benzylalcohol is found to dehydrogenate at temperatures as low as 230 K. Additionally, the observation of toluene suggests a benzylalcohol disproportionation which is most pronounced at 445 K. Furthermore, the surface chemistry of methanol has been studied using IR spectroscopy by Milena Osmić.^[92] The DFT results presented herein suggest, that the observed signals are due to two species: molecular methanol which binds via hydrogen bridge bonds to coadsorbates and a methoxy species.

This work emphasizes the importance of defects. Defects are either directly involved in the reaction as in the case of the reductive coupling, or play an indirect role as in the activation of oxygen to form the various oxygen species which are discussed in chapter 4. The role of defects is important to understand deviation results between the surface chemistry on the vacuum annealed surface in UHV and studies on systems under ambient conditions: The herein presented results and previous results by Jensen et al.^[139] point out that oxygen reacts with e.g. interstitials consuming them and therefore quenches reactions that rely on the defects as in the case of the reductive coupling. Thus, to transfer reactions observed in UHV to ambient conditions where oxygen is present, an in situ way to produce defects or to mimic their effect is needed, such as heating, reduction with hydrogen or preparation of reduced titania thin films on metal substrates.^[195,250–253]

Furthermore, this work shows up differences in the reactivity of the various oxygen species, that form on the surface. This is another aspect which is important to understand deviations between various studies, as the relative abundances of the oxygen species, such as molecular oxygen or oxygen ad atoms (O_{ad}), depends on several factors such as the sample temperature during exposure to oxygen. Reactions with coadsorbed oxygen are important for the various applications which were motivated in the introduction. For example the photo active species in aldehyde photo oxidation was found to be a reaction product with coadsorbed oxygen. Therefore, the herein suggested role of α hydrogen atoms in this reaction with oxygen has relevance for the design of photo catalysts to oxidize waste products and air purification, or for the choice of more stable linker molecules in dye sensitized solar cells.

Infrared reflection absorption spectroscopy (IRRAS) has been proven to be a valuable complementary technique to thermal desorption and scanning tunneling microscopy. In this work, IRRAS was used to identify the stilbene diolate intermediate in the reductive coupling of benzaldehyde and to study the impact of the bulk defect density on this intermediate. Using IRRAS, the oxidation of benzaldehyde to benzoate is observed which is difficult to observe in TPRS because benzoate does not desorb intact, but decomposes. Furthermore, for

the first time IRRAS provides a direct experimental evidence for the formation of the acetone-oxygen complex which is discussed in chapter 6. Additionally, the various methoxy signals for molecular and dissociative methanol adsorption were resolved in IR spectra.^[92] The main advantage of IRRAS compared to HREELS on titania is that it is not sensitive for the bulk phonon modes which are interfering and difficult to remove from HREEL spectra. Presumably, Henderson did not observe the acetone oxygen complex signal due to the phonon modes and instead focused on a signal which is, based on the evidence reported in chapter 6, most likely due to acetate formation.^[185] Additionally, the various methoxy signals for methanol adsorption were not resolved in previous HREEL spectra.^[126] The implementation of IRRAS for this work was challenging, most difficulties arose from the low signal intensities which required long measuring times. Therefore, one difficulty was to ensure a long time stability of the experiment over several hours compared to a few minutes for experiments on metal surfaces.

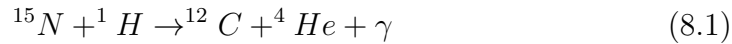
The density functional theory (DFT) results from the $\text{H}_8\text{Ti}_2\text{O}_8$ cluster model have been proven to be a most useful tool to interpret the obtained IR spectra. The main benefit of using these DFT results compared to reference spectra from databases is the identification of the vibrational modes and their alignment with respect to the surface which is crucial information to interpret the spectra based on the surface selection rules for IRRAS. Furthermore, some trends are to be studied such as the effect of hydrogen bridge bonds have on the adsorption of methanol. This model has been proven to be sufficiently accurate for most cases within this work. However, it is limited to such cases where the adsorbate binds to the five fold coordinate titanium atoms (Ti_{5c}). Furthermore, this model cannot reproduce the effect of bridging oxygen atoms (O_{br}) or defects, and is too small to obtain meaningful results on the interaction of coadsorbates. Therefore, these DFT results have to be interpreted carefully. More reliable results could be obtained by increasing the cluster size or using periodic methods, however this was beyond the scope of this work.

Outlook

Especially, the effect of the bulk on surface reactions is an open question which is not easily addressed with surface science techniques. This work showed that bulk defects play a major role, but the exact quantification of these defects is difficult. Besides defects, the bulk may play a role by absorbing reactants: for example Enevoldsen et al.^[249] observed sub surface hydrogen atoms in titania. One project that was started within this work is to study the intercalation

8 Summary and Outlook

of hydrogen into the bulk and the impact of defects thereon. To this end nuclear reaction analysis (NRA) experiments were conducted to quantify the concentration of hydrogen in the bulk in cooperation with Franziska Träger.^[254] This technique is based on the nuclear reaction



which occurs in resonance at 6.385 ± 0.005 MeV.^[255] By detecting the γ rays, which are emitted by this reaction, the amount of hydrogen is quantified. Furthermore, as the reaction occurs in resonance at 6.385 MeV, a depth profile is obtained by changing the initial energy of the ^{15}N beam. The primary beam loses energy in inelastic scattering processes upon propagating through the material. Therefore, the higher the primary energy is the deeper the beam penetrates until it reaches the resonance energy. Unfortunately, due to difficulties in quantification of the bulk defects, this project is currently postponed. For preliminary results see appendix 3.

Going back to Langmuir the next step within the surface chemistry approach is to increase the complexity of the system. As motivated in the introduction one interesting aspect in heterogeneous catalysis is the strong metal support interaction (SMSI). To study this effect, the herein gained insights are applied to more complex model systems, such as colloidal nano particles supported on titania which is the subject of the PhD thesis by Milena Osmić.^[92] Another approach to study the SMSI effect is working with titania thin film on metal supports: Previously, Goodman and coworkers studied titania thin films on molybdenum single crystals with gold nano particles on top.^[195,250–252] Additionally, Wu et al.^[253] characterized titania ultra thin films on gold. Both metal nano particles on titania, and thin films on metals are interesting candidates to study cooperative material effects. Other inviting next steps are comparing the herein gained findings to other reducible chalcogenides such as tungsten oxide, molybdenum sulfide,^[256,257] magnetite^[258] or various titanates to gain a broader understanding on the surface chemistry of dielectric materials or to apply the results to better understand photo chemical reactions like the aforementioned photo oxidation of aldehydes.^[172,213]

Appendix

1 Cluster Model

As discussed in section 6.2.3 DFT calculation were conducted using a $\text{H}_8\text{Ti}_2\text{O}_8$ cluster model. The coordinates of the atoms within the cluster model were taken from previous DFT results by Jan Haubrich (see figure 5.1).^[100]

Table 1: Cluster Coordinates used for Gaussian09

Ti	6.34627225	3.66470248	-0.02075718
Ti	3.43711716	4.23412259	0.04090617
O	1.73583634	3.29055540	-0.22491012
O	7.55414654	2.15171518	-0.34823682
O	4.64499144	2.72113529	-0.28657347
O	2.22924288	5.74710988	0.36838581
O	8.04755307	4.60826967	0.24505911
O	5.13839797	5.17768977	0.30672246
O	6.29730096	3.20314359	1.93106358
O	3.38814586	3.77256370	1.99272693
H	8.87934796	5.06960113	0.37502274
H	5.32235474	6.09356702	0.52792099
H	1.63868567	6.48684379	0.52849806
H	0.90404146	2.82922393	-0.35487375
H	4.46103468	1.80525805	-0.50777200
H	8.14470375	1.41198128	-0.50834906
H	3.36471287	3.55170562	2.92668228
H	6.27386796	2.98228551	2.86501893

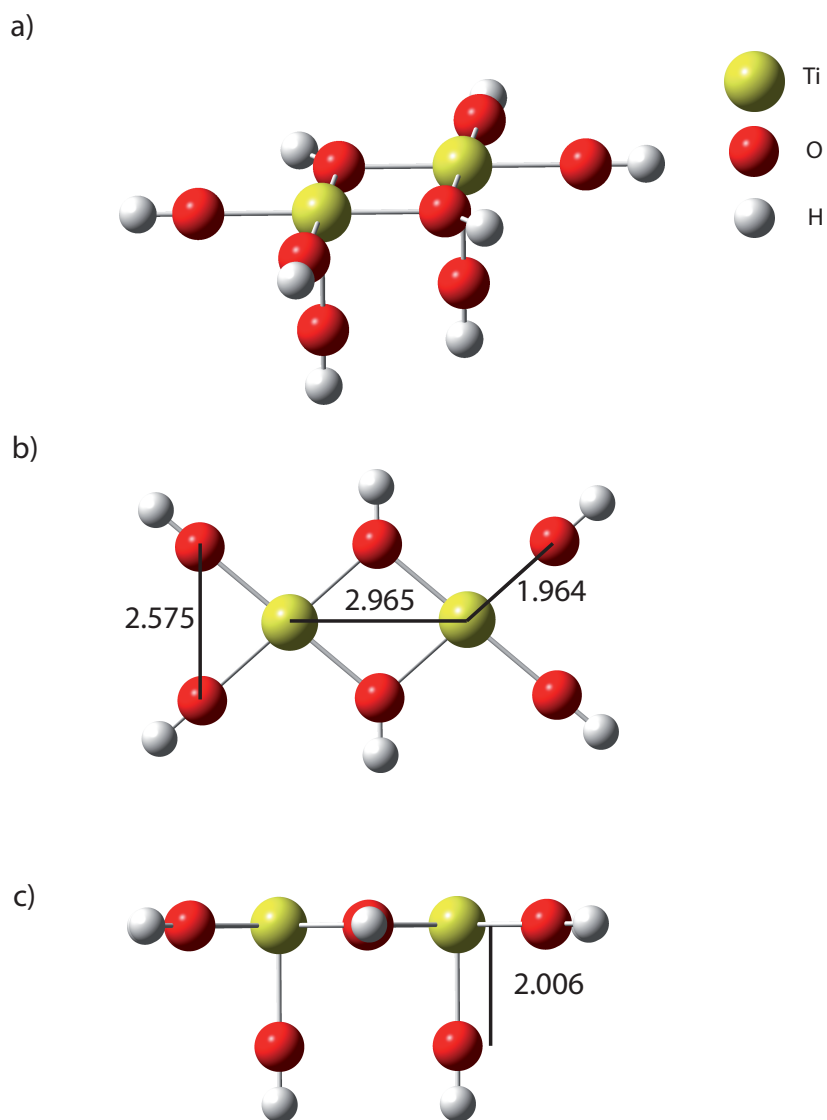


Figure 1: The $\text{H}_8\text{Ti}_2\text{O}_8$ cluster model used for DFT calculations:^[100] a) isomeric view, b) top view, c) side view. Distances are given in Å.

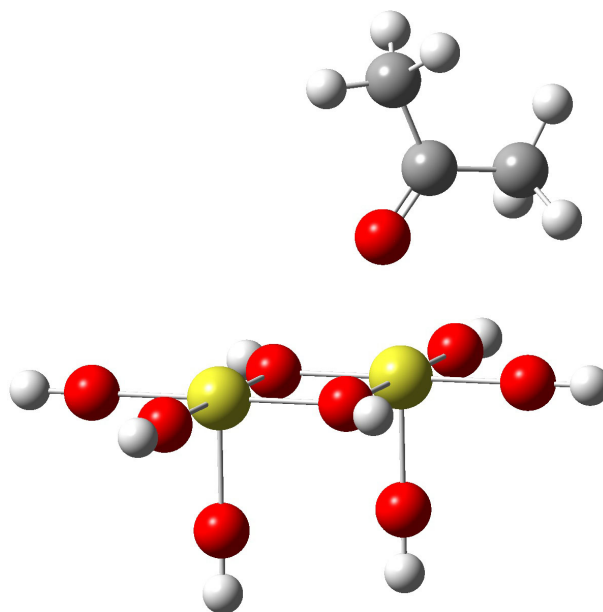


Figure 2: Acetone adsorbed on the $H_8Ti_2O_8$ cluster .

2 DFT functionals and basis sets

To access the reliability of the obtained DFT results, different DFT functionals and a smaller 6-31+G(d,p) basis set were tested for some of the structures used within this work. Besides the B3LYP functional, which is used primarily within this work, the PBE0 functional was tested. It is a parameter free hybrid functional proposed by Adamo and Barone^[259] and an extension of the original gradient corrected functional proposed by Perdew, Burke and Ernzerhof.^[260] As this functional depends less on empirically found parameters, it was proposed that this functional is more generally applicable than parametrized functionals, which are optimized for certain chemical compound classes.

The calculations were done using the Gaussian09 software packet. The species are adsorbed on the $H_8Ti_2O_8$ cluster model described in appendix 1. The PBE0 functional was used as implemented by using the pbe1pbe keyword.^[217] The chosen test candidates are:

- an acetone acetal (see figure 6.12 on page 86)
- benzoate (see figure 6.11 on page 84)
- acetone (figure 2)
- methanol and
- deprotonated methoxy (see figure 7.6 on page 112)

In general, the results for PBE0 and B3LYP (table 2) are in good agreement with each other and deviate by less than 50 cm^{-1} or by 30 cm^{-1} in average.

Appendix

The influence of the basis set is even lower: For calculations using the same functional, the frequencies shift by less than 15 cm^{-1} or 8 cm^{-1} in average when the basis set size is increased from 6-31+G(d,p) to 6-311+G(d,p).

For benzoate, the $\nu_{\text{asym}}(\text{OCO})$ is poorly reproduced by both, the PBE0 and the B3LYP functional. Therefore, the M06 functional was tested additionally. M06 was reported to reproduce organometallic thermal chemistry and non-covalent interactions better than the aforementioned functionals.^[261] However, in this case, the results obtained using the M06 functional are similar to the PBE0 results. Therefore, this functional is not further considered in this work. The results show that in most cases, the vibrations obtained using PBE0 deviate systematically to a higher wavenumbers compared to the B3LYP results. As discussed in section 6.2.3 DFT methods typically overestimate vibrations and are scaled by empirical factors. For PBE0/6-311+G(d,p) a scaling factor of 0.9601 was reported (0.9540 for PBE0/6-31+G(d))^[262] which is slightly lower compared to a factor of 0.964 for B3LYP/6-31++G(d,p).^[218,219] These scaling factors were obtained by testing a variety of small molecules.^[262] Thus, the tendency of PBE0 to overestimate vibrations more than B3LYP is consistent with the observations for the molecules, which were used to determine the scaling factors.

The results for benzoate and acetone indicate that the scaling factors do not apply in general to the herein investigated adsorbate system. The unscaled vibrations for the $\nu_{\text{sym}}(\text{OCO})$ mode for benzoate and the $\nu(\text{C=O})$ mode for acetone are in excellent agreement with the experimental result. Thus, for these modes, no scaling factor is needed. However, the $\nu_{\text{asym}}(\text{OCO})$ mode suggest a much stronger deviation from the computed results than indicated by the scaling factors. As this discrepancy is reproduced with three different functionals it is more likely due to the limitations of the cluster model used herein as discussed in section 6.2.3.

In summary, the deviations between the two functionals are negligible for the examined test cases compared to the expected deviations based on the limited representation of the rutile(110) surface by the used $\text{H}_8\text{Ti}_2\text{O}_8$ cluster model. The B3LYP functional in combination with the 6-311+g(d,p) basis set appears to be sufficiently reliable for the purpose of this work.

Table 2: Vibration results for B3LYP and PBE0 (and M06) using 6-31+G(d,p) and 6-311+G(d,p) basis sets.

Acetone acetal	$\delta_{\text{sym}}(\text{CCC})$	$\nu_{\text{sym}}(\text{OCO})$	
PBE0 6-31+G(d,p)	1217	1018	
PBE0 6-311+G(d,p)	1211	1015	
B3LYP 6-31+G(d,p)	1194	1002	
B3LYP 6-311+G(d,p)	1188	997	
(Exp) ¹	(1196)	(1018)	
Benzoat	$\nu_{\text{sym}}(\text{OCO})$	$\nu_{\text{asym}}(\text{OCO})$	
PBE0 6-31+G(d,p)	1467	1636	
PBE0 6-311+G(d,p)	1457	1625	
B3LYP 6-31+G(d,p)	1434	1593	
B3LYP 6-311+G(d,p)	1421	1579	
M06 6-311+G(d,p)	1454	1656 ²	
Exp	1420	1479	
Acetone	$\nu(\text{C=O})$		
PBE0 6-31+G(d,p)	1745		
PBE0 6-311+G(d,p)	1737		
B3LYP 6-31+G(d,p)	1711		
B3LYP 6-311+G(d,p)	1706		
Exp	1698		
Methanol	$\nu(\text{C-O})$	$\delta(\text{OH})$	$\nu(\text{O-H})$
PBE0 6-31+G(d,p)	1061	1362	3624
PBE0 6-311+G(d,p)	1054	1364	3667
B3LYP 6-31+G(d,p)	1016	1358	3633
B3LYP 6-311+G(d,p)	1009	1363	3669
Methoxy	$\nu(\text{C-O})$		
PBE0 6-31+G(d,p)	1162, 1179 ³		
PBE0 6-311+G(d,p)	1156, 1173 ³		
B3LYP 6-31+G(d,p)	1127		
B3LYP 6-311+G(d,p)	1119		

¹ The observed mode is not unambiguously assigned to an acetal.² Two modes are observed due to coupling with phenyl ring modes. The stronger mode is listed.³ Two modes are observed due to coupling with the $\rho(\text{CH}_3)$ mode.

3 Preliminary NRA results

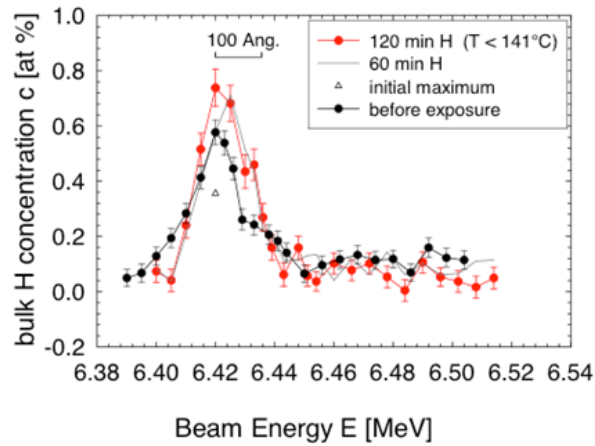


Figure 3: Preliminary NRA results of a slightly reduced crystals (20 preparation cycles) before and after exposure to atomic hydrogen. Increasing the primary beam energy increases the penetration depth in the material. The observed peak is most likely due to water adsorbed at the surface. Spectra provided by Franziska Träger.^[254]

Curriculum vitae

Personal Information

Name	Peter Michael Clawin
date of birth	28.3.1984
place of birth	Münster
citizenship	German
Address	Carl von Ossietzky Str. 3b, 26129 Oldenburg, Germany
Tel.	+49 441-798 3598
e-mail	Peter.Clawin@uni-oldenburg.de

Education

since 2009	PhD candidate , Prof. Katharina Al-Shamery, Carl von Ossietzky University of Oldenburg
2009-2010	visiting PhD student, Prof. Cynthia Friend, Harvard University, Department of Chemistry and Chemical Biology
2008	Diploma , Chemistry, Carl von Ossietzky University of Oldenburg Major courses in physical and inorganic chemistry, chemical engineering and computer science Thesis: "Ultrakurzpuls-Laser unterstützte Untersuchungen an Goldnanopartikeln und deren Präparation" ("Ultra fast Laser pulses aided characterisation of gold nano structures and their preparation")
2005	Vordiplom, Carl von Ossietzky University of Oldenburg
2003	Abitur, Gymnasium Bad Iburg
2001	student exchange: Roncalli High School, Manitowoc, WI, USA
2000	student exchange: Lycée François 1 ^{er} , Le Havre, France

Fellowships and Awards

2009-2012	Fellowship, Fond of the Chemical Industry (FCI) Germany
2009-2010	Fellowship, German Academic Exchange Service (DAAD)
2005	award for best Vordiplom

Publications

Part of this work has been presented at conferences and published in peer reviewed journals:

Publications

- Peter Clawin, Cynthia Friend, Katharina Al-Shamery: *Defects in Surface Chemistry-Reductive coupling of Benzaldehyde on Rutile(110)* Chemistry: A European Journal, **2014**, *90*, 7665-7669
- Peter Clawin, Cynthia Friend, Katharina Al-Shamery: *Nucleophilic versus radicalic reactions of oxygen species on rutile TiO₂(110)* (paper in preparation)
- Peter Clawin, Milena Osmić, Rainer Koch, Cynthia Friend, Katharina Al-Shamery: *Molecular and dissociative adsorption of methanol on titana: the advantage of using IRRAS*. (paper in preparation)

Conference Contributions

- Peter Clawin, Prof. Cynthia Friend, Prof. Katharina Al-Shamery, *DIET 14*, Pacific Grove, CA, October 13-17, **2014**, *Studying redox reaction intermediates on Titania using Polarized Infrared Reflection Absorption Spectroscopy* (poster)
- Peter Clawin, Prof. Cynthia Friend, Prof. Katharina Al-Shamery, *Aus den Hexenküchen der Materialwissenschaften*, Goslar, April 30, **2014**, *Revealing reaction intermediates in the coupling of benzaldehyde on reduced Titania using Polarized Infrared Reflection Absorption Spectroscopy (PIRATS)* (poster)
- Peter Clawin, Prof. Cynthia Friend, Prof. Katharina Al-Shamery, *Summer School on Emerging Renewable Energy Conversion and Storage*, Lake Como School of Advanced Studies, Italy, September 9-13, **2013**,

Revealing reaction intermediates in the coupling of benzaldehyde on reduced Titania using Polarized Infrared Reflection AbsorpTion Spectroscopy (PIRATS) (poster)

- Peter Clawin, Prof. Cynthia Friend, Prof. Katharina Al-Shamery, *112. Bunsentagung (Annual German Conference on Physical Chemistry)*, Karlsruhe Institute of Technology (KIT), May 9-11, **2013**, *PIRATS study of oxygenates on Titania* (presentation)
- Peter Clawin, Prof. Cynthia Friend, Prof. Katharina Al-Shamery, *Gorden Research Conference and Seminar - Chemical Reactions at Surfaces*, Les Diablerets, Switzerland, April 28-May 3, **2013**, *Revealing reaction intermediates in the coupling of benzaldehyde on reduced Titania using Polarized Infrared Reflection AbsorpTion Spectroscopy (PIRATS)* (poster)
- Peter Clawin, Prof. Cynthia Friend, Prof. Katharina Al-Shamery, *DIET XIII*, Stratford-upon-Avon, UK, July 2-6, **2012**, *IRRAS study of oxygenates on Titania* (poster)
- Peter Clawin, *Meeting of FCI fellows*, Münster, December 8, **2011**, *Surface (photo-)chemistry of oxygenates on Titania* (presentation)
- Peter Clawin, Dirk Hoogestraat, Prof. Katharina Al-Shamery, *3rd German-Danish meeting on Interface Related Phenomena*, Papenburg, July 13-15 **2009**, *Gold Nano structures for Evanescent Photo-catalysis* (presentation)

presenting author is underlined

Selbstständigkeitserklärung

Hiermit versichere ich, dass ich diese Arbeit selbständig in der Arbeitsgruppe von Frau Prof. Katharina Al-Shamery verfasst habe und keine anderen als die angegebenen Quellen und Hilfsmittel benutzt habe.

Oldenburg, den January 26, 2015

Bibliography

- [1] G. Ertl, *Nobel Lecture "Reactions at surfaces: From atoms to complexity"*, **2007**, downloaded 2014-09-09, 11:45. http://www.nobelprize.org/nobel_prizes/chemistry/laureates/2007/ertl_lecture.pdf.
- [2] R. L. Puurunen, *J. Appl. Phys.* **2005**, *97*, 121301.
- [3] Y. Paz, Z. Luo, L. Rabenberg, A. Heller, *J. Mater. Res.* **1995**, *10*, 2842–2848.
- [4] J. Rullkötter in *Encyclopedia of Physical Science and Technology (Third Edition)*, R. A. Meyers (Ed.), Academic Press, New York, **2003**, pp. 549–574.
- [5] J. Rullkötter, *Marine Geochemistry*, H. D. Schulz, M. Zabel (Eds.), Springer, Berlin/Heidelberg, **2006**, chapter 4 Organic Matter: The Driving Force for Early Diagenesis, pp. 125–168.
- [6] C. M. Friend, *Spektrum der Wissenschaft* **1993**, *6*, 72 ff.
- [7] F. Schüth, *Chem. Unserer Zeit* **2006**, *40*, 92–103.
- [8] M. Baerns, A. Behr, A. Brehm, J. Gmehling, H. Hofmann, U. Onken, *Technische Chemie*, Wiley-VCH, Weinheim, **2006**.
- [9] A. Fujishima, X. Zhang, D. A. Tryk, *Surf. Sci. Rep.* **2008**, *63*, 515–582.
- [10] R. Osgood, *Chem. Rev.* **2006**, *106*, 4379–4401.
- [11] P. Kamat, *J. of Phys. Chem. C* **2007**, *111*, 2834–2860.
- [12] A. T. Bell, *Science* **2003**, *299*, 1688–1691.
- [13] S. J. Tauster, *Acc. Chem. Res.* **1987**, *20*, 389–394.
- [14] I. Langmuir, *Trans. Faraday Soc.* **1922**, *17*, 607–620.
- [15] U. Diebold, *Surf. Sci. Rep.* **2003**, *48*, 53–229.
- [16] C. L. Pang, R. Lindsay, G. Thornton, *Chem. Soc. Rev.* **2008**, *37*, 2328–2353.
- [17] M. Haruta, *Catal. Today* **1997**, *36*, 153–166.
- [18] M. Haruta, *CATTECH* **2002**, *6*, 102–115.

Bibliography

- [19] A. Fujishima, K. Honda, *Nature* **1972**, *238*, 37–38.
- [20] A. Hoferichter, *Einsatz von Titandioxid - Hoffnungsträger mit Fragezeichen*, sueddeutsche.de: <http://www.sueddeutsche.de/wissen/einsatz-von-titandioxid-hoffnungstraeger-mit-fragezeichen-1.1502445>, **2012**, downloaded 2012-10-23, 11:20.
- [21] M. Gratzel, *Nature* **2001**, *414*, 338–344.
- [22] K. W. Kolasinski, *Surface Science - Foundations of Catalysis and Nanoscience 3rd ed.*, Wiley, Chichester, **2012**.
- [23] J. C. Vickerman, I. S. Gilmore (Eds.), *Surface Analysis The Principal Techniques 2nd ed.*, Wiley, Chichester, **2009**.
- [24] P. Atkins, J. de Paula, *Atkins' Physical Chemistry 8th ed.*, Oxford, **2002**.
- [25] R. Schaub, E. Wahlström, A. Ronnau, E. Laegsgaard, I. Stensgaard, F. Besenbacher, *Science* **2003**, *299*, 377–379.
- [26] S. Wendt, J. Matthiesen, R. Schaub, E. K. Vestergaard, E. Lægsgaard, F. Besenbacher, B. Hammer, *Phys. Rev. Lett.* **2006**, *96*, 066107.
- [27] A. Al-Shemmary, R. Buchwald, K. Al-Shamery, *J. Phys.: Condens. Matter* **2010**, *22*, 159802.
- [28] L. Benz, J. Haubrich, R. G. Quiller, S. C. Jensen, C. M. Friend, *J. Am. Chem. Soc.* **2009**, *131*, 15026–15031.
- [29] P. A. Redhead, *Vacuum* **1962**, *12*, 203–211.
- [30] D. A. King, *Surf. Sci.* **1975**, *47*, 384–402, Proceedings of the Third Symposium on Surface Physics University of Utrecht, The Netherlands 26-28 June 1974.
- [31] A. de Jong, J. Niemantsverdriet, *Surf. Sci.* **1990**, *233*, 355–365.
- [32] J. Falconer, R. Madix, *Surf. Sci.* **1975**, *48*, 393–405.
- [33] J. H. Gross, *Massenspektrometrie - Ein Lehrbuch*, Springer, Berlin Heidelberg, **2013**.
- [34] S. Stein, *NIST Chemistry WebBook, NIST Standard Reference Database Number 69*, P. Linstrom, W. Mallard (Eds.), National Institute of Standards and Technology, Gaithersburg MD, 20899, **2012**, chapter "Mass Spectra" by NIST Mass Spec Data Center, <http://webbook.nist.gov>, (retrieved September 27, 2012).
- [35] J. Batey, *Vacuum* **1987**, *37*, 659–668.

- [36] B. Xu, *Prof C. Friends group - Personal communication*.
- [37] R. Madix, *Cat. Rev.- Sci. Eng.* **1984**, *26*, 281–297.
- [38] P. Hollins, J. Pritchard, *Prog. Surf. Sci.* **1985**, *19*, 275–349.
- [39] F. M. Hoffmann, *Surf. Sci. Rep.* **1983**, *3*, 107–107.
- [40] H. Carol J., *Surf. Sci.* **2002**, *500*, 577–604.
- [41] *Carl von Ossietzky Universität Oldenburg - Skript zum Fortgeschrittenenpraktikum Physikalische Chemie Versuch: Infrarot-Spektroskopie*.
- [42] J. M. Hollas, *Moderne Methoden in der Spektroskopie*, vieweg, Braunschweig Wiesbaden, **1995**.
- [43] M. Hesse, H. Meier, B. Zeeh, *Spektroskopische Methoden in der Organischen Chemie 7th ed.*, Thieme, Stuttgart, **2005**.
- [44] P. R. Griffiths, J. A. de Haseth, *Fourier Transform Infrared Spectroscopy*, Wiley, Hoboken, **2007**.
- [45] M. Schiek, K. Al-Shamery, M. Kunat, F. Traeger, C. Wöll, *Phys. Chem. Chem. Phys.* **2006**, *8*, 1505–1512.
- [46] B. E. Hayden, A. King, M. A. Newton, *Chem. Phys. Lett.* **1997**, *269*, 485–488.
- [47] B. E. Hayden, A. King, M. A. Newton, *J. Phys. Chem. B* **1999**, *103*, 203–208.
- [48] B. E. Hayden in *Oxide Surfaces, Vol. 9*, D. Woodruff (Ed.), Elsevier, Amsterdam, **2001**, chapter Vibrational Spectroscopy at Oxide Surfaces, pp. 514–549.
- [49] C. Rohmann, Y. Wang, M. Muhler, J. Metson, H. Idriss, C. Wöll, *Chem. Phys. Lett.* **2008**, *460*, 10–12.
- [50] M. Xu, Y. Gao, Y. Wang, C. Wöll, *Phys. Chem. Chem. Phys.* **2010**, *12*, 3649–3652.
- [51] Y. Wang, C. Wöll, *Surf. Sci.* **2009**, *603*, 1589–1599.
- [52] Y. Wang, A. Glenz, M. Muhler, C. Wöll, *Rev. Sci. Instrum.* **2009**, *80*, 113108.
- [53] G. A. Kimmel, M. Baer, N. G. Petrik, J. VandeVondele, R. Rousseau, C. J. Mundy, *J. Phys. Chem. Lett.* **2012**, *3*, 778–784.
- [54] N. G. Petrik, G. A. Kimmel, *J. Phys. Chem. Lett.* **2012**, *3*, 3425–3430.
- [55] M. Buchholz, P. G. Weidler, F. Bebensee, A. Nefedov, C. Woll, *Phys. Chem. Chem. Phys.* **2014**, *16*, 1672–1678.

Bibliography

- [56] Y. J. Chabal, *Semiconductor Interfaces: Formation and Properties*, G. LeLay, J. Derrien, N. Boccarda (Eds.), Springer, **1987**, chapter Vibrational Properties at Semiconductor Surfaces and Interfaces, pp. 301–327.
- [57] Y. Chabal, *Surf. Sci. Rep.* **1988**, *8*, 211–357.
- [58] W. N. Hansen, *J. Opt. Soc. Am.* **1968**, *58*, 380–390.
- [59] W. N. Hansen, *Symp. Faraday Soc.* **1970**, *4*, 27–35.
- [60] J. McIntyre, D. Aspnes, *Surf. Sci.* **1971**, *24*, 417–434.
- [61] M. Milosevic, *Internal Reflection and ATR Spectroscopy*, Wiley, Hoboken, **2012**.
- [62] P. Yeh, *Surf. Sci.* **1980**, *96*, 41–53.
- [63] A. N. Parikh, D. L. Allara, *J. Chem. Phys.* **1992**, *96*, 927–945.
- [64] W. Xu, L. T. Wood, T. D. Golding, *Phys. Rev. B* **2000**, *61*, 1740–1743.
- [65] H. Brunner, U. Mayer, H. Hoffmann, *Appl. Spectrosc.* **1997**, *51*, 209–217.
- [66] J. DeVore, *J. Opt. Soc. Am.* **1950**, *41*, 416–419.
- [67] D. Meschede, *Optik, Licht und Laser 3rd ed.*, Vieweg + Teubner, Wiesbaden, **2008**.
- [68] P. J. Feibelman, *Prog. Surf. Sci.* **1982**, *12*, 287–407.
- [69] W. Chen, W. Schaich, *Surf. Sci.* **1989**, *218*, 580–602.
- [70] W. L. Schaich, W. Chen, *Phys. Rev. B* **1989**, *39*, 10714–10724.
- [71] U. Leist, Phd thesis, Carl von Ossietzky University of Oldenburg, **2002**.
- [72] C. Kittel, *Einführung in die Festkörperphysik 14th ed.*, Oldenbourg, München Wien, **2006**.
- [73] N. W. Ashcroft, D. N. Mermin, *Festkörperphysik 4th ed.*, Oldenbourg, München, **2013**.
- [74] C. Powell, A. Jablonski, *NIST Electron Inelastic-Mean-Free-Path Database, Version 2.1, SRD 71*, National Institute of Standards and Technology, Gaithersburg, MD, **2010**, Inelastic mean free path length for titania were predicted using the TPP-2M equation.
- [75] P. Atkins, R. Friedman, *Molecular Quantum Mechanics 4th ed.*, Oxford, Oxford, **2005**.

- [76] J. B. Foresman, Æleen Frisch, *Exploring Chemistry with Electronic Structure Methods 2nd ed.*, Gaussian Inc, Wallingfort, CT, **1996**.
- [77] F. Jensen, *Introduction to Computational Chemistry*, Wiley, Chichester, England, **1999**.
- [78] K. Burke, L. O. Wagner, *Int. J. Quantum Chem.* **2013**, *113*, 96–101.
- [79] P. Hohenberg, W. Kohn, *Phys. Rev.* **1964**, *136*, B864–B871.
- [80] W. Kohn, L. J. Sham, *Phys. Rev.* **1965**, *140*, A1133–A1138.
- [81] A. D. Becke, *J. Chem. Phys.* **1993**, *98*, 5648–5652.
- [82] C. Lee, W. Yang, R. G. Parr, *Phys. Rev. B* **1988**, *37*, 785–789.
- [83] A. D. McLean, G. S. Chandler, *J. Chem. Phys.* **1980**, *72*, 5639–5648.
- [84] R. Krishnan, J. S. Binkley, R. Seeger, J. A. Pople, *J. Chem. Phys.* **1980**, *72*, 650–654.
- [85] M. J. Frisch, J. A. Pople, J. S. Binkley, *J. Chem. Phys.* **1984**, *80*, 3265–3269.
- [86] A. Wille, Ph.D. thesis, Carl von Ossietzky University of Oldenburg, **2003**.
- [87] U. Leist, A. Winkler, J. Büssov, K. Al-Shamery, *Rev. Sci. Instrum.* **2003**, *74*, 4772–4778.
- [88] M. A. Henderson, *Surf. Sci.* **1999**, *419*, 174–187.
- [89] P. J. Møller, M.-C. Wu, *Surf. Sci.* **1989**, *224*, 265–276.
- [90] Y. Chung, W. Lo, G. Somorjai, *Surf. Sci.* **1977**, *64*, 588–602.
- [91] Reprinted from *Surface Science*, *224*, Preben J. Møller and Ming-Cheng Wu, *Surface geometrical structure and incommensurate growth: Ultrathin Cu films on TiO₂(110)*, 265–276, Copyright **1989**, with permission from Elsevier.
- [92] M. Osmić, Phd-thesis, Carl von Ossietzky University of Oldenburg, **2015**, in preparation.
- [93] *Quadstar 32 bit Version 7.03*, **2005**, Pfeiffer Vacuum.
- [94] *OPUS-NT Version 3.1 Build 3,0,16*, **2000**, Bruker Optik GmbH.
- [95] U. Diebold, *Appl. Phys. A* **2003**, *76*, 681–687.
- [96] M. A. Henderson, *Surf. Sci. Rep.* **2011**, *66*, 185–297.
- [97] M. A. Henderson, I. Lyubinetsky, *Chem. Rev.* **2013**, *113*, 4428–4455.

Bibliography

- [98] A. L. Linsebigler, G. Lu, J. T. Yates, *Chem. Rev.* **1995**, *95*, 735–758.
- [99] T. L. Thompson, J. T. Yates, *J. Phys. Chem. B* **2006**, *110*, 7431–7435.
- [100] J. Haubrich, *Prof C. Friends group - Personal communication*.
- [101] E. Riedel, *Anorganische Chemie 5th ed.*, de Gruyter, Berlin; New York, **2002**.
- [102] U. Diebold, *personal communication - talk on Gordon Research Conference - Chemical Reactions at Surfaces, Les Diablerets, Switzerland April 28-May 3, 2013*.
- [103] U. Diebold, J. F. Anderson, K.-O. Ng, D. Vanderbilt, *Phys. Rev. Lett.* **1996**, *77*, 1322–1325.
- [104] H. Onishi, Y. Iwasawa, *Surf. Sci.* **1994**, *313*, L783–L789.
- [105] M. Blanco-Rey, J. Abad, C. Rogero, J. Méndez, M. F. López, E. Román, J. A. Martín-Gago, P. L. de Andrés, *Phys. Rev. B* **2007**, *75*, 081402.
- [106] K.-i. Fukui, H. Onishi, Y. Iwasawa, *Phys. Rev. Lett.* **1997**, *79*, 4202–4205.
- [107] R. Kelly, N. Q. Lam, *Radiat Eff.* **1973**, *19*, 39–48.
- [108] H. Idriss, M. Barteau, *Catal. Lett.* **1994**, *26*, 123–139.
- [109] M. Nolan, S. D. Elliott, J. S. Mulley, R. A. Bennett, M. Basham, P. Mulheran, *Phys. Rev. B* **2008**, *77*, 235424.
- [110] H. Sezen, M. Buchholz, A. Nefedov, C. Natzeck, S. Heissler, C. Di Valentin, C. Wöll, *Sci. Rep.* **2014**, *4*, 3808.
- [111] D. C. Cronemeyer, *Phys. Rev.* **1959**, *113*, 1222–1226.
- [112] K. Onda, B. Li, H. Petek, *Phys. Rev. B* **2004**, *70*, 045415.
- [113] M. Li, W. Hebenstreit, L. Gross, U. Diebold, M. A. Henderson, D. R. Jennison, P. A. Schultz, M. P. Sears, *Surf. Sci.* **1999**, *437*, 173–190.
- [114] T. L. Thompson, J. T. Y. Jr., *Top. Catal.* **2005**, *35*, 197–210.
- [115] M. V. Ganduglia-Pirovano, A. Hofmann, J. Sauer, *Surf. Sci. Rep.* **2007**, *62*, 219–270.
- [116] K. R. Phillips, S. C. Jensen, M. Baron, S.-C. Li, C. M. Friend, *J. Am. Chem. Soc.* **2013**, *135*, 574–577.
- [117] T. Bak, J. Nowotny, M. Rekas, C. Sorrell, *J. Phys. Chem. Solids* **2003**, *64*, 1057–1067.

- [118] K. Hameeuw, G. Cantele, D. Ninno, F. Trani, G. Iadonisi, *Phys. Status Solidi A* **2006**, *203*, 2219–2222.
- [119] U. Diebold, J. Lehman, T. Mahmoud, M. Kuhn, G. Leonardelli, W. Hebenstreit, M. Schmid, P. Varga, *Surf. Sci.* **1998**, *411*, 137–153.
- [120] P. Rahe, R. Bechstein, J. Schütte, F. O. anf A. Kühnle, *Phys. Rev. B* **2008**, *77*, 195410.
- [121] R. Schaub, P. Thostrup, N. Lopez, E. Laesgaard, I. Stensgaard, J. K. Norskov, F. Besenbacher, *Phys. Rev. Lett.* **2001**, *87*, 266104.
- [122] O. Bikondoa, C. L. Pang, R. Ithnin, C. A. Muryn, H. Onishi, G. Thornton, *Nat Mater* **2006**, *5*, 189–192.
- [123] M. A. Henderson, *Surf. Sci.* **1996**, *355*, 151–166.
- [124] G. Lu, A. Linsebigler, J. T. Yates, *J. Phys. Chem.* **1994**, *98*, 11733–11738.
- [125] J. Oviedo, R. Sánchez-de Armas, M. n. San Miguel, J. F. Sanz, *J. Phys. Chem. C* **2008**, *112*, 17737–17740.
- [126] M. A. Henderson, S. Otero-Tapiab, M. E. Castrob, *Faraday Discuss.* **1999**, *114*, 313.
- [127] Z. Zhang, O. Bondarchuk, J. M. White, B. D. Kay, Z. Dohnalek, *J. Am. Chem. Soc.* **2006**, *128*, 4198–4199.
- [128] M. A. Henderson, W. S. Epling, C. H. F. Peden, C. L. Perkins, *J. Phys. Chem. B* **2003**, *107*, 534–545.
- [129] Y. Du, N. A. Deskins, Z. Zhang, Z. Dohnalek, M. Dupuis, I. Lyubinetsky, *Phys. Chem. Chem. Phys.* **2010**, *12*, 6337–6344.
- [130] S. Wendt, P. T. Sprunger, E. Lira, G. K. H. Madsen, Z. Li, J. O. Hansen, J. Matthiesen, A. Blekinge-Rasmussen, E. Laegsgaard, B. Hammer, F. Besenbacher, *Science* **2008**, *320*, 1755–1759.
- [131] M. Li, W. Hebenstreit, U. Diebold, *Phys. Rev. B* **2000**, *61*, 4926–4933.
- [132] M. Li, W. Hebenstreit, U. Diebold, A. M. Tyryshkin, M. K. Bowman, G. G. Dunham, M. A. Henderson, *J. Phys. Chem. B* **2000**, *104*, 4944–4950.
- [133] P. Stone, R. A. Bennett, M. Bowker, *New J. Phys.* **1999**, *1*, 8.
- [134] R. D. Smith, R. A. Bennett, M. Bowker, *Phys. Rev. B* **2002**, *66*, 035409.
- [135] M. Bowker, R. A. Bennett, *Journal of Physics: Condensed Matter* **2009**, *21*, 474224.

Bibliography

- [136] S. Bonanni, K. Aït-mansour, H. Brune, W. Harbich, *ACS Catal.* **2011**, *1*, 385–389.
- [137] L. Benz, J. Haubrich, R. G. Quiller, C. M. Friend, *Surf. Sci.* **2009**, *603*, 1010–1017.
- [138] L. Benz, J. Haubrich, S. C. Jensen, C. M. Friend, *ACS Nano* **2011**, *5*, 834–843.
- [139] S. C. Jensen, J. Haubrich, A. Shank, C. M. Friend, *Chem. Eur. J.* **2011**, *17*, 8309–8312.
- [140] R. Bennett, P. Stone, R. Smith, M. Bowker, *Surf. Sci.* **2000**, *454-456*, 390–395.
- [141] R. Bennett, N. McCavish, *Top. Catal.* **2005**, *36*, 11–19.
- [142] M. Aono, R. R. Hasiguti, *Phys. Rev. B* **1993**, *48*, 12406–12414.
- [143] U. Martinez, L. B. Vilhelmsen, H. H. Kristoffersen, J. Stausholm-Møller, B. Hammer, *Phys. Rev. B* **2011**, *84*, 205434.
- [144] N. A. Deskins, R. Rousseau, M. Dupuis, *J. Phys. Chem. C* **2011**, *115*, 7562–7572.
- [145] E. Finazzi, C. Di Valentin, G. Pacchioni, *J. Phys. Chem. C* **2009**, *113*, 3382–3385.
- [146] G. Mattioli, F. Filippone, P. Alippi, A. Amore Bonapasta, *Phys. Rev. B* **2008**, *78*, 241201.
- [147] C. Di Valentin, G. Pacchioni, A. Selloni, *J. Phys. Chem. C* **2009**, *113*, 20543–20552.
- [148] J. Haubrich, E. Kaxiras, C. M. Friend, *Chem. Eur. J.* **2011**, *17*, 4496–4506.
- [149] M. A. Henderson, W. S. Epling, C. L. Perkins, C. H. F. Peden, U. Diebold, *J. Phys. Chem. B* **1999**, *103*, 5328–5337.
- [150] C. Naccache, P. Meriaudeau, M. Che, A. J. Tench, *Trans. Faraday Soc.* **1971**, *67*, 506–512.
- [151] C. A. Jenkins, D. M. Murphy, *J. Phys. Chem. B* **1999**, *103*, 1019–1026.
- [152] M. A. Henderson, M. Shen, Z.-T. Wang, I. Lyubinetsky, *J. Phys. Chem. C* **2013**, *117*, 5774–5784.
- [153] G. Lu, A. Linsebigler, J. T. Yates, *J. Chem. Phys.* **1995**, *102*, 3005–3008.
- [154] G. Lu, A. Linsebigler, J. T. Yates, *J. Chem. Phys.* **1995**, *102*, 4657–4662.
- [155] C. N. Rusu, J. T. Yates, *Langmuir* **1997**, *13*, 4311–4316.

- [156] G. a. Kimmel, N. G. Petrik, *Phys. Rev. Lett.* **2008**, *100*, 196102.
- [157] M. de Lara-Castells, J. L. Krause, *Chem. Phys. Lett.* **2002**, *354*, 483–490.
- [158] D. Pillay, Y. Wang, G. S. Hwang, *J. Am. Chem. Soc.* **2006**, *128*, 14000–14001.
- [159] S. Tan, Y. Ji, Y. Zhao, A. Zhao, B. Wang, J. Yang, J. Hou, *J. Am. Chem. Soc.* **2011**, *133*, 2002–2009.
- [160] S. Porsgaard, P. Jiang, F. Borondics, S. Wendt, Z. Liu, H. Bluhm, F. Besenbacher, M. Salmeron, *Angew. Chem.* **2011**, *123*, 2314–2317.
- [161] W. S. Epling, C. H. Peden, M. A. Henderson, U. Diebold, *Surf. Sci.* **1998**, *412-413*, 333–343.
- [162] Y. Du, Z. Dohnalek, I. Lyubinetsky, *J. Phys. Chem. C* **2008**, *112*, 2649–2653.
- [163] N. G. Petrik, Z. Zhang, Y. Du, Z. Dohnalek, I. Lyubinetsky, G. A. Kimmel, *J. Phys. Chem. C* **2009**, *113*, 12407–12411.
- [164] C. M. Yim, C. L. Pang, G. Thornton, *Phys. Rev. Lett.* **2010**, *104*, 036806.
- [165] E. Lira, S. Wendt, P. Huo, J. . Hansen, R. Streber, S. Porsgaard, Y. Wei, R. Bechstein, E. Laegsgaard, F. Besenbacher, *J. Am. Chem. Soc.* **2011**, *133*, 6529–6532.
- [166] F. Rieboldt, R. Bechstein, F. Besenbacher, S. Wendt, *J. Phys. Chem. C* **2014**, *118*, 3620–3628.
- [167] U. Martinez, J. O. Hansen, E. Lira, H. H. Kristoffersen, P. Huo, R. Bechstein, E. Lægsgaard, F. Besenbacher, B. Hammer, S. Wendt, *Phys. Rev. Lett.* **2012**, *109*, 155501.
- [168] H. Onishi, Y. Iwasawa, *Phys. Rev. Lett.* **1996**, *76*, 791–794.
- [169] M. Li, W. Hebenstreit, U. Diebold, M. A. Henderson, D. R. Jennison, *Faraday Discuss.* **1999**, *114*, 245–258.
- [170] H. B. Huntington, G. A. Sullivan, *Phys. Rev. Lett.* **1965**, *14*, 177–178.
- [171] P. M. Clawin, C. M. Friend, K. Al-Shamery, *Chem. Eur. J.* **2014**, *20*, 7665–7669.
- [172] R. Zehr, M. Henderson, *Surf. Sci.* **2008**, *602*, 2238–2249.
- [173] M. A. Henderson, *Surf. Sci.* **2008**, *602*, 3188–3193.
- [174] J. E. McMurry, *Acc. Chem. Res.* **1983**, *16*, 405–411.
- [175] J. E. McMurry, *Chem. Rev.* **1989**, *89*, 1513–1524.

Bibliography

- [176] W. Walter, W. Francke, *Lehrbuch der Organischen Chemie 24th ed.*, s. Hirzel Verlag, Stuttgart, **2003**.
- [177] R. Brückner, *Reaktionsmechanismen 3rd ed.*, Spektrum, München, **2004**.
- [178] H. Idriss, K. Pierce, M. A. Barteau, *J. Am. Chem. Soc.* **1991**, *113*, 715–716.
- [179] H. Idriss, M. Libby, M. A. Barteau, *Catal. Lett.* **1992**, *15*, 13–23.
- [180] H. Idriss, K. Kim, M. Barteau, *J. Catal.* **1993**, *139*, 119–133.
- [181] H. Idriss, M. Barteau, *Catal. Lett.* **1996**, *40*, 147–153.
- [182] A. B. Sherrill, V. S. Lusvardi, J. Eng Jr., J. G. Chen, M. A. Barteau, *Catalysis Today* **2000**, *63*, 43–51.
- [183] H. Qiu, H. Idriss, Y. Wang, C. Wöll, *J. Phys. Chem. C* **2008**, *112*, 9828–9834.
- [184] *SDBSWeb (National Institute of Advanced Industrial Science and Technology)*, retrieved 2012-11-22. <http://riodb01.ibase.aist.go.jp/sdbs/>.
- [185] M. A. Henderson, *J. Phys. Chem. B* **2004**, *108*, 18932–18941.
- [186] S. Stein, *NIST Chemistry WebBook, NIST Standard Reference Database Number 69*, P. Linstrom, W. Mallard (Eds.), National Institute of Standards and Technology, Gaithersburg MD, 20899, **2012**, chapter "Infrared Spectra" by NIST Mass Spec Data Center, <http://webbook.nist.gov>, (retrieved September 27, 2012).
- [187] R. Koch, *Carl von Ossietzky University - Unpublished results*.
- [188] G. A. Somorjai, Y. Li, *Introduction to Surface Chemistry and Catalysis 2nd ed.*, Wiley, Hoboken, **2010**.
- [189] E. Lira, J. O. Hansen, P. Huo, R. Bechstein, P. Galliker, E. Lægsgaard, B. Hammer, S. Wendt, F. Besenbacher, *Surf. Sci.* **2010**, *604*, 1945–1960.
- [190] J. J. Plata, V. Collico, A. M. Márquez, J. F. Sanz, *J. Phys. Chem. C* **2011**, *115*, 2819–2825.
- [191] J. M. Vohs, *Chem. Rev.* **2013**, *113*, 4136–4163.
- [192] C. R. Ayre, R. J. Madix, *J. Am. Chem. Soc.* **1995**, *117*, 2301–2312.
- [193] A. Klust, R. J. Madix, *Surf. Sci.* **2006**, *600*, 5025–5040.
- [194] B. Xu, X. Liu, J. Haubrich, C. M. Friend, *Nat. Chem.* **2010**, *2*, 61–65.
- [195] F. Gao, T. Wood, D. Goodman, *Catal. Lett.* **2010**, *134*, 9–12.

- [196] A. Linsebigler, G. Lu, J. T. Y. Jr., *J. Chem. Phys.* **1995**, *103*, 9438–9443.
- [197] A. Linsebigler, G. Lu, J. T. Y. Jr., *J. Phys. Chem.* **1996**, *100*, 6631–6636.
- [198] N. G. Petrik, G. A. Kimmel, *J. Phys. Chem. Lett.* **2010**, *1*, 2508–2513.
- [199] M. A. Henderson, *Langmuir* **1996**, *12*, 5093–5098.
- [200] Y. Du, N. A. Deskins, Z. Zhang, Z. Dohnálek, M. Dupuis, I. Lyubinetsky, *J. Phys. Chem. C* **2009**, *113*, 666–671.
- [201] A. Tilocca, C. Di Valentin, A. Selloni, *J. Phys. Chem. B* **2005**, *109*, 20963–20967.
- [202] Z. Zhang, Y. Du, N. G. Petrik, G. A. Kimmel, I. Lyubinetsky, Z. Dohnalek, *J. Phys. Chem. C* **2009**, *113*, 1908–1916.
- [203] C. L. Perkins, M. A. Henderson, *J. Phys. Chem. B* **2001**, *105*, 3856–3863.
- [204] T. Laue, A. Plagens, *Namen- und Schlagwortreaktionen der Organischen Chemie 5th ed.*, Teubner, Wiesbaden, **2006**.
- [205] J. Clayden, N. Greeves, S. Warren, *Organische Chemie 2nd ed.*, Springer, Berlin Heidelberg, **2013**.
- [206] N. A. Clinton, R. A. Kenley, T. G. Traylor, *J. Am. Chem. Soc.* **1975**, *97*, 3746–3751.
- [207] T. G. Solomons, C. B. Fryhle, *Organic Chemistry 8th ed.*, Wiley, Hoboken, **2004**.
- [208] E. Farfan-Arribas, R. J. Madix, *Surf. Sci.* **2003**, *544*, 241–260.
- [209] J. E. Rekoske, M. A. Barteau, *Langmuir* **1999**, *15*, 2061–2070.
- [210] S. Luo, J. L. Falconer, *J. Catal.* **1999**, *185*, 393–407.
- [211] M. A. Henderson, *Langmuir* **2005**, *21*, 3451–3458.
- [212] M. A. Henderson, *J. Phys. Chem. B* **2005**, *109*, 12062–12070.
- [213] M. A. Henderson, *J. Phys. Chem. C* **2008**, *112*, 11433–11440.
- [214] T. van der Meulen, A. Mattson, L. Österlund, *J. Catal.* **2007**, *251*, 131–144.
- [215] E. C. Landis, S. C. Jensen, K. R. Phillips, C. M. Friend, *J. Phys. Chem. C* **2012**, *116*, 21508–21513.
- [216] E. Stuve, R. Madix, B. Sexton, *Surf. Sci.* **1982**, *119*, 279–290.

Bibliography

- [217] M. J. Frisch, G. W. Trucks, H. B. Schlegel, G. E. Scuseria, M. A. Robb, J. R. Cheeseman, G. Scalmani, V. Barone, B. Mennucci, G. A. Petersson, H. Nakatsuji, M. Caricato, X. Li, H. P. Hratchian, A. F. Izmaylov, J. Bloino, G. Zheng, J. L. Sonnenberg, M. Hada, M. Ehara, K. Toyota, R. Fukuda, J. Hasegawa, M. Ishida, T. Nakajima, Y. Honda, O. Kitao, H. Nakai, T. Vreven, J. A. Montgomery, Jr., J. E. Peralta, F. Ogliaro, M. Bearpark, J. J. Heyd, E. Brothers, K. N. Kudin, V. N. Staroverov, R. Kobayashi, J. Normand, K. Raghavachari, A. Rendell, J. C. Burant, S. S. Iyengar, J. Tomasi, M. Cossi, N. Rega, J. M. Millam, M. Klene, J. E. Knox, J. B. Cross, V. Bakken, C. Adamo, J. Jaramillo, R. Gomperts, R. E. Stratmann, O. Yazyev, A. J. Austin, R. Cammi, C. Pomelli, J. W. Ochterski, R. L. Martin, K. Morokuma, V. G. Zakrzewski, G. A. Voth, P. Salvador, J. J. Dannenberg, S. Dapprich, A. D. Daniels, O. Farkas, J. B. Foresman, J. V. Ortiz, J. Cioslowski, D. J. Fox, *Gaussian 09 Revision B.01*, Gaussian Inc. Wallingford CT 2009.
- [218] C. Fábri, T. Szidarovszky, G. Magyarfalvi, G. Tarczay, *J. Phys. Chem. A* **2011**, *115*, 4640–4649.
- [219] P. Borowski, A. Drzewiecka, M. Fernández-Gómez, M. P. Fernández-Liencrees, T. P. Ruiz, *Vib. Spectrosc.* **2010**, *52*, 16–21.
- [220] M. A. Henderson, *J. Phys. Chem. B* **1997**, *101*, 221–229.
- [221] W. Haynes (Ed.), *Handbook of Chemistry and Physics 94th ed.*, CRC Press, Boca Raton, **2013**.
- [222] A. M. Márquez, J. J. Plata, J. F. Sanz, *J. Phys. Chem. C* **2009**, *113*, 19973–19980.
- [223] M.-a. Yasuo, A. Sasahara, H. Onishi, *J. Phys. Chem. C* **2010**, *114*, 14579–14582.
- [224] R. T. Zehr, M. A. Henderson, *Phys. Chem. Chem. Phys.* **2010**, *12*, 8085–8092.
- [225] R. T. Zehr, N. A. Deskins, M. A. Henderson, *J. Phys. Chem. C* **2010**, *114*, 16900–16908.
- [226] B. Xu, X. Liu, J. Haubrich, R. J. Madix, C. M. Friend, *Angew. Chem., Int. Ed.* **2009**, *48*, 4206–4209.
- [227] K. Kim, M. Barteau, *Surf. Sci.* **1989**, *223*, 13–32.
- [228] M. Mittelbach, "*Methanolvergasung aus Biogas*" *Machbarkeits-Studie*, **2005**, Karl-Franzens-Universität Graz, downloaded 2014-09-03,13:45. http://www.noest.or.at/intern/dokumente/076_Enbericht_Methanolstudie.pdf.

- [229] Y. K. Kim, B. D. Kay, J. M. White, Z. Dohnálek, *J. Phys. Chem. C* **2007**, *111*, 18236–18242.
- [230] B. Jasper, Master's thesis, Carl von Ossietzky University of Oldenburg, **2014**, in preparation.
- [231] M. Shen, M. A. Henderson, *J. Phys. Chem. C* **2012**, *116*, 18788–18795.
- [232] D. A. Panayotov, S. Burrows, M. Mihaylov, K. Hadjiivanov, B. M. Tissue, J. R. Morris, *Langmuir* **2010**, *26*, 8106–8112.
- [233] R. S. de Armas, J. Oviedo, M. A. San Miguel, J. F. Sanz, *J. Phys. Chem. C* **2007**, *111*, 10023–10028.
- [234] J. Zhao, J. Yang, H. Petek, *Phys. Rev. B* **2009**, *80*, 235416.
- [235] M. Farnesi Camellone, J. Zhao, L. Jin, Y. Wang, M. Muhler, D. Marx, *Angew. Chem. Int. Ed.* **2013**, *52*, 5780–5784.
- [236] E. Farfan-Arribas, R. J. Madix, *J. Phys. Chem. B* **2002**, *106*, 10680–10692.
- [237] Z. Zhang, O. Bondarchuk, B. D. Kay, J. M. White, Z. Dohnálek, *J. Phys. Chem. C* **2007**, *111*, 3021–3027.
- [238] M. Shen, D. P. Acharya, Z. Dohnálek, M. A. Henderson, *J. Phys. Chem. C* **2012**, *116*, 25465–25469.
- [239] S. C. Jensen, C. M. Friend, *Top. Catal.* **2013**, *56*, 1377–1388.
- [240] P. M. Jayaweera, E. L. Quah, H. Idriss, *J. Phys. Chem. C* **2007**, *111*, 1764–1769.
- [241] A. M. Nadeem, J. M. R. Muir, K. A. Connelly, B. T. Adamson, B. J. Metson, H. Idriss, *Phys. Chem. Chem. Phys.* **2011**, *13*, 7637–7643.
- [242] D. J. Cooke, D. Eder, J. A. Elliott, *J. Phys. Chem. C* **2010**, *114*, 2462–2470.
- [243] J. C. F. Rodríguez-Reyes, C. M. Friend, R. J. Madix, *Surf. Sci.* **2012**, *606*, 1129–1134.
- [244] *Entry on benzylalcohol in the GESTIS-Stoffdatenbank database*, downloaded 2014-09-05, 16:14. [http://gestis.itrust.de/nxt/gateway.dll?f=id\\$t=default.htm\\$vid=gestisdeu:sdbdeu\\$id=020370](http://gestis.itrust.de/nxt/gateway.dll?f=id$t=default.htm$vid=gestisdeu:sdbdeu$id=020370).
- [245] *Entry on benzaldehyde in the GESTIS-Stoffdatenbank database*, downloaded 2014-09-05, 16:14. [http://gestis.itrust.de/nxt/gateway.dll/gestis_de/013380.xml?f=templates\\$fn=default.htm\\$3.0](http://gestis.itrust.de/nxt/gateway.dll/gestis_de/013380.xml?f=templates$fn=default.htm$3.0).
- [246] T. Cremer, S. C. Jensen, C. M. Friend, *J. Phys. Chem. C* **2014**, *NN*, NN.

Bibliography

- [247] R. Sreekumar, C. Pillai, *Catal. Lett.* **1993**, *19*, 281–291.
- [248] M. Jayamani, C. Pillai, *J. Catal.* **1983**, *82*, 485–488.
- [249] G. H. Enevoldsen, H. P. Pinto, A. S. Foster, M. C. R. Jensen, W. A. Hofer, B. Hammer, J. V. Lauritsen, F. Besenbacher, *Phys. Rev. Lett.* **2009**, *102*, 136103.
- [250] Q. Guo, W. Oh, D. Goodman, *Surf. Sci.* **1999**, *437*, 49–60.
- [251] M. Chen, D. Goodman, *Top. Catal.* **2007**, *44*, 41–47.
- [252] M. Chen, D. W. Goodman, *Chem. Soc. Rev.* **2008**, *37*, 1860–1870.
- [253] C. Wu, M. S. J. Marshall, M. R. Castell, *J. Phys. Chem. C* **2011**, *115*, 8643–8652.
- [254] F. Träger, *Westfälische Hochschule - Unpublished results.*
- [255] W. Lanford, *Nuclear Instruments and Methods in Physics Research Section B: Beam Interactions with Materials and Atoms* **1992**, *66*, 65–82.
- [256] T. R. Thurston, J. P. Wilcoxon, *J. Phys. Chem. B* **1999**, *103*, 11–17.
- [257] B. L. Abrams, J. P. Wilcoxon, *Crit. Rev. Solid. State.* **2005**, *30*, 153–182.
- [258] R. Bliem, R. Kosak, L. Perneczky, Z. Novotny, O. Gamba, D. Fobes, Z. Mao, M. Schmid, P. Blaha, U. Diebold, G. S. Parkinson, *ACS Nano* **2014**, *8*, 7531–7537.
- [259] C. Adamo, V. Barone, *J. Chem. Phys.* **1999**, *110*, 6158–6170.
- [260] J. P. Perdew, K. Burke, M. Ernzerhof, *Phys. Rev. Lett.* **1996**, *77*, 3865–3868.
- [261] Y. Zhao, D. G. Truhlar, *Theor. Chem. Acc.* **2008**, *120*, 215–241.
- [262] Y. Tantirungrotechai, K. Phanasant, S. Roddecha, P. Surawatanawong, V. Sutthikhum, J. Limtrakul, *Theochem. J. Mol. Struct.* **2006**, *760*, 189–192.